THE 2 Ms *CHANDRA* DEEP FIELD-NORTH SURVEY AND THE 250 Ks EXTENDED *CHANDRA* DEEP FIELD-SOUTH SURVEY: IMPROVED POINT-SOURCE CATALOGS

Y. Q. Xue[1], B. Luo[2,3], W. N. Brandt[2,3,4], D. M. Alexander[5], F. E. Bauer[6,7,8], B. D. Lehmer[9,10,11], and G. Yang[2,3]

[1] CAS Key Laboratory for Researches in Galaxies and Cosmology, Center for Astrophysics, Department of Astronomy, University of Science and Technology of China, Chinese Academy of Sciences, Hefei, Anhui 230026, China; xuey@ustc.edu.cn
[2] Department of Astronomy and Astrophysics, Pennsylvania State University, University Park, PA 16802, USA
[3] Institute for Gravitation and the Cosmos, Pennsylvania State University, University Park, PA 16802, USA
[4] Department of Physics, Pennsylvania State University, University Park, PA 16802, USA
[5] Centre for Extragalactic Astronomy, Department of Physics, Durham University, Durham, DH1 3LE, UK
[6] Instituto de Astrofísica, Facultad de Física, Pontificia Universidad Católica de Chile, Casilla 306, Santiago 22, Chile
[7] Millennium Institute of Astrophysics, Chile
[8] Space Science Institute, 4750 Walnut Street, Suite 205, Boulder, Colorado 80301, USA
[9] The Johns Hopkins University, Homewood Campus, Baltimore, MD 21218, USA
[10] NASA Goddard Space Flight Centre, Code 662, Greenbelt, MD 20771, USA
[11] Department of Physics, University of Arkansas, 226 Physics Building, 835 West Dickson Street, Fayetteville, AR 72701, USA
Received 2015 July 11; accepted 2016 February 17; published 2016 May 26

ABSTRACT

We present improved point-source catalogs for the 2 Ms *Chandra* Deep Field-North (CDF-N) and the 250 ks Extended *Chandra* Deep Field-South (E-CDF-S) Surveys, implementing a number of recent improvements in *Chandra* source-cataloging methodology. For CDF-N/E-CDF-S, we provide a main catalog that contains 683/1003 X-ray sources detected with WAVDETECT at a false-positive probability threshold of 10^{-5} that also satisfy a binomial-probability source-selection criterion of $P < 0.004/P < 0.002$. Such an approach maximizes the number of reliable sources detected: a total of 196/275 main-catalog sources are new compared to the Alexander et al. CDF-N/Lehmer et al. E-CDF-S main catalogs. We also provide CDF-N/E-CDF-S supplementary catalogs that consist of 72/56 sources detected at the same WAVDETECT threshold and having P of 0.004–0.1/0.002–0.1 and $K_s \leqslant 22.9/K_s \leqslant 22.3$ mag counterparts. For all $\approx$1800 CDF-N and E-CDF-S sources, including the $\approx$500 newly detected ones (these being generally fainter and more obscured), we determine X-ray source positions utilizing centroid and matched-filter techniques; we also provide multiwavelength identifications, apparent magnitudes of counterparts, spectroscopic and/or photometric redshifts, basic source classifications, and estimates of observed active galactic nucleus and galaxy source densities around respective field centers. Simulations show that both the CDF-N and E-CDF-S main catalogs are highly reliable and reasonably complete. Background and sensitivity analyses indicate that the on-axis mean flux limits reached represent a factor of $\approx$1.5–2.0 improvement over the previous CDF-N and E-CDF-S limits. We make our data products publicly available.

Key words: catalogs – cosmology: observations – diffuse radiation – galaxies: active – surveys – X-rays: galaxies

Supporting material: extended figures, machine-readable tables

1. INTRODUCTION

Over the past few decades, deep and wide cosmic X-ray surveys of active galactic nuclei (AGNs), and their critical complementary multiwavelength observations, have dramatically improved our understanding of many aspects of growing supermassive black holes in the distant universe, e.g., the AGN population and its evolution ("demographics"), the physical processes operating in AGNs ("physics"), and the interactions between AGNs and their environments ("ecology"; see Brandt & Alexander 2015 for a review). The *Chandra* Deep Fields (CDFs) have critically contributed to the characterization of the 0.5–8 keV cosmic X-ray background sources, the majority of which are AGNs. The *Chandra* Deep Field-North (CDF-N; 1 Ms CDF-N, Brandt et al. 2001; 2 Ms CDF-N, Alexander et al. 2003, hereafter A03) and the CDF-South (CDF-S; 1 Ms CDF-S, Giacconi et al. 2002; 2 Ms CDF-S, Luo et al. 2008; 4 Ms CDF-S, Xue et al. 2011, hereafter X11) are the two deepest *Chandra* surveys, and the latter is complemented by the 1 Ms Extended-*Chandra* Deep Field-South (E-CDF-S, which consists of four flanking, contiguous 250 ks *Chandra* observations; Lehmer et al. 2005, hereafter L05). The CDFs have enormous supporting multiwavelength investments that

are key to source identification and characterization, and will remain a crucial resource for interpreting the nature of extragalactic populations identified using superb multiwavelength surveys (e.g., *James Webb Space Telescope*, ALMA, and EVLA) over the coming decades, thereby continuing the lasting legacy value.

Over the last $\approx$10 years there have been major improvements in the methodology of producing *Chandra* source catalogs, as evidenced by, e.g., the four Ms CDF-S point-source catalogs (X11). Similar applications of a two-stage source-detection approach, which is a key ingredient of such an improved methodology, have also been presented in, e.g., Getman et al. (2005), Nandra et al. (2005, 2015), Elvis et al. (2009), Laird et al. (2009), Lehmer et al. (2009), Puccetti et al. (2009), and Ehlert et al. (2013; see Sections 2.2.2 and 2.3.1 for details). Given the parallel importance of the CDF-N and E-CDF-S to the CDF-S, it is imperative to create improved 2 Ms CDF-N and 250 ks E-CDF-S source catalogs implementing such improvements in methodology, thereby contributing to the most effective exploitation of the large investments in the CDF surveys. The E-CDF-S, though not as deep as CDF-N and CDF-S, is also a premiere deep-survey field, and its data

Table 1
Improvements over Existing 2 Ms CDF-N (A03) and 250 ks E-CDF-S (L05) Catalogs

	A03 and L05	Improved Catalogs	Example Section(s)
Astrometric alignment	Using merged observations	Frame by frame (i.e., observation by observation)	2.2.1
Source detection	WAVDETECT-only	WAVDETECT + ACIS Extract (AE)[12] no-source probability	2.2.2 and 2.3.1
Extraction region	Circular aperture	AE polygonal region that approximates the PSF shape	2.2.2
Crowded sources	Manual extraction	AE extraction by automatically shrinking regions	2.2.2
Background estimate	Source-masking approach	AE BETTER_BACKGROUNDS algorithm	2.2.2
X-ray photometry	Cumulative images	AE merging of extractions on individual images	2.2.2
Comprehensive source identification	Not provided	Provided	2.3.3
Redshift compilation	Not provided	Provided	2.3.4
Source classification	Not provided	Provided	2.3.4

significantly help with measurements of sources located at large off-axis angles in CDF-S proper.

In this paper we present the improved *Chandra* point-source catalogs and associated data products, together with observation details, data reduction, and technical analyses, for 2 Ms CDF-N and 250 ks E-CDF-S. Table 1 gives a list of major improvements implemented in X11 and here in the production of the improved source catalogs over the existing 2 Ms CDF-N (A03) and 250 ks E-CDF-S (L05) catalogs. The key improvements include (1) adoption of the flexible and reliable two-stage source-detection approach (leading to a significant number of new sources with high confidence in their validity without new *Chandra* observational investment), (2) optimal extractions of X-ray photometry (enabling the best possible X-ray characterization of detected sources), and (3) secure identification of multiwavelength counterparts of detected X-ray sources (allowing for detailed follow-up studies). The details of the improvements are given in the relevant sections as indicated in Table 1. To implement the improved methodology, we make extensive use of the ACIS Extract (AE; Broos et al. 2010)[12] point-source analysis software that accurately computes source X-ray properties (most importantly point-spread function; PSF), when combining multiple observations that have different roll angles and/or aim points. The improved 2 Ms CDF-N and 250 ks E-CDF-S point-source catalogs presented here supercede those presented in A03 and L05, respectively.

This paper is structured as follows. Section 2 is dedicated to the production of the improved 2 Ms CDF-N source catalogs, covering a range of contents organized into subsections and sub-subsections as appropriate, including observations and data reduction (Section 2.1), creation of the images, exposure maps, and the candidate-list catalog (Section 2.2), production of the main and supplementary catalogs (Sections 2.3 and 2.4), completeness and reliability analyses (Section 2.5), and background and sensitivity analyses (Section 2.6). Section 3 is parallel to Section 2, but dedicated to the production of the improved 250 ks E-CDF-S source catalogs, in basically the same manner as Section 2. Section 4 summarizes the results of this work.

Throughout this paper, Galactic column densities of $N_H = 1.6 \times 10^{20}$ cm^{-2} and $N_H = 8.8 \times 10^{19}$ cm^{-2} along the lines of sight to CDF-N and E-CDF-S are adopted, respectively (e.g., Stark et al. 1992). The J2000.0 coordinate system, the AB magnitude system, and a cosmology with

$H_0 = 69.7$ km s^{-1} Mpc^{-1}, $\Omega_M = 0.282$, and $\Omega_\Lambda = 0.718$ (Hinshaw et al. 2013) are used.

2. PRODUCTION OF THE IMPROVED 2 Ms CDF-N POINT-SOURCE CATALOGS

The overall production procedure, as illustrated in Figure 1, is similar to that described in X11. For ease of reading, here we provide only essential details and refer readers to X11 for full details. In addition, we make our 2 Ms CDF-N data products publicly available.[13]

2.1. Observations and Data Reduction

2.1.1. Observations and Observing Conditions

The 2 Ms CDF-N consists of a total of 20 separate observations taken between 1999 November 13 and 2002 February 22 (see Table 1 of A03 for the journal for these 20 CDF-N observations). The 20 CDF-N observations were made with the Advanced CCD Imaging Spectrometer (ACIS; Garmire et al. 2003) on board *Chandra* that consists of an imaging array (ACIS-I; with an overall field of view of $16.'9 \times 16.'9 = 285.6$ arcmin^2) and a spectroscopic array (ACIS-S). The four ACIS-I CCDs were in operation throughout the 20 CDF-N observations, while the ACIS-S CCD S2 was operated for the first 12 observations. We do not use the data taken with the ACIS-S CCD S2 in this work due to its large off-axis angle and consequently its low sensitivity. The focal-plane temperature was $-110°$C for the first three CDF-N observations (ObsIDs = 580, 967, and 966) and $-120°$C for the remaining ones. The first 12 CDF-N observations were carried out in Faint mode, while the later 8 observations were carried out in Very Faint mode to help screen background events and thus improve the ACIS sensitivity for detecting faint X-ray sources (Vikhlinin 2001).
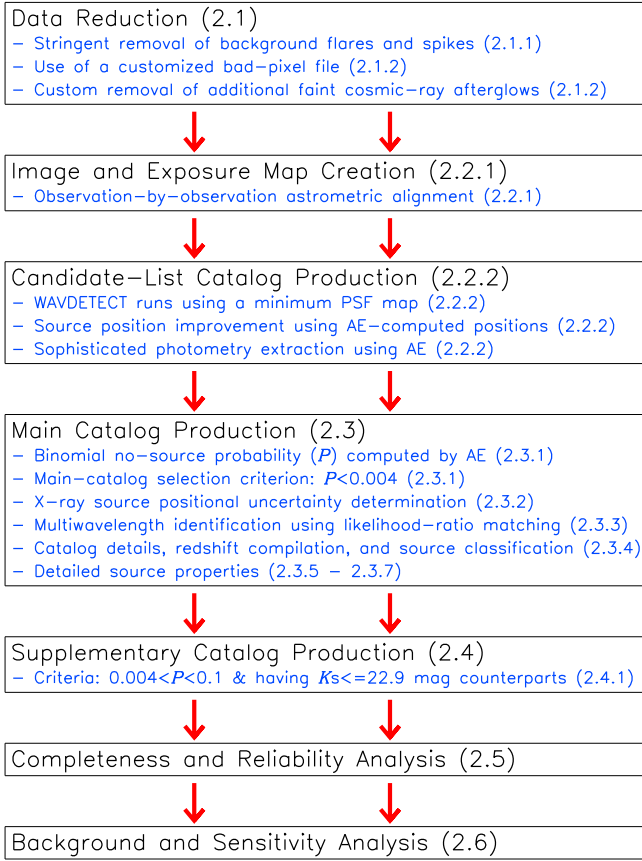
The background light curves for all the 20 CDF-N observations were examined utilizing the *Chandra* Imaging and Plotting System (ChIPS).[14] During observation 2344, there are two significant flares in the background, each lasting ≈ 1.5 ks and being $\gtrsim 2$ times higher than nominal; a time span of ≈ 18.0 ks between these two flares was affected moderately. The background increased significantly (up to ≈ 4 times higher than nominal) toward the end of observation 3389, affecting an

---

[12] Details on AE can be found at http://www.astro.psu.edu/xray/docs/TARA/ae_users_guide.html.

[13] The data products, including the final event files, raw images, effective exposure maps, background maps, sensitivity maps, and solid-angle versus flux-limit curves for 2 Ms CDF-N and 250 ks E-CDF-S are available at http://www2.astro.psu.edu/users/niel/hdf/hdf-chandra.html and http://www2.astro.psu.edu/users/niel/ecdfs/ecdfs-chandra.html, respectively.

[14] The ChIPS analysis threads can be found at http://cxc.harvard.edu/chips/.

2 Ms CDF-N: Cataloging Procedure

Figure 1. Flowchart of the overall 2 Ms CDF-N cataloging procedure. The black text describes the major cataloging steps, while the blue text highlights some key points in the corresponding steps. The numbers in parentheses indicate the relevant subsections/sub-subsections.

exposure of ≈ 17.0 ks. All the other observations are free from strong flaring and are stable within $\approx 20\%$ of typical quiescent *Chandra* values, except for a number of short moderate "spikes" (up to ≈ 1.5 times higher than nominal). To remove these significant flares and moderate spikes, we utilize an iterative sigma-clipping tool LC_SIGMA_CLIP, which is part of the *Chandra* Interactive Analysis of Observations (CIAO; we use CIAO 4.5 and CALDB 4.5.9 in this work) package. We adopt 2.6σ, 2.0σ, and 3.5σ clippings for observation 2344, observation 3389, and the other observations, respectively. After filtering the data on good-time intervals, we obtain a total effective exposure time of 1.896 Ms for the 20 CDF-N observations (see Section 2.2.1), which is smaller than the value of 1.945 Ms reported in A03 due to our more stringent filtering process.

For the majority of the 20 observations, the ACIS-I aim point was placed near the HDF-N (Williams et al. 1996) center and the roll angles varied around two main values of ≈ 40 and ≈ 140 degrees. This pointing scheme and the roll constraints not only lead to a total region of 447.5 arcmin^2 covered by these 20 CDF-N observations that is considerably larger than the ACIS-I field of view, but also result in all the individual pointings being separated from the average aim point by $> 1'$. The average aim point is $\alpha_{\rm J2000.0} = 12^{\rm h}36^{\rm m}45\!\!^{\rm s}\!7$, $\delta_{\rm J2000.0} = +62°13'58\!\!''0$, weighted by the 20 individual exposures that typically range from ≈ 50 to ≈ 170 ks.

2.1.2. Data Reduction

We make use of CIAO tools and custom software for data reduction. We utilize ACIS_PROCESS_EVENTS to reprocess each level 1 observation, which takes into account the radiation damage sustained by the CCDs during the beginning of the *Chandra* operations by implementing a Charge Transfer Inefficiency correction procedure presented in Townsley et al. (2000, 2002; this procedure is only applicable to $-120°$C observations, but not to $-110°$C ones) and applies a modified bad-pixel file instead of the standard CXC one. Our customized bad-pixel file retrieves several percent of the ACIS-I pixels on which numerous events are valid for source detection, photometry extraction, and spectral analysis that would otherwise be discarded\(see Section 2.2 of Luo et al. 2008 for reasoning). We set CHECK_VF_PHA=YES in ACIS_PROCESS_E-VENTS for observations carried out in Very Faint mode for better cleaning of background events, which utilizes a 5×5 pixel event island to identify imposter cosmic-ray background events. We then use ACIS_DETECT_AFTERGLOW to eliminate cosmic-ray afterglows. To reject further surviving faint afterglows, we remove a number of additional faint afterglows with $\gtrsim 3$ counts arriving within a timespan of 20 s on a pixel that almost certainly signifies an association with cosmic-ray afterglows (see Footnote 27 of X11 for our reasoning).

2.2. Images, Exposure Maps, and Candidate-list Catalog

2.2.1. Image and Exposure Map Creation

For astrometric alignment purposes, we first run WAVDETECT (Freeman et al. 2002) with the option of "psffile = none"[15] at a false-positive probability threshold of 10^{-6} on each of the individual cleaned 0.5–7 keV[16] images to construct initial source lists and utilize AE to determine centroid positions of detected sources. In order to register the observations to a common astrometric frame, we then match X-ray centroid positions to the $K_s \leqslant 21.0$ mag sources in the GOODS-N WIRCam K_s-band catalog (Wang et al. 2010) rather than the Very Large Array (VLA) 1.4 GHz GOODS-N radio sources used by A03 (Morrison et al. 2010; note that an earlier VLA 1.4 GHz GOODS-N radio catalog presented in Richards 2000 was adopted in A03), because we find the astrometric frame of the K_s-band catalog to be in better agreement with that of other multiwavelength catalogs that are used for our X-ray source identifications in Section 2.3.3. We carry out X-ray/K_s-band

---

[15] This option means that no PSF map file is provided to WAVDETECT such that WAVDETECT will not compute PSF sizes for source detection. With this option on, the source-detection results are still secure although the source characteristics might not be reliable. However, in Section 2.2.2 where we perform formal source detections on merged images, we do provide an appropriate PSF map to WAVDETECT.
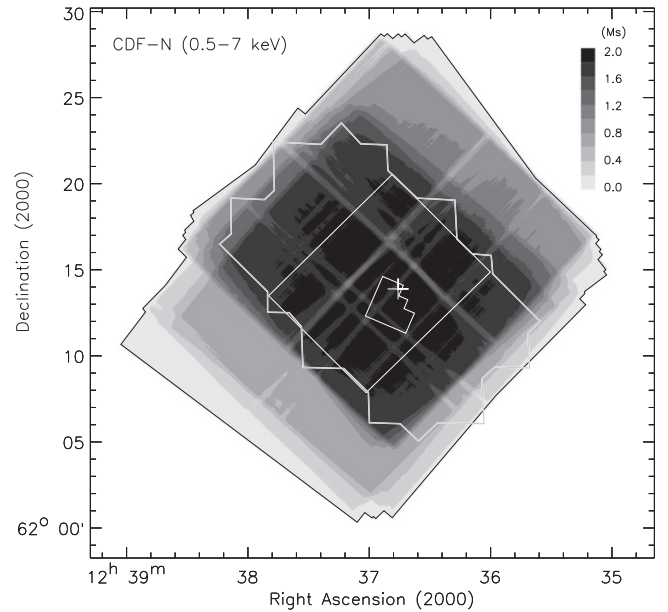
[16] Throughout this work, we switch to an upper energy bound of 7 keV from the "traditional" 8 keV adopted by our previous CDF catalogs (e.g., A03, L05, X11) for the following reasons: (1) the *Chandra* High Resolution Mirror Assembly (HRMA) effective area decreases significantly toward high energies, e.g., ≈ 180 cm^2 at 7 keV versus ≈ 80 cm^2 at 8 keV (as opposed to ≈ 800 cm^2 at 1 keV); (2) the gain of net counts at 7–8 keV is modest due to increasing background toward high energies; and (3) the upper energy bound of 7 keV has been adopted for source detection and/or X-ray photometry by a number of other cataloging works (e.g., Elvis et al. 2009; Laird et al. 2009; Nandra et al. 2015). (However, as noted in Footnote 32 of X11, there appears to be no significant statistical difference between catalogs made with upper energy cuts of 7 and 8 keV for the case of 4 Ms CDF-S.) We note that the cataloging of the coming 7 Ms CDF-S (PI: W. N. Brandt; the *Chandra* observations are scheduled to be completed by 2016 March) will adopt the upper energy cut of 7 keV as well, to ensure uniformity among the latest CDF catalogs.
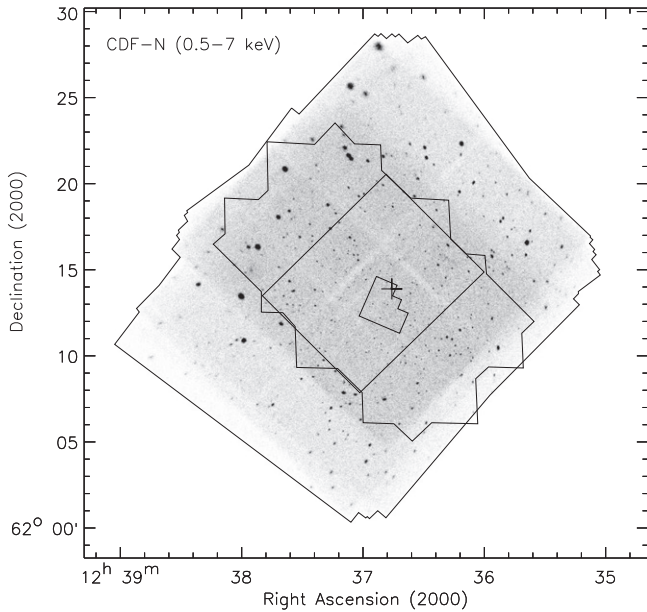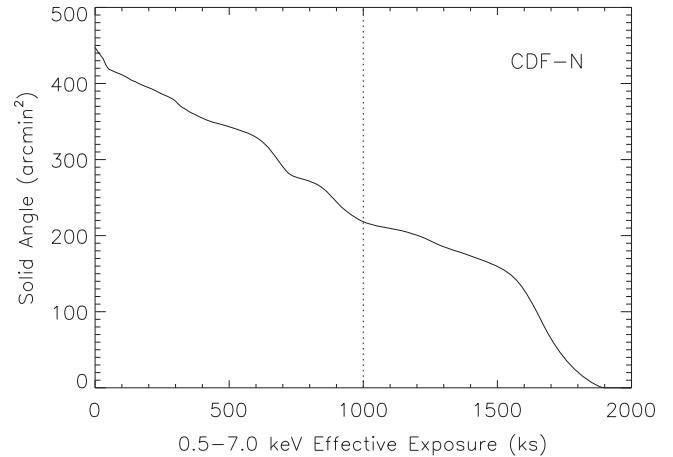
Figure 2. Full band (0.5–7.0 keV) raw image of the 2 Ms CDF-N rendered using linear grayscales. The outermost segmented boundary indicates the coverage of the entire CDF-N. Toward the direction of the exposure-weighted average aim point (denoted as a plus sign) sitting roughly at the field center, the large polygon, the rectangle, and the small polygon denote the regions for the GOODS-N (Giavalisco et al. 2004), the CANDELS GOODS-N deep (Grogin et al. 2011; Koekemoer 2011), and the HDF-N (Williams et al. 1996) surveys, respectively. The light grooves running through the image are caused by the ACIS-I CCD gaps, thereby having lower effective exposures than the nearby non-gap areas (clearly revealed in Figure 3). The apparent trend of sources having larger sizes off the center is due to the PSF degradation toward larger off-axis angles (also see Figure 5).

Figure 3. Full band (0.5–7.0 keV) effective-exposure map of the 2 Ms CDF-N rendered using linear grayscales (indicated by the inset scale bar). The darkest areas indicate the highest effective exposure times, reaching a maximum of 1.896 Ms. The ACIS-I CCD gaps can be clearly identified as the light grooves. The regions and the plus sign have the same meanings as those in Figure 2.

Figure 4. Survey solid angle as a function of minimum full band (0.5–7.0 keV) effective exposure for the 2 Ms CDF-N. The 2 Ms CDF-N covers a total area of 447.5 arcmin^2 and has a maximum exposure of 1.896 Ms. The vertical dotted line denotes an effective exposure of 1 Ms. 218.3 arcmin^2 (48.8%) of the CDF-N survey area has >1 Ms effective exposure.

matching and astrometric reprojection utilizing REPROJECT_AS-PECT and WCS_UPDATE with a matching radius of $2''$ and a $0''6$ residual rejection limit, resulting in typical false-match rates of $\lesssim 8\%$ that are estimated using the simple shifting-and-recorrelating approach (this approach of estimating false-match rates is adopted throughout this paper except for Sections 2.3.3 and 3.3.3 where we perform multiwavelength identifications for the detected X-ray sources). We then reproject all the observations to the frame of observation 3293 that is among the observations with the longest exposures and has raw coordinates closely matched to the K_s-band astrometric frame. Subsequently we combine the individual event files into a merged event file using DMMERGE, from which we construct images using the standard ASCA grade set for three standard bands: 0.5–7.0 keV (full band; FB), 0.5–2.0 keV (soft band; SB), and 2–7 keV (hard band; HB; see footnote 16). Figure 2 shows the full band raw image.

Following the basic procedure detailed in Section 3.2 of Hornschemeier et al. (2001), we produce effective-exposure maps for the three standard bands and normalize them to the effective exposures of a pixel lying at the average aim point, assuming a photon index of $\Gamma = 1.4$ that is the slope of the cosmic 2–10 keV X-ray background (e.g., Marshall et al. 1980; Gendreau et al. 1995; Hasinger et al. 1998; Hickox & Markevitch 2006). This procedure accounts for the effects of vignetting, CCD gaps, bad-column and bad-pixel filtering, as well as the spatial and time-dependent degradation in quantum efficiency caused by contamination on the ACIS optical-blocking filters. Figure 3 presents the full band effective-

exposure map and Figure 4 shows the survey solid angle as a function of the minimum full band effective exposure.

We create exposure-weighted smoothed images following Section 3.3 of Baganoff et al. (2003). We first generate the raw images and effective-exposure maps in the 0.5–2, 2–4, and 4–7 keV bands. We then utilize CSMOOTH (Ebeling et al. 2006) to adaptively smooth the raw images and effective-exposure maps. We finally divide the smoothed images by the corresponding smoothed effective-exposure maps and combine the exposure-weighted smoothed images into a false-color composite, which is shown in Figure 5.
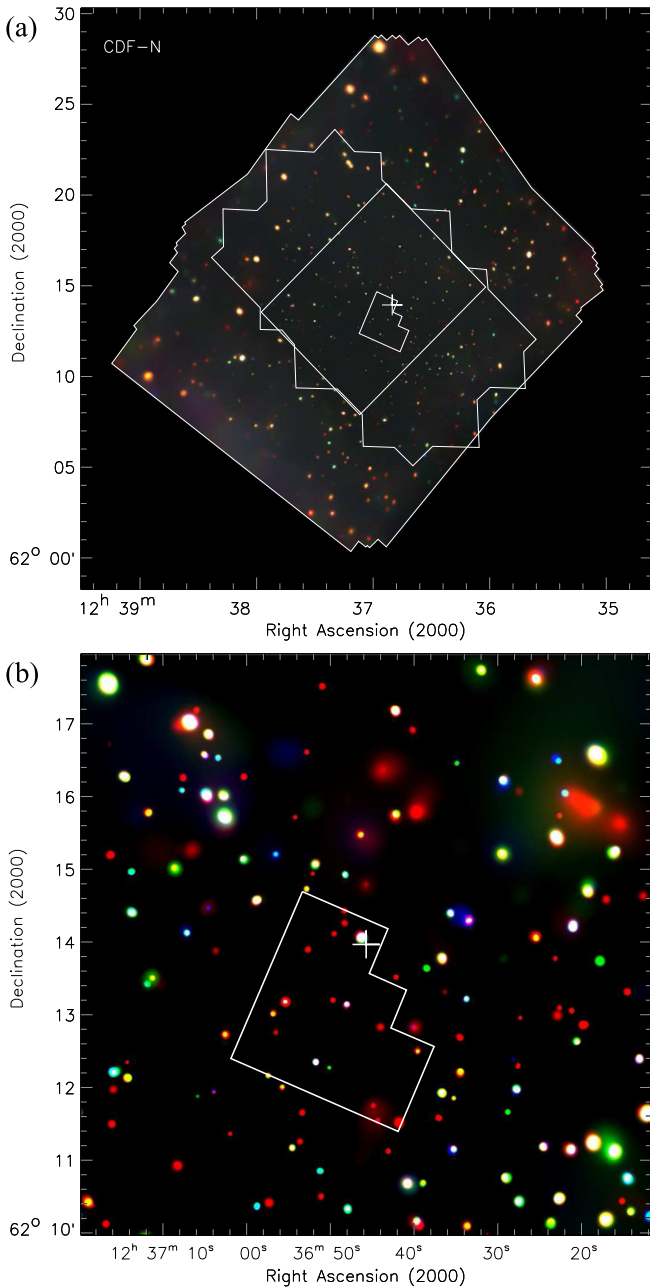
Figure 5. (a) False-color image of the 2 Ms CDF-N that is a color composite of the exposure-weighted and adaptively smoothed images in the 0.5–2.0 keV (red), 2–4 keV (green), and 4–7 keV (blue) bands. (b) A zoomed-in view of the false-color image of the central $8' \times 8'$ region. Near the field center, the seemingly smaller sizes and lower brightnesses of the sources are due to the smaller PSF size on-axis. The regions and the plus sign have the same meanings as those in Figure 2.

2.2.2. Candidate-list Catalog Production

To perform a blind search of potential sources, we run WAVDETECT on each combined raw image in the three standard bands to search for likely sources and to generate a candidate-list catalog, utilizing a "$\sqrt{2}$ sequence" of wavelet scales (i.e., from 1, $\sqrt{2}$, 2, ... to 16 pixels), a false-positive probability threshold of 10^{-5} (sigthresh = 10^{-5}), and an appropriate merged PSF map. We obtain the PSF map in the following way. We first utilize MKPSFMAP to produce a soft-band PSF map pixel by pixel for each individual observation, setting the

"energy" parameter to 1.497 keV and the parameter of "encircled counts fraction (ECF)" to 0.393. We then use DMIMGFILT to combine the individual PSF maps into a merged one with the option of adopting the minimum PSF map size at each pixel location rather than the average. In the above WAVDETECT runs, our choices of parameters (i.e., energy = 1.497 keV, ECF = 0.393, and minimum PSF map size) provide the best sensitivity to point-like sources across the entire field, thus being able to detect as many candidate-list sources as possible. However, these parameter choices in combination with sigthresh = 10^{-5} would inevitably introduce a non-negligible number of spurious sources that have $\lesssim 2$–3 source counts. In Section 2.3.1, we therefore construct a more conservative main catalog by determining additional detection significances of each candidate-list source in the three standard bands and discarding sources with significances below an adopted threshold value.

Our candidate-list catalog contains 1003 CDF-N source candidates, with each being detected in at least one of the three standard bands. For these candidate sources, we adopt source positions in a prioritized order, i.e., the full band, soft band, or hard band position. We adopt a $2''5$ matching radius to carry out cross-band matching for sources lying within $6'$ of the average aim point (i.e., $\theta < 6'$) and a $4''0$ matching radius for sources with $\theta \geqslant 6'$, with the mismatch probability being $\approx 1\%$ across the entire field. We then make use of the AE-computed centroid and matched-filter positions to improve the above WAVDETECT source positions. The WAVDETECT, centroid, and matched-filter positions are comparably accurate on-axis, while the matched-filter positions are of better accuracy off-axis. As such, we adopt centroid positions for sources located inside $\theta = 8'$ and matched-filter positions for sources lying outside $\theta = 8'$.

Utilizing AE, we compute photometry for the candidate-list catalog sources. AE calculates the PSF model by simulating the *Chandra* HRMA with the MARX[17] ray-tracing simulator (version 4.4). It then creates a polygonal extraction region, rather than the "traditional" circular aperture (e.g., A03, L05), to approximate the $\approx 90\%$ encircled-energy fraction (EEF) contour of a local PSF that is measured at 1.497 keV. For crowded sources with overlapping polygonal extraction regions, AE automatically shrinks extraction regions ($\approx 40\%$–75% EEFs) that are not overlapping and chosen to be as large as possible. We utilize the AE "BETTER_BACKGROUNDS" algorithm for background extraction, which models the spatial distributions of flux for the source of interest and its adjacent sources making use of unmasked data, and then calculates local background counts inside background regions removing contributions from the source and its adjacent sources. This algorithm generates accurate background extractions, making it particularly critical for crowded sources. For each source, AE analyzes individual observations independently and merges the data to produce photometry with appropriate energy-dependent aperture corrections applied.

2.3. Main Chandra Source Catalog

2.3.1. Selection of Main-catalog Sources

To cull spurious candidate-list catalog sources and thus produce a reliable main *Chandra* source catalog, we calculate

---

[17] See http://space.mit.edu/CXC/MARX/index.html for the MARX manual.
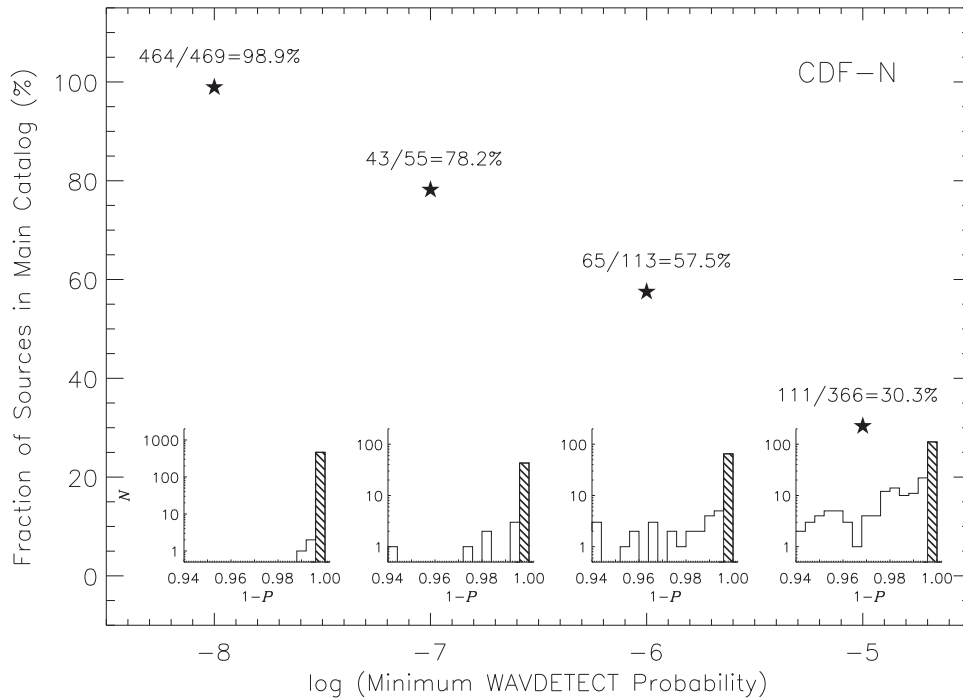
Figure 6. Fraction of the candidate-list catalog sources having an AE binomial no-source probability $P < 0.004$ that are included in the 2 Ms CDF-N main catalog, as a function of minimum WAVDETECT probability (see footnote 20; denoted as five-pointed stars). The number of sources having $P < 0.004$ vs. the number of candidate-list catalog sources detected at each minimum WAVDETECT probability is displayed (note that there are $464 + 43 + 65 + 111 = 683$ main-catalog sources and $469 + 55 + 113 + 366 = 1003$ candidate-list catalog sources). The fraction of candidate-list catalog sources included in the main catalog falls monotonically from 98.9% to 30.3% between minimum WAVDETECT probabilities of 10^{-8} and 10^{-5}. The insets present the $1 - P$ distributions for the candidate-list catalog sources at each minimum WAVDETECT probability, and the shaded areas highlight those included in the main catalog (i.e., satisfying $1 - P > 0.996$).

for each candidate source the binomial no-source probability P that no source exists given the source and local background measurements, which can be calculated as

$$P(X \geqslant S) = \sum_{X=S}^{N} \frac{N!}{X!(N-X)!} p^X (1-p)^{N-X}, \qquad (1)$$

where S is the total number of counts in the source-extraction region without subtracting the background counts B_{src} therein; $N = S + B_{ext}$, with B_{ext} being the total background counts extracted within a background-extraction region; and $p = 1/(1 + \mathrm{BACKSCAL})$ with $\mathrm{BACKSCAL} = B_{ext}/B_{src}$ being the probability that a photon is located inside the source-extraction region. AE computes P in each of the three standard bands. We include a candidate source in the main catalog only if it has $P < 0.004$ in at least one of the three standard bands.[18,19] The criterion of $P < 0.004$ results from a balance between keeping the fraction of spurious sources small

and recovering the maximum possible number of real sources, primarily based on joint maximization of the total number of sources and minimization of the fraction of sources without significant multiwavelength counterparts (see Section 2.3.3). Our main catalog consists of a total of 683 sources given this $P < 0.004$ criterion. Figure 6 presents the fraction of candidate-list sources that satisfy the $P < 0.004$ main-catalog source-selection criterion and the $1 - P$ distribution of candidate-list sources as a function of the minimum WAVDETECT probability.[20]

The cataloging procedure adopted in this work is characterized by a number of advantages over a "traditional" WAVDETECT-only approach (e.g., A03, L05; see Table 1), including, e.g.,: (1) the better PSF approximation (i.e., using MARX-simulated polygonal source-extraction regions rather than circular apertures) that lays the foundation of accurate X-ray photometry, (2) the more sophisticated background treatment that takes into account effects of both adjacent sources and CCD gaps, and (3) the more flexible and reliable two-stage source-detection approach that provides an effective identification of real X-ray sources, including those falling below the traditional more stringent WAVDETECT searching threshold (e.g., sigthresh = 10^{-6}). Note that such a two-stage source-detection approach has been implemented in a similar

---

[18] We note that our $P < 0.004$ source-detection procedure associated with Equation (1) can also be discussed in terms of False Discovery Rate (FDR) and Type I/II errors (i.e., false positives/negatives). We refer interested readers to Benjamini & Hochberg (1995) for a discussion of FDR.

[19] The adopted source-detection criterion of $P < (P_0 = 0.004)$ does not straightforwardly indicate that, for a source with $P < P_0$ in each of the three standard bands, its final probability of being fake is $1 - (1 - P_0)^3 \approx 3P_0$. This is because only the soft band and hard band are truly distinct, while the full band, being the sum of the soft band and hard band, is dependent both on the soft band and hard band. Furthermore, $P < P_0$ is only the second stage of the overall two-stage source-detection approach (i.e., WAVDETECT plus $P < P_0$), which implies that the probability of a source being fake is not strictly P_0, even as far as only one single band is concerned. Therefore, we rely on simulations (see Section 2.5) to obtain a realistic estimate of the reliability of our main-catalog sources.

[20] We also run WAVDETECT with sigthresh = 10^{-6}, 10^{-7}, and 10^{-8} in order to provide a more detailed WAVDETECT-based perspective on source significance. The minimum WAVDETECT probability gives the WAVDETECT significance with lower values representing higher significances. For instance, if a source was detected with WAVDETECT in at least one of the three standard bands at sigthresh = 10^{-7} but was not detected in any of the three standard bands at sigthresh = 10^{-8}, then the minimum WAVDETECT probability is 10^{-7} for this source.

way in a number of previous studies (e.g., Getman et al. 2005; Nandra et al. 2005, 2015; Elvis et al. 2009; Laird et al. 2009; Lehmer et al. 2009; Puccetti et al. 2009; X11; Ehlert et al. 2013).

2.3.2. X-Ray Source Positional Uncertainty

We find 230 matches between the 683 main-catalog sources and the $K_s \leqslant 20.0$ mag sources in the GOODS-N WIRCam K_s-band catalog using a matching radius of $1\rlap{.}''5$. On average ≈ 5.1 (2.2%) false matches are expected, with a median offset of $1\rlap{.}''05$ for these false matches. Figure 7(a) presents the positional offset between these 230 X-ray-K_s-band matches (the median offset is $0\rlap{.}''28$) as a function of off-axis angle. We find that the source indicated as a red filled circle around the top-left corner is likely an off-nuclear source based on inspecting its X-ray and *Hubble Space Telescope* (*HST*) images and therefore do not include it in the following analysis of X-ray positional uncertainty. Figure 7(b) presents the positional residuals between the X-ray and K_s-band positions for the remaining 229 sources, which appear roughly symmetric. Figure 7(a) reveals clear off-axis angle and source-count dependencies for these sources, with the former caused by the degrading *Chandra* PSF toward large off-axis angles and the latter caused by statistical difficulties in identifying the centroid of a faint X-ray source. We adopt the Kim et al. (2007) functional form and obtain an empirical relation for the positional uncertainty of our main-catalog X-ray sources by fitting to the 229 X-ray sources with K_s-band counterparts, which is given as

$$\log \Delta_X = 0.0514\theta - 0.4538 \log C + 0.1262, \quad (2)$$

where Δ_X is the X-ray positional uncertainty in units of arcseconds at the 68% confidence level, θ denotes the off-axis angle in units of arcminutes, and C represents the source counts quoted in the energy band that is used to determine the source position (note that our Equation (2) is very similar to Equation (2) of X11). Figure 8 shows the distributions of X-ray-K_s-band positional offsets in four bins of X-ray positional uncertainty. When deriving Equation (2) and presenting X-ray-K_s-band positional offsets in Figures 7 and 8, we allow for positional uncertainties arising from the K_s-band sources that are typically $\lesssim 0\rlap{.}''1$.

2.3.3. Multiwavelength Identifications

We implement the Luo et al. (2010) likelihood-ratio matching procedure to identify the primary optical/near-infrared/mid-infrared/radio (ONIR) counterparts for our main-catalog X-ray sources. We adopt, in order of priority (given factors of positional accuracy, angular resolution, false-match rate, and catalog depth), six ONIR catalogs for identification purposes.

1. The VLA 1.4 GHz GOODS-N radio catalog (denoted as "VLA"; Morrison et al. 2010), with a 5σ detection threshold of $\approx 20\,\mu$Jy at the field center.
2. The GOODS-N *HST* version 2.0 F850LP (z)-band catalog (denoted as "GOODS-N"; Giavalisco et al. 2004), with a 5σ limiting magnitude of ≈ 28.1.
3. The CANDELS GOODS-N WFC3 F160W-band catalog (denoted as "CANDELS"; Grogin et al. 2011; Koekemoer 2011), with a 5σ limiting magnitude of ≈ 27.4.
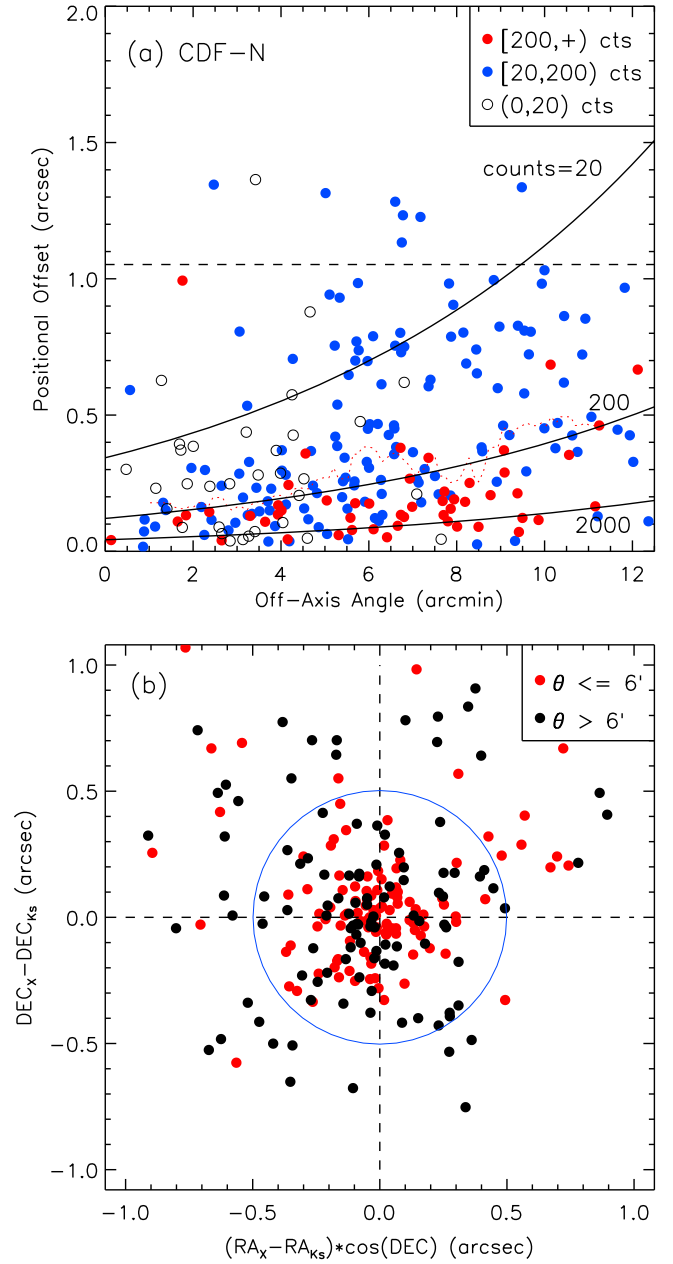
Figure 7. (a) Positional offset vs. off-axis angle for the 230 2 Ms CDF-N main-catalog sources that have $K_s \leqslant 20.0$ mag counterparts in the GOODS-N WIRCam K_s-band catalog (Wang et al. 2010) utilizing a matching radius of $1\rlap{.}''5$ (see Section 2.3.2 for the description of an apparent outlier, i.e., the red filled circle located around the top-left corner, that deviates significantly from the relation defined as Equation (2)). Red filled, blue filled, and black open circles indicate X-ray sources having $\geqslant 200$, $\geqslant 20$, and < 20 counts in the energy band that is used to determine the source position, respectively. The red dotted curve denotes the running median of positional offset in bins of $2'$. The horizontal dashed line represents the median offset ($1\rlap{.}''05$) of the false matches expected. The three solid curves correspond to the $\approx 68\%$ confidence-level X-ray positional uncertainties (derived according to Equation (2)) for sources with 20, 200, and 2000 counts. (b) Positional residuals between the X-ray and K_s-band positions for the remaining 229 X-ray-K_s-band matches. Red and black filled circles represent sources with an off-axis angle of $\leqslant 6'$ and $> 6'$, respectively. A blue circle with a $0\rlap{.}''5$ radius is drawn at the center as a visual guide.

4. The GOODS-N WIRCam K_s-band catalog (denoted as "Ks"; Wang et al. 2010), with a 5σ limiting magnitude of ≈ 24.5.
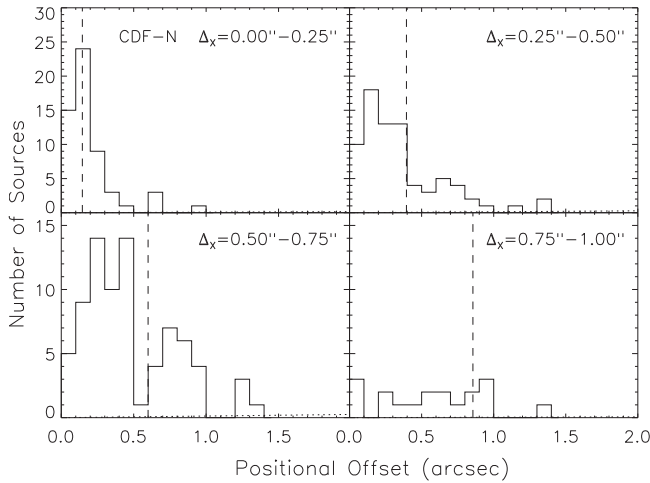
Figure 8. Histograms of X-ray-K_s-band positional offsets for the 229 2 Ms CDF-N main-catalog sources that are matched to the GOODS-N WIRCam $K_s \leqslant 20.0$ mag sources (Wang et al. 2010) utilizing a matching radius of $1\rlap{.}''5$. Based on their X-ray positional uncertainties estimated with Equation (2), these matched sources are divided into four bins of $0''$–$0\rlap{.}''25$, $0\rlap{.}''25$–$0\rlap{.}''50$, $0\rlap{.}''50$–$0\rlap{.}''75$, and $0\rlap{.}''75$–$1''$. In each panel (bin), the vertical dashed line denotes the median X-ray positional uncertainty; the dotted line (almost indistinguishable from the bottom x-axis) displays the expected numbers of false matches assuming a uniform spatial distribution of K_s-band sources as a function of X-ray-K_s-band positional offset.

5. The H-HDF-N Suprime-Cam R-band catalog (denoted as "CapakR"; Capak et al. 2004), with a 5σ limiting magnitude of $\approx$26.6; this catalog is complemented by the H-HDF-N photometric-redshift catalog (denoted as "Yang14"; Yang et al. 2014).
6. The SEDS IRAC $3.6\,\mu$m band catalog (denoted as "IRAC"; Ashby et al. 2013), with a 3σ limiting magnitude of $\approx$26.0.

We shift the above ONIR source positions appropriately to be consistent with the GOODS-N WIRCam K_s-band astrometry (see Section 2.2.1), by removing systematic positional offsets between the ONIR and K_s-band coordinates of common sources that are matched using a matching radius of $0\rlap{.}''5$. We identify primary ONIR counterparts for 670 (98.1%) of the 683 main-catalog sources. We estimate the false-match rates for the above six catalogs in the listed order to be 0.2%, 3.7%, 1.5%, 1.3%, 4.5%, and 1.3%, respectively, utilizing the Monte Carlo approach described in Broos et al. 2007, 2011) rather than the simple shifting-and-recorrelating approach, given that the Monte Carlo approach provides more realistic and reliable estimates of false-match rates by taking into account different levels of susceptibilities to false matching associated with different X-ray source populations (also see Section 4.3 of X11 for more details). We derive the average false-match rate as 1.9% by means of weighting the false-match rates of individual ONIR catalogs with the number of counterparts in each catalog. The high identification rate in conjunction with the small false-match rate serves as independent evidence that the vast majority of our main-catalog sources are robust.

We visually examine the X-ray images of the 13 main-catalog sources without highly significant multiwavelength counterparts, and find that the majority of them have apparent or even strong X-ray signatures. Of these 13 sources, 2 are relatively bright sources (with 47.4 and 25.0 full band counts) that are free of associations with any background flares or cosmic-ray afterglows. These two sources are located near a very bright optical source (their counterparts might thus be hidden by light of the bright sources) and are also present in the A03 main catalog. The other 11 sources are all fainter, with $<$20 full-band counts (some of them are thus likely false detections), none of which are present in the A03 main or supplementary catalog.

2.3.4. Main-catalog Details

For easy use of our main catalog, in Table 2 we provide a list of a total of 72 columns in our main *Chandra* X-ray source catalog (note that the contents of Table 2 are very similar to those of Table 2 of X11). We present the main catalog itself in Table 3. Below we give the details of these 72 columns.

1. Column 1 gives the source sequence number (i.e., XID) in this work. Sources are sorted in order of increasing R.A.
2. Columns 2 and 3 give the J2000.0 R.A. and decl. (determined in Section 2.2.2) of the X-ray source, respectively.
3. Columns 4 and 5 give the minimum value of $\log P$ among the three standard bands, with P being the binomial no-source probability computed by AE, and the logarithm of the minimum WAVDETECT false-positive probability detection threshold, respectively. More negative values of $\log P$ and WAVDETECT false-positive probability threshold correspond to a source detection of higher significance. For sources with $P = 0$, we set $\log P = -99.0$. We find a median value of $\log P = -10.7$ for the main-catalog sources, being much smaller than the main-catalog selection threshold value of $\log P < -2.4$ (i.e., $P < 0.004$; see Section 2.3.1). We find that 464, 43, 65, and 111 sources have minimum WAVDETECT probabilities (see footnote 20) of 10^{-8}, 10^{-7}, 10^{-6}, and 10^{-5}, respectively (see Figure 6).
4. Column 6 gives the X-ray positional uncertainty in units of arcseconds at the $\approx$68% confidence level, which is computed utilizing Equation (2), which is dependent on both off-axis angle and aperture-corrected net source counts. For the main-catalog sources, the positional uncertainty ranges from $0\rlap{.}''10$ to $2\rlap{.}''02$, with a median value of $0\rlap{.}''47$.
5. Column 7 gives the off-axis angle of each X-ray source, in units of arcminutes, that is the angular separation between the X-ray source and the average aim point given in Section 2.1.1. For the main-catalog sources, the off-axis angle ranges from $0\rlap{.}'13$ to $14\rlap{.}'63$, with a median value of $6\rlap{.}'01$ (see Section 2.1.1 for the observational pointing scheme and roll constraints that lead to such a wide range of off-axis angles).
6. Columns 8–16 give the aperture-corrected net (i.e., background-subtracted) source counts and the associated 1σ upper and lower statistical errors (Gehrels 1986) for the three standard bands (computed in Section 2.2.2), respectively. We treat a source as being "detected" for photometry purposes in a given band only if it satisfies $P < 0.004$ in that band. We calculate upper limits for sources not detected in a given band, according to the Bayesian method of Kraft et al. (1991) for a 90% confidence level, and set the corresponding errors to -1.00.

Table 2
2 Ms CDF-N Main Catalog: Overview of Columns

Column(s)	Description
1	Source sequence number (i.e., XID) in this work
2, 3	J2000.0 R.A. and decl. of the X-ray source
4	Minimum value of $\log P$ among the three standard bands (P is the binomial no-source probability calculated by AE)
5	Logarithm of the minimum WAVDETECT false-positive probability detection threshold
6	X-ray positional uncertainty (in units of arcseconds) at the $\approx 68\%$ confidence level
7	Off-axis angle (in units of arcminutes) of the X-ray source
8–16	Aperture-corrected net (i.e., background-subtracted) source counts and the associated errors for the three standard bands
17	Flag of whether a source has a radial profile consistent with that of the local PSF
18, 19	J2000.0 R.A. and decl. of the primary optical/near-infrared/mid-infrared/radio (ONIR) counterpart
20	Offset (in units of arcseconds) between the X-ray source and its primary ONIR counterpart
21	AB magnitude of the primary ONIR counterpart
22	Catalog name of the primary ONIR counterpart
23–40	J2000.0 R.A., decl., and AB magnitude of the counterpart in the six ONIR catalogs
41, 42	Secure spectroscopic redshift and its reference
43–53	Photometric-redshift information compiled from the literature
54	Preferred redshift adopted in this work
55–57	Corresponding XID, J2000.0 R.A., and decl. of the A03 main- and supplementary-catalog sources
58–60	Effective exposure times (in units of seconds) derived from the exposure maps for the three standard bands
61–63	Band ratio and the associated errors
64–66	Effective photon index and the associated errors
67–69	Observed-frame fluxes (in units of erg cm^{-2} s^{-1}) for the three standard bands
70	Absorption-corrected, rest-frame 0.5–7 keV luminosity (in units of erg s^{-1})[a]
71	Estimate of likely source type (AGN, Galaxy, or Star)
72	Note on the source (whether the source is in a close double or triple)

Note.
[a] Note that $L_{0.5-8\,\mathrm{keV}} = 1.066 \times L_{0.5-7\,\mathrm{keV}}$ and $L_{2-10\,\mathrm{keV}} = 0.721 \times L_{0.5-7\,\mathrm{keV}}$, given the assumed $\Gamma_{\mathrm{int}} = 1.8$ (see the description of Column 70 in Section 2.3.4 for details).

7. Column 17 gives a flag indicating whether a source shows a radial profile consistent with that of the local PSF. This analysis is motivated by the fact that the use of 9 wavelet scales up to 16 pixels in the WAVDETECT runs in Section 2.2.2 potentially allows for the detection of extended sources on such scales compared to local PSFs. From the merged PSF image, we initially derive a set of cumulative EEFs by means of extracting the PSF power within a series of circular apertures up to a 90% EEF radius. From the merged source image, we subsequently derive another set of cumulative EEFs by means of extracting source counts within a series of circular apertures up to the same 90% EEF. Finally, we make use of a Kolmogorov–Smirnov (K–S) test to calculate the probability (ρ_{K-S}) of the two sets of cumulative EEFs being consistent with each other. Of the 683 main-catalog sources, we find that all but 15 have $\rho_{K-S} > 0.05$, i.e., these sources have radial profiles consistent with those of their corresponding PSFs above a 95% confidence level (thus being likely point-like sources), and set the value of this column to 1 for these sources. We then set the value of this column to 0 for the 15 sources with $\rho_{K-S} \leqslant 0.05$, which are located across the entire CDF-N field and show no pattern of spatial clustering. Furthermore, we visually inspect these 15 sources and do not find any significant signature of extension.

8. Columns 18 and 19 give the R.A. and decl. of the primary ONIR counterpart (shifted accordingly to be consistent with the K_s-band astrometric frame; see Section 2.3.3). Sources without ONIR counterparts have these two columns set to "00 00 00.00" and "+00 00 00.0."

9. Column 20 gives the offset between the X-ray source and the primary ONIR counterpart in units of arcseconds. Sources without ONIR counterparts have this column set to −1.00.

10. Column 21 gives the AB magnitude of the primary ONIR counterpart in the counterpart-detection band.[21] Sources without ONIR counterparts have this column set to −1.00.

11. Column 22 gives the name of the ONIR catalog (i.e., VLA, GOODS-N, CANDELS, Ks, CapakR/Yang14, or IRAC; see Section 2.3.3) where the primary counterpart is found. Sources without ONIR counterparts have a value set to "....".

12. Columns 23–40 give the counterpart R.A., decl., and AB magnitude (see footnote 21) from the above six ONIR catalogs (the coordinates have been shifted accordingly to be consistent with the K_s-band astrometric frame; see Section 2.3.3). We match the position of the primary ONIR counterpart (i.e., Columns 18 and 19) with the six ONIR catalogs using a matching radius of 0″.5. We set values of R.A. and decl. to "00 00 00.00" and "+00 00 00.0" and set AB magnitudes to −1.00 for sources without matches. We find 31.3%, 55.2%, 57.2%, 91.7%, 68.5%, and 87.0% of the main-catalog sources have VLA, GOODS-N, CANDELS, Ks, CapakR/Yang14, and IRAC counterparts, respectively.

13. Columns 41 and 42 give the spectroscopic redshift (z_{spec}) and its corresponding reference. Only secure z_{spec}'s are collected and they are from (1) Barger et al. (2008), (2)

_____
[21] The radio AB magnitudes are converted from the radio flux densities using $m(\mathrm{AB}) = -2.5 \log(f_\nu) - 48.60$.

Table 3
2 Ms CDF-N Main *Chandra* Source Catalog

No. (1)	α_{2000} (2)	δ_{2000} (3)	$\log P$ (4)	WAVDETECT (5)	Pos Err (6)	Off-axis (7)	Full Band (8)	Full Band Upp Err (9)	Full Band Low Err (10)	Soft Band (11)	Soft Band Upp Err (12)	Soft Band Low Err (13)
1	12 35 12.35	+62 16 35.1	−2.7	−5	1.3	11.18	39.1	−1.0	−1.0	20.7	9.2	8.0
2	12 35 15.09	+62 14 06.9	−17.8	−8	0.8	10.56	55.2	10.3	9.1	43.9	8.8	7.5
3	12 35 16.70	+62 15 37.9	−9.0	−7	0.7	10.50	61.2	13.3	12.1	33.3	9.1	7.9
4	12 35 18.77	+62 15 51.9	−14.7	−8	0.6	10.30	101.4	16.6	15.4	61.6	11.8	10.6
5	12 35 19.40	+62 13 40.5	−11.3	−8	0.6	10.06	73.8	14.2	13.0	44.4	9.8	8.6

Note. The full table contains 72 columns of information for the 683 X-ray sources.

(This table is available in its entirety in machine-readable form.)
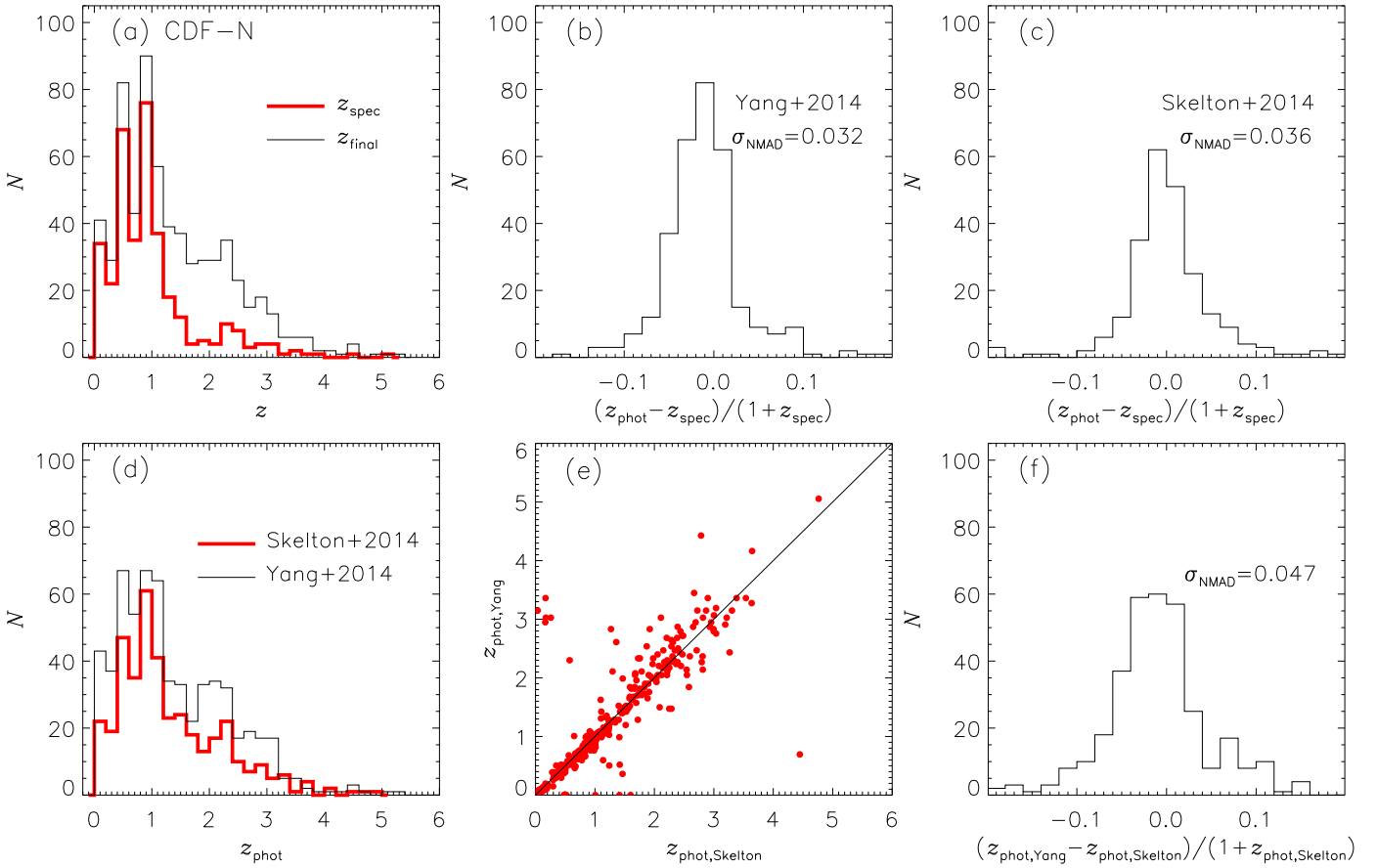
Figure 9. Redshift information for the 2 Ms CDF-N main-catalog sources. (a) Histograms of z_{spec} (351 sources; $351/683 = 51.4\%$) and z_{final} (638 sources; $638/683 = 93.4\%$). (b) Histogram of $(z_{phot} - z_{spec})/(1 + z_{spec})$ from Yang et al. (2014; 347 sources) with σ_{NMAD} annotated. (c) Histogram of $(z_{phot} - z_{spec})/(1 + z_{spec})$ from Skelton et al. (2014; 264 sources) with σ_{NMAD} annotated. (d) Histograms of z_{phot} from Yang et al. (2014; 612 sources) and Skelton et al. (2014; 389 sources). (e) The Yang et al. z_{phot} vs. the Skelton et al. z_{phot} for the 365 sources that have z_{phot} estimates from both catalogs. (f) Histogram of $(z_{phot,Yang} - z_{phot,Skelton})/(1 + z_{phot,Skelton})$ for these 365 sources with σ_{NMAD} annotated.

Cowie et al. (2004), (3) Wirth et al. (2004), (4) Cooper et al. (2011), (5) Chapman et al. (2005), (6) Barger et al. (2003), and (7) Skelton et al. (2014). The number preceding the corresponding reference is listed in Column 42. We match the positions of primary ONIR counterparts with the above z_{spec} catalogs utilizing a 0″5 matching radius. For the 670 main-catalog sources with ONIR counterparts, we find that 351 (52.4%) have z_{spec} measurements ($307/351 = 87.5\%$ have $R \leqslant 24$ mag and $44/351 = 12.5\%$ have $R > 24$ mag). Sources without z_{spec} have these two columns set to -1.000 and -1, respectively. The z_{spec} histogram is shown in Figure 9(a).

14. Columns 43–53 give the photometric-redshift (z_{phot}) information compiled from the literature. Columns 43–48 give the z_{phot}, the associated 1σ lower and upper bounds, the associated quality flag Q_z (smaller Q_z values denote better quality, with $0 < Q_z \lesssim 1$ indicating a reliable z_{phot} estimate), the alternative z_{phot} (set to -1.000 if not available), and the likely photometric classification ("Galaxy," "Star," or "Xray_AGN"; "..." indicates lacking relevant information) from the H-HDF-N z_{phot} catalog of Yang et al. (2014). Columns 49–53 give the z_{phot}, the associated 1σ lower and upper bounds, Q_z, and the likely photometric classification ("Galaxy" or "Star") from the CANDELS/3D-*HST* z_{phot} catalog of Skelton et al. (2014). We match the positions of primary

ONIR counterparts with the above z_{phot} catalogs utilizing a 0″5 matching radius. Of the 670 main-catalog sources with ONIR counterparts, 612 (91.3%) and 389 (58.1%) have z_{phot} estimates from Yang et al. (2014) and Skelton et al. (2014), respectively. Sources without z_{phot}'s have all these columns correspondingly set to -1.000 or "...". Figures 9(b)–(d) show the histograms of $(z_{phot} - z_{spec})/(1 + z_{spec})$ and z_{phot} for these two z_{phot} catalogs. The Yang et al. histogram of $(z_{phot} - z_{spec})/(1 + z_{spec})$ seems skewed toward slightly negative values (i.e., by $\lesssim 2\%$), which is likely caused by some systematic errors of a small subset of the adopted templates in z_{phot} estimation; there appears no such skewness for the Skelton et al. histogram of $(z_{phot} - z_{spec})/(1 + z_{spec})$. Figures 9(e) and (f) show the Yang et al. z_{phot} versus the Skelton et al. z_{phot} and the histogram of $(z_{phot,Yang} - z_{phot,Skelton})/(1 + z_{phot,Skelton})$, with both revealing general agreement between the two sets of z_{phot} estimates and the latter again indicating the above slightly negative skewness of the Yang et al. z_{phot}. We caution that the quoted z_{phot} qualities, as indicated by values of σ_{NMAD} annotated in Figures 9(b) and (c), do not necessarily represent realistic estimates because those z_{phot} qualities are not derived using blind tests (see, e.g., Section 3.4 of Luo et al. 2010 for relevant discussion) and in some cases "training biases" are involved in z_{phot}

derivation (e.g., the Skelton et al. z_{phot} catalog makes use of template correction).

15. Column 54 gives the preferred redshift (z_{final}) adopted in this work. We choose z_{final} for a source in the following order of preference: secure z_{spec}, the CANDELS/3D-*HST* z_{phot}, and the H-HDF-N z_{phot}. Of the 670 main-catalog sources with ONIR counterparts, 638 (95.2%) have z_{spec}'s or z_{phot}'s.

16. Column 55 gives the corresponding source ID number in the A03 2 Ms CDF-N catalogs. We match our X-ray source positions to the A03 source positions (shifted accordingly to be consistent with the K_s-band astrometric frame) using a 2″5 matching radius for sources having $\theta < 6'$ and a 4″0 matching radius for sources having $\theta \geqslant 6'$. Among the 683 main-catalog sources, we find that (1) 487 have matches in the 503-source A03 main catalog (the value of this column is that from Column 1 of Table 3(a) in A03), i.e., there are 196 (i.e., $683 - 487 = 196$) new main-catalog sources (see Section 2.3.7 for more details of these 196 new sources), compared to the A03 main catalog; (2) 45 have matches in the 78-source A03 supplementary catalog (the value of this column is that from Column 1 of Table 7(a) in A03 added with a prefix of "SP_"); and (3) 151 have no match in either the A03 main or supplementary catalogs, which are detected now thanks to our two-stage source-detection approach (the value of this column is set to −1). We refer readers to Section 2.3.5 for information on the 16 A03 main-catalog sources that are not included in our main catalog.

17. Columns 56 and 57 give the R.A. and decl. of the corresponding A03 source (shifted accordingly to be consistent with the K_s-band astrometric frame). Sources without an A03 match have these two columns set to "00 00 00.00" and "+00 00 00.0."

18. Columns 58–60 give the effective exposure times in units of seconds derived from the exposure maps (see Section 2.2.1) for the three standard bands. Effective count rates that are corrected for effects of vignetting, quantum-efficiency degradation, and exposure time variations can be obtained by dividing the counts in Columns 8–16 by the corresponding effective exposure times.

19. Columns 61–63 give the band ratio and the associated upper and lower errors, respectively. The band ratio is defined as the ratio of effective count rates between the hard and soft bands. Band-ratio errors are computed according to the numerical error-propagation method detailed in Section 1.7.3 of Lyons (1991), which avoids the failure of the standard approximate variance formula in the case of a small number of counts (e.g., see Section 2.4.5 of Eadie et al. 1971). Upper limits are computed for sources detected in the soft band but not the hard band, while lower limits are computed for sources detected in the hard band but not the soft band; for these sources, the upper and lower errors are set to the calculated band ratio. Band ratios and associated errors are set to −1.00 for sources with full band detections only.

20. Columns 64–66 give the effective photon index (Γ) and the associated upper and lower errors, respectively, assuming a power-law model with the Galactic column density that is given in Section 1. Γ is calculated based on the band ratio and a conversion between Γ and the band ratio. This conversion is derived utilizing the band ratios and photon indices computed by the AE-automated XSPEC-fitting procedure for sources with >200 full band counts. Upper limits are computed for sources detected in the hard band but not the soft band, while lower limits are computed for sources detected in the soft band but not the hard band; for these sources, the upper and lower errors are set to the calculated Γ. A value of $\Gamma = 1.4$ is assumed for low-count sources, being a representative value for faint sources that enables reasonable flux estimates, and the associated upper and lower errors are set to 0.00. Low-count sources are defined as those that were (1) detected in the soft band having <30 counts and not detected in the hard band, (2) detected in the hard band having <15 counts and not detected in the soft band, (3) detected in both the soft band and hard band, but having <15 counts in each, or (4) detected only in the full band.

21. Columns 67–69 give observed-frame fluxes in units of erg cm^{-2} s^{-1} for the three standard bands. Fluxes are calculated making use of the net counts (Columns 8–16), the effective exposure times (Columns 58–60), and Γ (Column 64), based on conversions derived from XSPEC-fitting results. Fluxes are not corrected for Galactic absorption or intrinsic absorption of the source. Negative fluxes denote upper limits.

22. Column 70 gives a basic estimate of the absorption-corrected, rest-frame 0.5–7 keV luminosity ($L_{0.5-7\,keV}$ or L_X) in units of erg s^{-1}. $L_{0.5-7\,keV}$ is computed utilizing the procedure presented in Section 3.4 of Xue et al. (2010). First, this procedure adopts a power law with both Galactic and intrinsic absorption to model the X-ray emission, thus obtaining an estimate of the intrinsic column density that reproduces the observed band ratio under the assumption of $\Gamma_{int} = 1.8$ for intrinsic AGN spectra; subsequently, it derives the absorption-corrected flux by means of correcting for both Galactic and intrinsic absorption and obtains $L_{0.5-7\,keV}$ using z_{final}. We note that $L_{0.5-8\,keV} = 1.066 \times L_{0.5-7\,keV}$ and $L_{2-10\,keV} = 0.721 \times L_{0.5-7\,keV}$, given the assumed $\Gamma_{int} = 1.8$. In this procedure, the observed band ratio is set to a value that corresponds to $\Gamma = 1.4$ for sources with full-band detections only; and for sources with upper or lower limits on the band ratio, their upper or lower limits are adopted. For sources without full band detections, their observed-frame full band fluxes are estimated by extrapolating their soft band or hard band fluxes assuming $\Gamma = 1.4$ and Galactic absorption. Crude luminosity estimates that have been derived this way are in general agreement (i.e., within $\approx 30\%$) with those derived through direct and detailed spectral fitting. Sources without z_{final} have this column set to −1.000.

23. Column 71 gives a basic estimate of likely source type: "AGN," "Galaxy," or "Star." A source is classified as an AGN once it satisfies at least one of the following four criteria (see Section 4.4 of X11 for reasoning and caveats): $L_{0.5-7\,keV} \geqslant 3 \times 10^{42}$ erg s^{-1} (i.e., luminous AGNs), $\Gamma \leqslant 1.0$ (i.e., obscured AGNs), $\log(f_X/f_R) > -1$ ($f_X = f_{0.5-7\,keV}$, $f_{0.5-2\,keV}$, or $f_{2-7\,keV}$; f_R is the *R*-band flux), and $L_{0.5-7\,keV} \gtrsim 3 \times (8.9 \times 10^{17} L_R)$ (L_R is the rest-frame 1.4 GHz monochromatic luminosity in units

Table 4
2 Ms CDF-N Main Catalog: Summary of Source Detections

Band (keV)	Number of Sources	Maximum Counts	Minimum Counts	Median Counts	Mean Counts
Full (0.5–7.0)	622	19748.4	8.1	66.2	342.8
Soft (0.5–2.0)	584	14227.3	5.4	35.0	234.7
Hard (2–7)	411	5540.6	7.7	57.5	181.4

Table 5
2 Ms CDF-N Main Catalog: Sources Detected in One Band but Not Another

Detection Band (keV)	Nondetection Full Band	Nondetection Soft Band	Nondetection Hard Band
Full (0.5–7.0)	…	91	219
Soft (0.5–2.0)	53	…	253
Hard (2–7)	8	80	…

of W Hz^{-1}). A source is classified as a star if (1) it has $z_{spec} = 0$, (2) it is one of the old late-type X-ray-detected CDF-N stars studied in Feigelson et al. (2004), or (3) it has a photometric classification of "Star" (see Columns 48 and 53) and is further confirmed through visual inspection of optical images. The sources that are not classified as either AGNs or stars are then regarded as "galaxies." There are 591 (86.5%), 75 (11.0%), and 17 (2.5%) of the 683 main-catalog sources identified as AGNs, galaxies, and stars, respectively.

24. Column 72 gives brief notes on the sources. Sources in close doubles or triples are annotated with "C" (a total of 27 such sources, which have overlapping polygonal extraction regions corresponding to ≈40%–75% EEFs; see Section 2.2.2); otherwise, sources are annotated with "....".

2.3.5. Comparison with the A03 Main-catalog Sources

Table 4 summarizes the source detections in the three standard bands for the main catalog. Of the 683 main-catalog sources, 622, 584, and 411 are detected in the full band, soft band, and hard band, respectively; as a comparison (see Table 4 of A03), of the 503 A03 main-catalog sources, 479, 451, and 332 are detected in the full, soft, and hard bands, respectively (note that A03 adopt an upper energy bound of 8 keV). As stated in Section 2.3.4 (see the description of Column 55), 487 of the main-catalog sources have matches in the A03 main catalog. For these 487 common sources, we find that the X-ray photometry derived in this work is in general agreement with that in A03, e.g., the median ratio between our and the A03 soft band count rates for the soft band detected common sources is 1.03, with an interquartile range of 0.92–1.11. The significant increase in the number of main-catalog sources, i.e., an increase of 683–487 = 196 new main-catalog sources, is mainly due to the improvements of our cataloging methodology that are summarized in Table 1, in particular, due to our two-stage source-detection approach. Indeed, we are able to detect fainter sources than A03 that are yet reliable, with median detected counts (see Table 4) in the three standard bands being ≈70% of those of A03.

Sixteen (i.e., 503–487 = 16) of the A03 main-catalog sources are not recovered in our main catalog, among which seven are recovered in our supplementary catalog (see Section 2.4). Among the nine A03 main-catalog sources that are not recovered in our main or supplementary catalogs, six sources not only have faint X-ray signatures, but also have multiwavelength counterparts with a few being bright, which indicates that most of them are likely real X-ray sources although they do not satisfy our main-catalog or supplementary-catalog source-selection criterion. The remaining three sources have marginal X-ray signatures and have no multi-wavelength counterparts, thus they are likely false detections.

Figure 10. Distributions of detected source counts for the 2 Ms CDF-N main-catalog sources in the full, soft, and hard bands. Sources with upper limits are not plotted. The vertical dotted lines indicate the median detected counts of 66.2, 35.0, and 57.5, for the full, soft, and hard bands, respectively (detailed in Table 4).

Table 5 summarizes the number of sources detected in one band but not another in the main catalog (see Table 5 of A03). There are 19, 53, and 8 sources detected only in the full, soft, and hard bands, in contrast to 5, 23, and 1 source(s) in the A03 main catalog, respectively.

2.3.6. Properties of Main-catalog Sources

Figure 10 presents the histograms of detected source counts in the three standard bands for the sources in the main catalog. The median detected counts are 66.2, 35.0, and 57.5 for the full, soft, and hard bands, respectively; and there are 232, 136, 67, and 41 sources with >100, >200, >500, and >1000 full band counts, respectively.

Figure 11 presents the histograms of effective exposure times in the three standard bands for all the 683 main-catalog sources. The median effective exposures are 1607.5, 1597.0, and 1653.6 ks for the full, soft, and hard bands, respectively.

Figure 12 presents the histograms of observed-frame X-ray fluxes in the three standard bands for the sources in the main catalog. The X-ray fluxes distribute within roughly four orders of magnitude, with median values of $8.1 \times 10^{-16}, 1.6 \times 10^{-16}$, and 1.1×10^{-15} erg cm^{-2} s^{-1} for the full, soft, and hard bands, respectively.

Figure 13 presents the histogram of the AE-computed binomial no-source probability P for the sources in the main catalog, with a total of 13 sources having no multiwavelength counterparts highlighted by shaded areas. The majority of the main-catalog sources have low P values that indicate significant detections, with a median P of 1.95×10^{-11} and an interquartile range of $0.00–2.36 \times 10^{-5}$. We find that 0.4% of the $\log P \leqslant -5$ sources have no ONIR counterparts, in
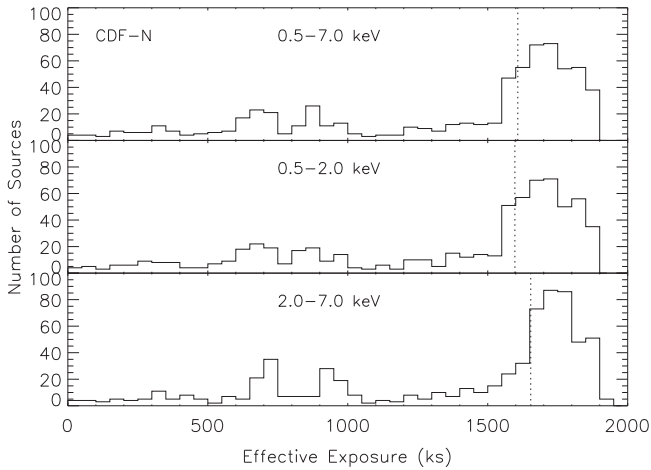
Figure 11. Distributions of effective exposure times for all the 683 2 Ms CDF-N main-catalog sources in the full, soft, and hard bands. The vertical dotted lines indicate the median effective exposures of 1607.5, 1597.0, and 1653.6 ks, for the full, soft, and hard bands, respectively.
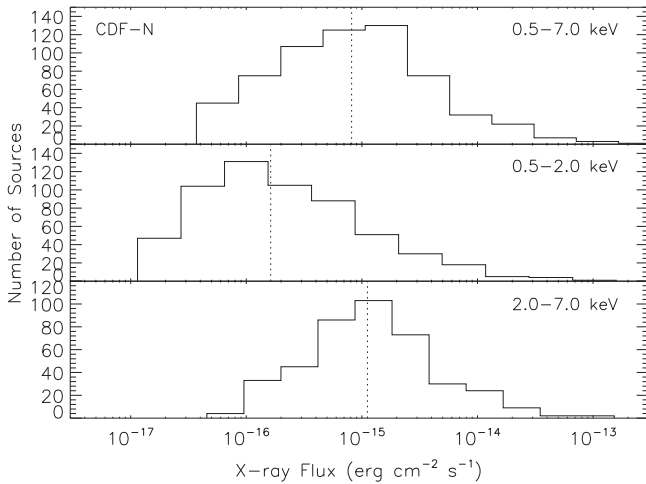
Figure 12. Distributions of observed-frame X-ray fluxes for the 2 Ms CDF-N main-catalog sources in the full, soft, and hard bands. Sources with upper limits are not plotted. The vertical dotted lines denote the median fluxes of $8.1 \times 10^{-16}, 1.6 \times 10^{-16}$ and 1.1×10^{-15} erg cm^{-2} s^{-1} for the full, soft, and hard bands, respectively.
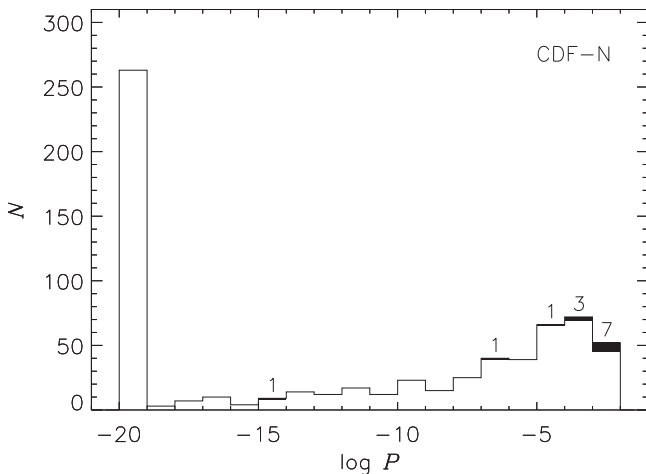
Figure 13. Distribution of the AE-computed binomial no-source probability P for the 2 Ms CDF-N main-catalog sources. The values of $\log P < -20$ are set to $\log P = -20$ for easy illustration. The shaded areas denote sources without multiwavelength counterparts, with their corresponding numbers annotated.

contrast to 5.8% of $\log P > -5$ sources lacking ONIR counterparts. Given the small false-match rate estimated in Section 2.3.3, a main-catalog source with a secure ONIR counterpart is almost certain to be real (note that sources without ONIR counterparts are more likely but not necessarily false detections).

Figures 14–16 display $25'' \times 25''$ postage-stamp images from the H-HDF-N Suprime-Cam R band (Capak et al. 2004), the GOODS-N WIRCam K_s band (Wang et al. 2010), and the SEDS IRAC 3.6 μm band (Ashby et al. 2013), overlaid with adaptively smoothed full-band X-ray contours for the main-catalog sources, respectively.

2.3.7. Properties of the 196 New Main-catalog Sources

Figure 17(a) displays the spatial distributions of the 196 new main-catalog sources (i.e., 154 new AGNs, 39 new galaxies, and 3 new stars that are all indicated as filled symbols) and the 487 old main-catalog sources (indicated as open symbols), whose colors are coded based on source types (red for AGNs, black for galaxies, and blue for stars) and whose symbol sizes represent different P values (larger sizes denote lower P values and thus higher source-detection significances). The vast majority of both the new and old galaxies are located within the GOODS-N area that has the deepest exposures (see Figure 3), as a result of their growing numbers at the faintest fluxes (e.g., Bauer et al. 2004; Lehmer et al. 2012). Both the new and old AGNs spread out more evenly within the entire CDF-N field. The above spatial distribution features are also evident in Figure 17(c), which shows the histograms of off-axis angles for different source types for the main-catalog sources.

Figures 17(e) and (f) show the observed source density as a function of off-axis angle for all the main-catalog sources and the new main-catalog sources, respectively. These two plots reveal, for either all or new sources, that (1) the source densities decline toward large off-axis angles due to the decreasing sensitivities (see Section 2.6.2); (2) overall, observed AGN densities are larger than observed galaxy densities; and (3) the galaxy source density approaches the AGN source density toward smaller off-axis angles where lower flux levels are achieved, due to the observed galaxy number counts having a steeper slope than the observed AGN number counts (e.g., Bauer et al. 2004; Lehmer et al. 2012). In the central CDF-N area of $\theta \leqslant 3'$, the observed source densities for all sources, all AGNs, and all galaxies reach $16,700^{+1600}_{-1500}$ deg^{-2}, $12,400^{+1400}_{-1300}$ deg^{-2}, and 4200^{+900}_{-700} deg^{-2}, respectively; and the observed source densities for all new sources, new AGNs, and new galaxies reach 6000^{+1000}_{-900} deg^{-2}, 3700^{+800}_{-700} deg^{-2}, and 2300^{+700}_{-500} deg^{-2}, respectively.

Figure 18 displays (a) observed-frame full-band flux versus adopted redshift, (b) absorption-corrected, rest-frame 0.5–7 keV luminosity versus adopted redshift, and (c) band ratio versus absorption-corrected, rest-frame 0.5–7 keV luminosity, for the new sources (indicated as filled circles) and old sources (indicated as open circles), respectively. We find that (1) the new sources typically have smaller X-ray fluxes and luminosities than the old sources (also see Figure 19); and (2) the median value of 1.40 of band ratios or upper limits on band ratios of the 128 new sources is larger than the corresponding median value of 0.77 of the 406 old sources (also see Figure 21). Following the example provided in Section 10.8.2 of Feigelson & Babu (2012), we further quantify the difference in band ratios between the above 128 new sources and 406 old
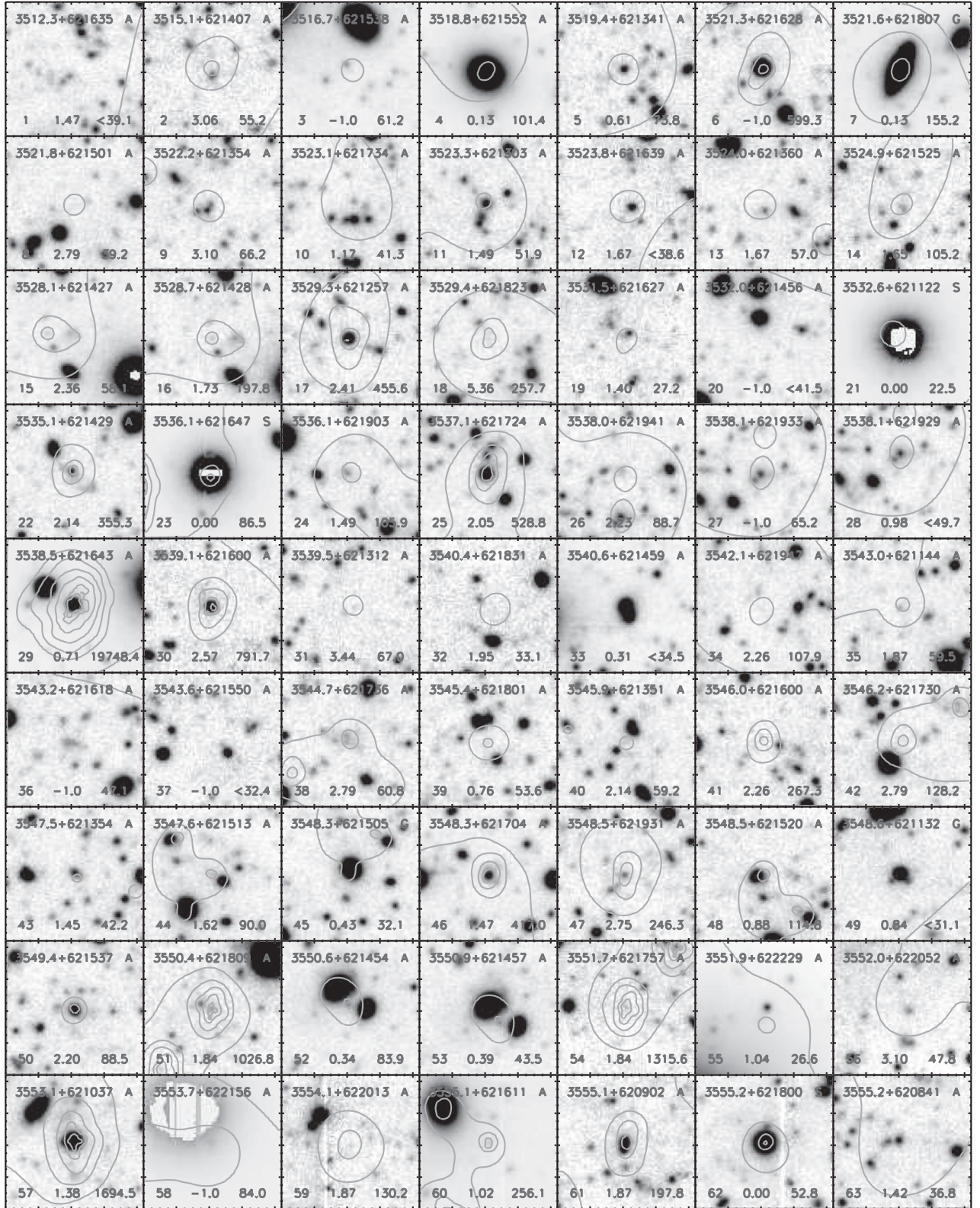
Figure 14. $25'' \times 25''$ postage-stamp images from the H-HDF-N Suprime-Cam *R* band (Capak et al. 2004) for the 2 Ms CDF-N main-catalog sources that are centered on the X-ray positions, overlaid with full-band adaptively smoothed X-ray contours that have a logarithmic scale and range from $\approx$0.003%–30% of the maximum pixel value. In each image, the labels at the top are the source name (the hours "12" of R.A. are omitted for succinctness) and source type (A = AGN, G = Galaxy, and S = Star); the bottom numbers indicate the source X-ray ID number, adopted redshift, and full-band counts or upper limit (with a "<" sign). There are cutouts (i.e., nearly plain white portions) in some images that are caused by stellar light-induced saturation. In some cases there are no X-ray contours present, either due to these sources being not detected in the full band or having low full-band counts leading to their observable emission in the adaptively smoothed image being suppressed by CSMOOTH. (An extended version of this figure is available.)
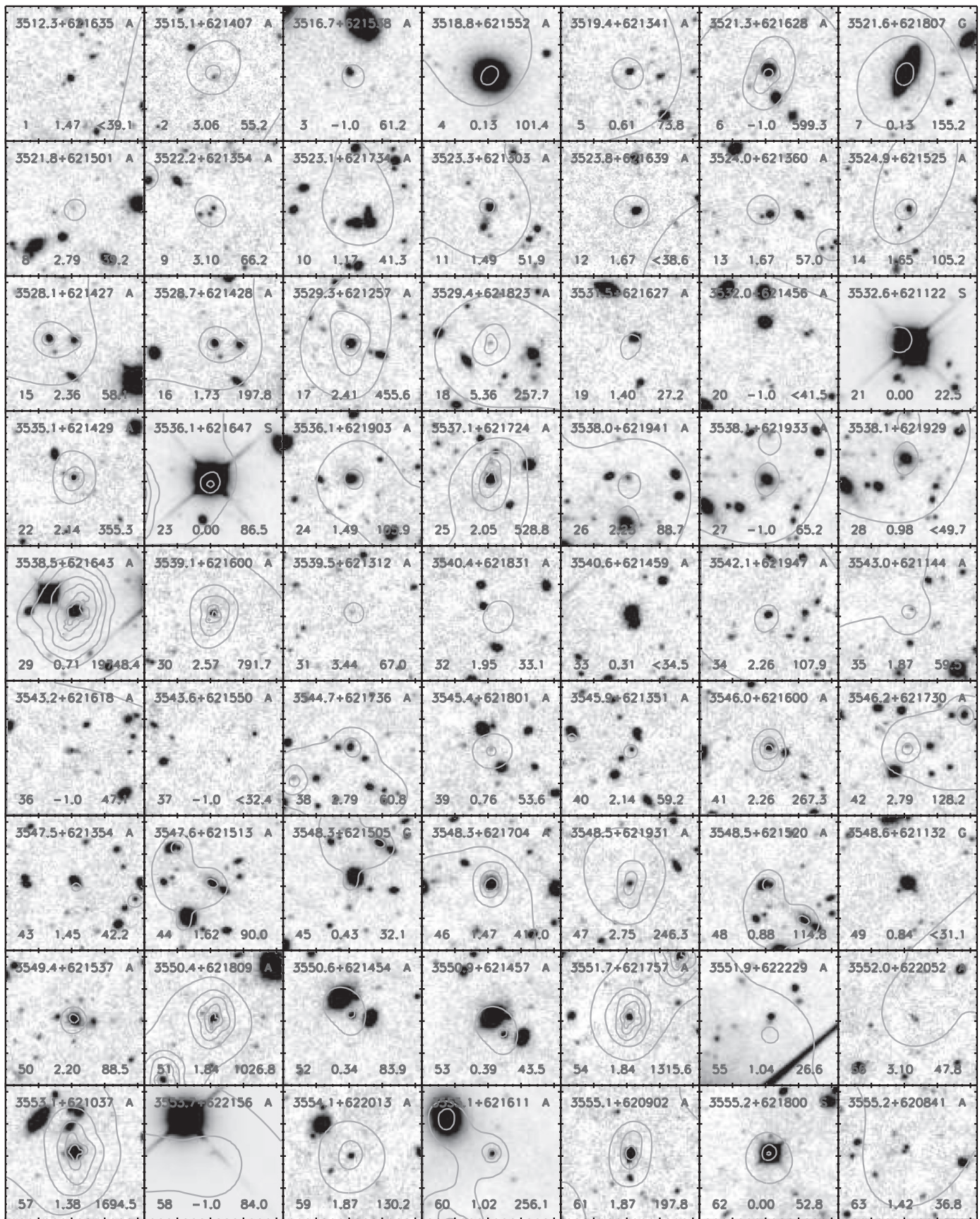
Figure 15. Same as Figure 14, but for the WIRCam K_s band (Wang et al. 2010). (An extended version of this figure is available.)
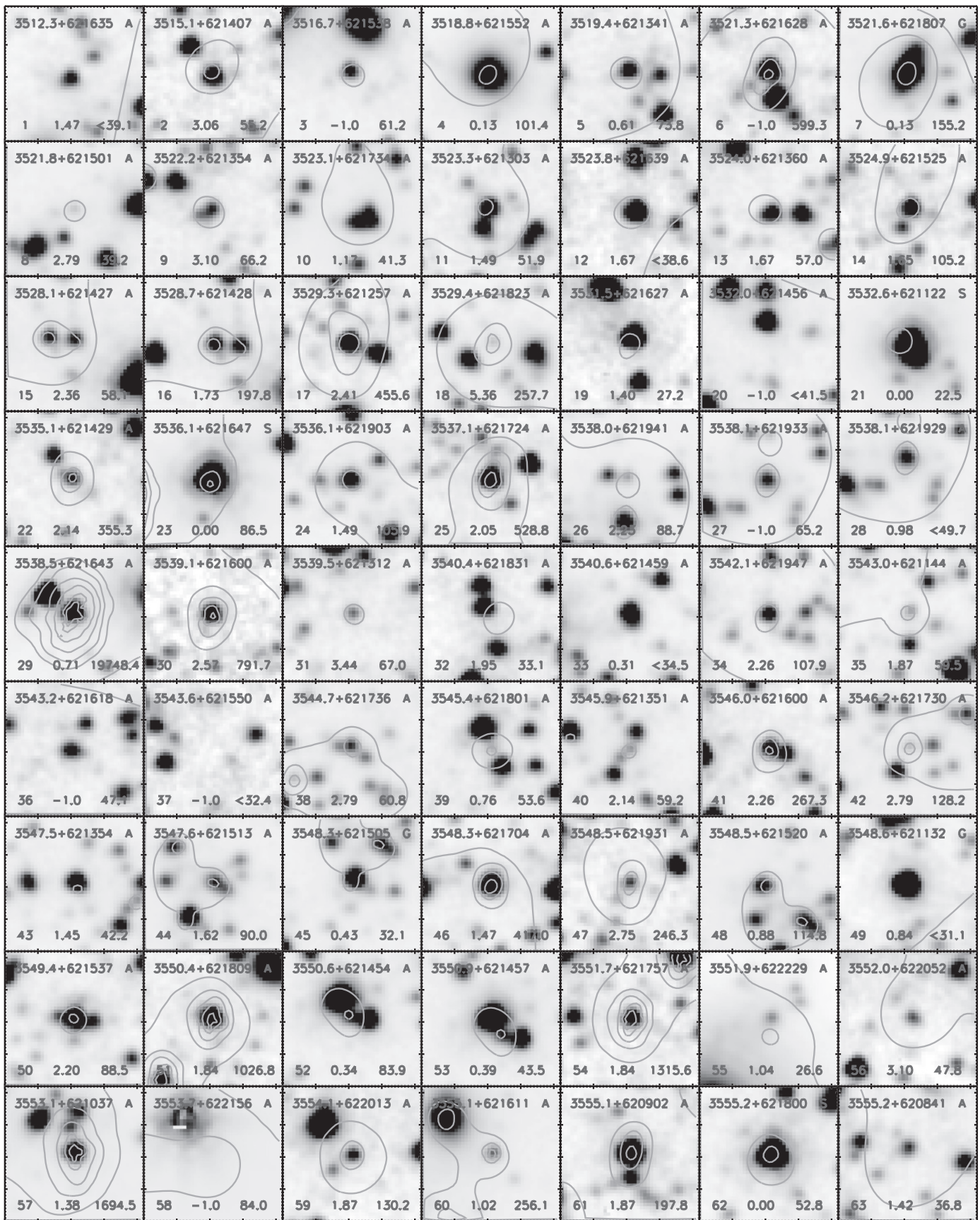
Figure 16. Same as Figure 14, but for the SEDS IRAC 3.6 μm band (Ashby et al. 2013). (An extended version of this figure is available.)
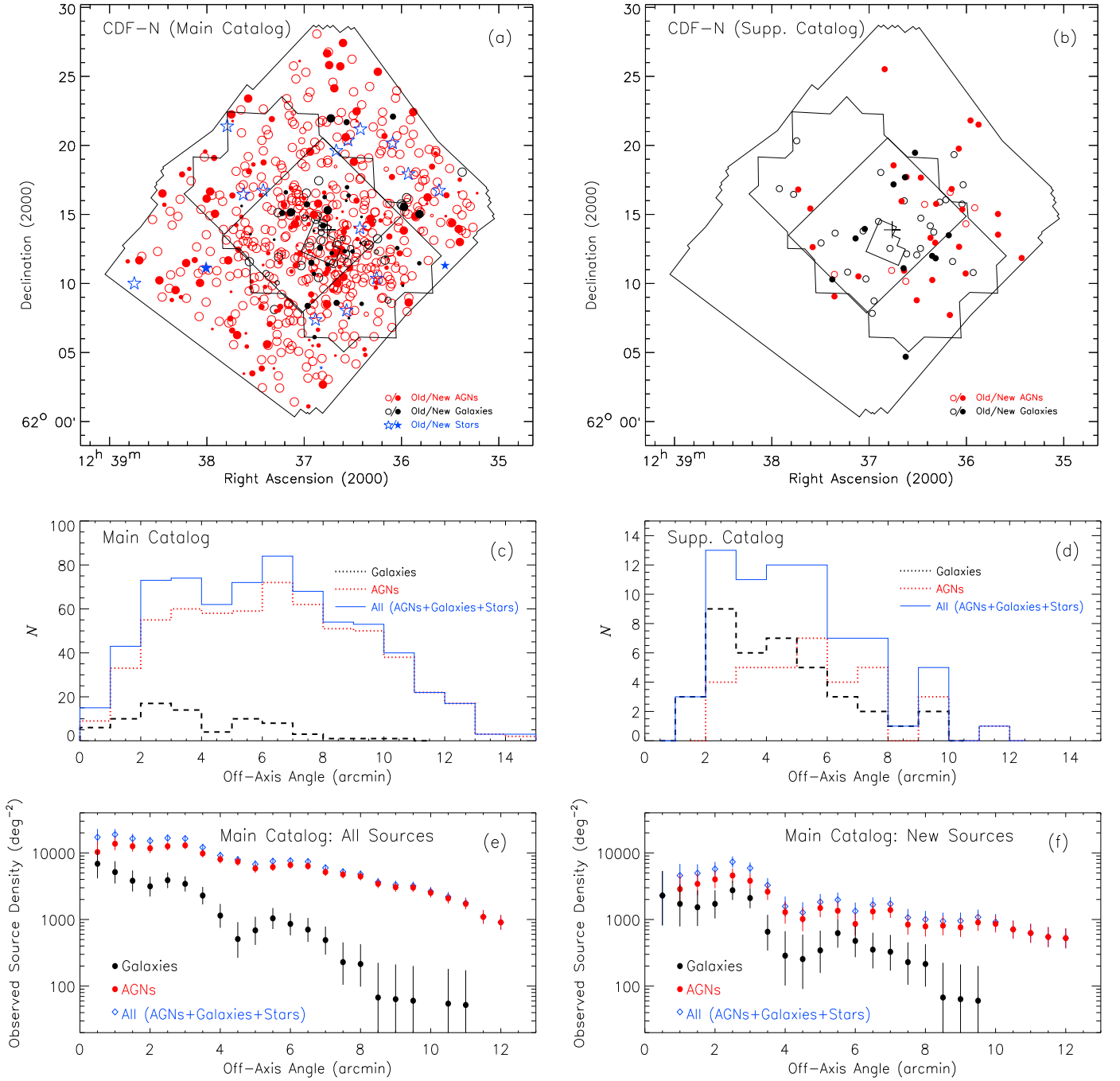
Figure 17. (Top) spatial distributions for (a) the 2 Ms CDF-N main-catalog sources and (b) the supplementary-catalog sources. Sources classified as AGNs, galaxies, and stars are plotted as red, black, and blue symbols, respectively. Open symbols indicate old sources that were previously detected in (a) the A03 main catalog or (b) the A03 main or supplementary catalog, while filled symbols indicate new sources that were not previously detected in the A03 main and/or supplementary catalog. The regions and the plus sign have the same meanings as those in Figure 2. In panel (a), larger symbol sizes indicate lower AE binomial no-source probabilities, ranging from $\log P > -3$, $-4 < \log P \leqslant -3$, $-5 < \log P \leqslant -4$, to $\log P \leqslant -5$; while in panel (b), all sources have $\log P > -3$ and are plotted as symbols of the same size. (Middle) distributions of off-axis angles for different source types for (c) the main-catalog sources and (d) the supplementary-catalog sources. (Bottom) observed source densities broken down into different source types as a function of off-axis angle (θ) for (e) all the 2 Ms CDF-N main-catalog sources and (f) the new main-catalog sources, which are calculated in bins of $\Delta\theta = 1'$ and whose 1σ errors are computed utilizing Poisson statistics.

sources that involve censored data, utilizing survival-analysis 2-sample tests (the logrank test and the Peto & Peto modification of the Gehan-Wilcoxon test) that are implemented in the function SURVDIFF in the public domain R statistical software system (R Core Team 2015). Both of the 2-sample tests give $p = 0.0$ results, indicating that there is a significant difference in band ratios between the above new and old sources. Together, the above observations indicate that our

improved cataloging methodology allows us to probe fainter obscured sources than A03.

Figure 19 presents histograms of observed-frame full-band flux and absorption-corrected, rest-frame 0.5–7 keV luminosity for the new AGNs and galaxies (main panels), as well as the old AGNs and galaxies (insets). It is apparent that AGNs and galaxies have disparate distributions of flux and luminosity, and overall galaxies become the numerically dominant
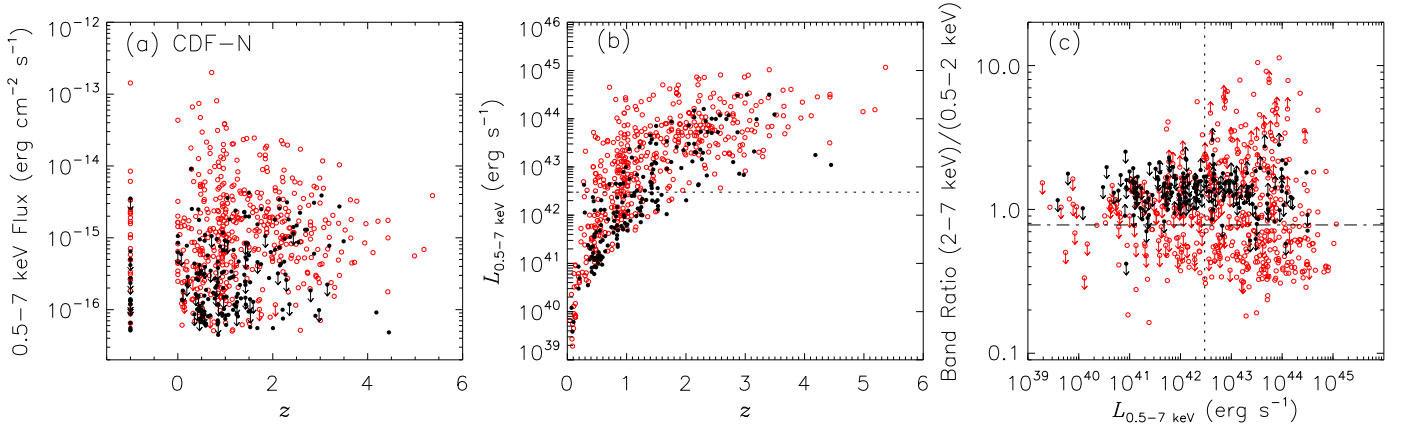
Figure 18. (a) Observed-frame full-band flux vs. adopted redshift, (b) absorption-corrected, rest-frame 0.5–7 keV luminosity vs. adopted redshift, and (c) band ratio vs. absorption-corrected, rest-frame 0.5–7 keV luminosity for the 2 Ms CDF-N main-catalog sources. Red open circles indicate old sources while black filled circles indicate new sources. Arrows denote limits. In panel (b), sources having no redshift estimates are not plotted; in panel (c), sources having no redshift estimates or sources having only full-band detections are not plotted. The dotted lines in panels (b) and (c) and the dashed–dotted line in panel (c) correspond to the threshold values of two AGN-identification criteria, $L_{0.5-7\,\mathrm{keV}} \geqslant 3 \times 10^{42}$ erg s^{-1} and $\Gamma \leqslant 1.0$.
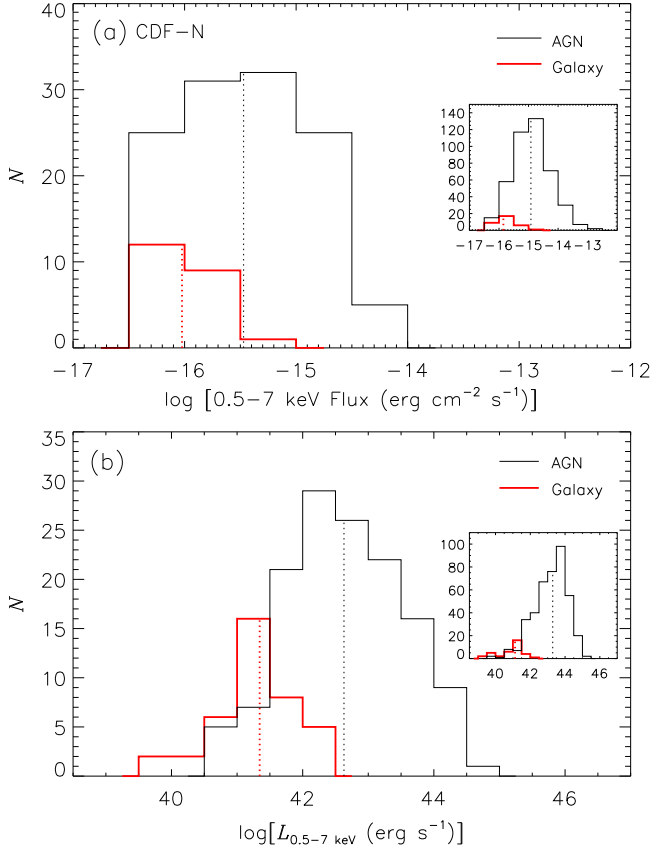
Figure 19. Histograms of (a) observed-frame full-band flux and (b) absorption-corrected, rest-frame 0.5–7 keV luminosity for the new 2 Ms CDF-N main-catalog sources. The insets display results for the old main-catalog sources. The vertical dotted lines indicate the median values. In panel (a), sources without full-band detections are not included; in panel (b), sources without redshift estimates are not included.

population at 0.5–7 keV luminosities less than $\approx 10^{41.5}$ erg s^{-1}, no matter whether the new or old sources are considered.

Figure 20(a) displays the band ratio as a function of full-band count rate for the new sources (indicated as filled symbols) and the old sources (indicated as open symbols), with the large crosses, triangles, and diamonds representing the

average (i.e., stacked) band ratios[22] for all AGNs, all galaxies, and all sources (counting both AGNs and galaxies), respectively. The overall average band ratio is, as expected, dominated by AGNs, which has a rising-leveling-off-declining shape toward low full-band count rates that is in general agreement with that seen in, e.g., Figure 14 of A03 and Figure 19 of X11 (see Section 4.7 of X11 for the relevant discussion on such a shape). Figure 20(b) presents the fraction of new sources as a function of full-band count rate for the sources in the main catalog. From full-band count rates of $\approx 10^{-3}$ count s^{-1} to $\approx 5 \times 10^{-6}$ count s^{-1}, the fraction of new sources rises monotonically from 0% to $\approx 57\%$.

Figure 21 presents the average band ratio in bins of adopted redshift and X-ray luminosity for the new AGNs, old AGNs, new galaxies, and old galaxies, respectively. A couple of observations can be made, e.g.: (1) the new AGNs have larger band ratios than the old AGNs no matter which bin of redshift or X-ray luminosity is considered, with the only exception being the lowest luminosity bin, reflecting the rise of obscured AGNs toward faint fluxes (e.g., Bauer et al. 2004; Lehmer et al. 2012); (2) for the lowest redshift bin and the two lowest luminosity bins where both the AGN and galaxy results are available for comparison, the AGNs have larger band ratios than the galaxies, no matter if they are old or new ones; and (3) in the lowest luminosity bin of $\log(L_{\mathrm{X}}) < 41.5$, the new galaxies have a smaller average band ratio than the old galaxies, while in a higher luminosity bin of $41.5 \leqslant \log(L_{\mathrm{X}}) < 42.5$, the trend is reversed (but note the relatively small numbers of sources considered in this higher luminosity bin).

Figure 22(a) presents the Suprime-Cam R-band magnitude versus the full-band flux for the new sources (indicated as filled symbols) and old sources (indicated as open symbols), as well as the approximate flux ratios for AGNs and galaxies (see the description of Column 71 for AGN identification), where the sources are color-coded with red for AGNs, black for galaxies, and blue for stars, respectively. As a comparison, Figure 22(c) presents the IRAC 3.6 μm magnitude versus the full-band flux for the new sources and old sources, since a larger fraction of

---

[22] We note that the stacked averages only indicate the mean properties and cannot represent the full distribution of the stacked sample.
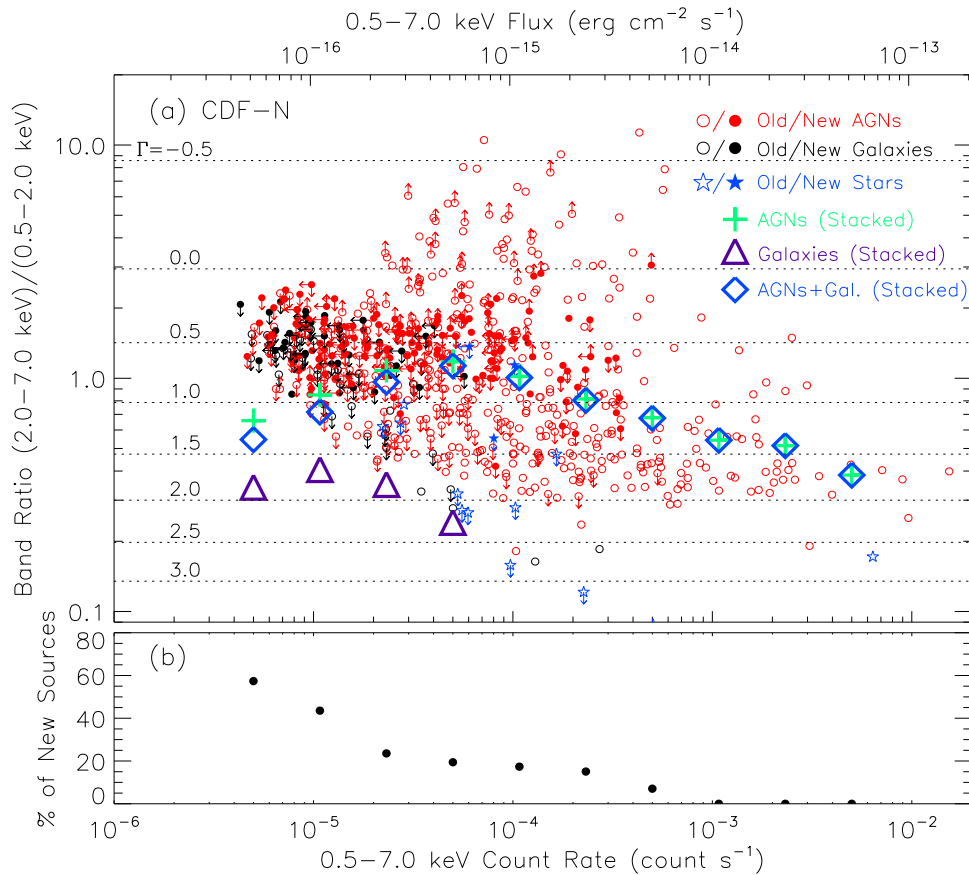
Figure 20. (a) Band ratio vs. full-band count rate for the 2 Ms CDF-N main-catalog sources. For reference, the top *x*-axis displays representative full-band fluxes that are derived using full-band count rates given an assumed $\Gamma = 1.4$ power law. The meanings of symbols of different types and colors are indicated by the legend. Arrows indicate limits. Sources with only full-band detections are not plotted; there are only 19 ($19/683 = 2.8\%$) such sources, the exclusion of which would not affect our results significantly. Large crosses, triangles, and diamonds denote average/stacked band ratios as a function of full-band count rate that are derived in bins of $\Delta\log(\text{Count Rate}) = 0.6$, for AGNs, galaxies, and both AGNs and galaxies, respectively. Horizontal dotted lines indicate the band ratios that correspond to given effective photon indexes. (b) Fraction of new sources as a function of full-band count rate for the 2 Ms CDF-N main-catalog sources, computed in bins of $\Delta\log(\text{Count Rate}) = 0.6$.

the main-catalog sources have IRAC 3.6 μm band counterparts than Suprime-Cam *R*-band counterparts (i.e., 87.0% versus 68.5%; see the description of Columns 23–40). We note that the flux ratio of $\log(f_X/f_{3.6\,\mu m})$ can also be used to separate AGNs from galaxies when the classification threshold is carefully calibrated (e.g., Wang et al. 2013). Overall, a total of 591 (86.5%) of the sources in the main catalog are likely AGNs, the majority of which lie in the region expected for relatively luminous AGNs that have $\log(f_X/f_R) > -1$ (i.e., dark gray areas in Figure 22(a)); among these 591 AGNs, 154 (26.1%) are new. A total of 75 (11.0%) of the sources in the main catalog are likely galaxies, and by selection all of them lie in the region expected for normal galaxies, starburst galaxies, and low-luminosity AGNs that have $\log(f_X/f_R) \leqslant -1$ (i.e., light gray areas in Figure 22(a)); among these 75 sources, 39 (52.0%) are new. Only 17 (2.5%) of the sources in the main catalog are likely stars, with all but one having low X-ray-to-optical flux ratios; among these 17 stars, 3 are new. Among the new sources, normal and starburst galaxies total a fraction of 19.9%, as opposed to 7.4% if the old sources are considered, which is expected due to galaxies having a steeper number-count slope than AGNs (e.g., Bauer et al. 2004; Lehmer et al. 2012).
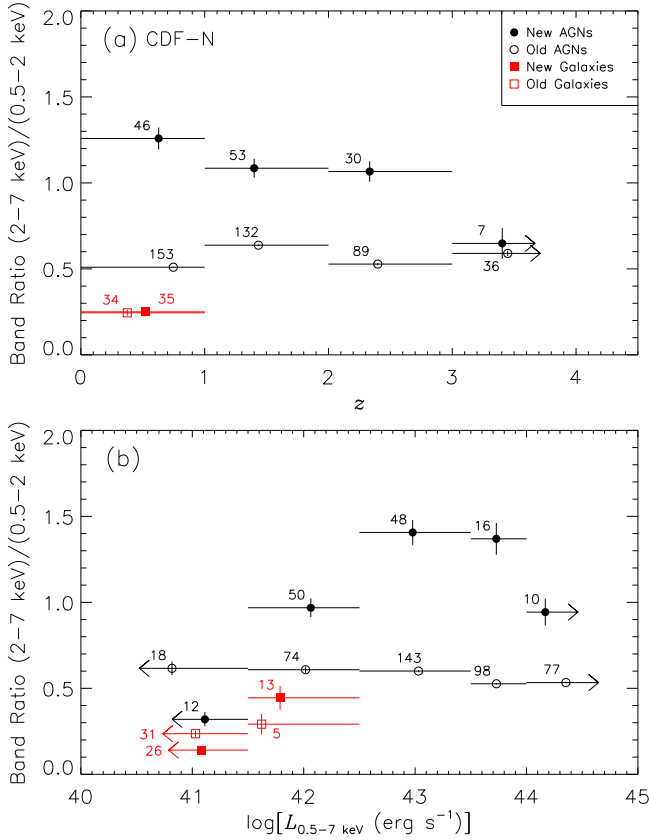
Figure 23 presents the histograms of X-ray-to-optical flux ratio for the new AGNs, old AGNs, new galaxies, and old

galaxies, respectively. It is apparent that (1) the new AGNs have a similar overall distribution of *R*-band magnitude to the old AGNs, but generally have smaller X-ray-to-optical flux ratios than the old AGNs; and (2) the new galaxies generally have fainter *R*-band magnitudes and larger X-ray-to-optical flux ratios than the old galaxies.

2.4. Supplementary Near-infrared Bright Chandra Source Catalog

2.4.1. Supplementary Catalog Production

Among the 320 (i.e., 1003–683 = 320) candidate-list X-ray sources that do not satisfy the main-catalog source-selection criterion of $P < 0.004$, 167 are of moderate significance with $0.004 \leqslant P < 0.1$. In order to retrieve genuine X-ray sources from this sample of 167 sources, we create a supplementary catalog that consists of the subset of these sources having bright near-infrared counterparts, because such *Chandra* sources are likely real, thanks to the comparatively low spatial density of near-infrared bright sources. Similar prior-based source-searching methods have been widely used (e.g., Richards et al. 1998; A03; L05; Luo et al. 2008; X11), and they allow for detections of real X-ray sources with lower significances. We match these 167 *Chandra* sources with the $K_s \leqslant 22.9$ mag sources in the GOODS-N WIRCam K_s-band

Figure 21. Average/stacked band ratios in bins of (a) redshift ($0 < z < 1$, $1 \leqslant z < 2$, $2 \leqslant z < 3$, and $z \geqslant 3$) and (b) absorption-corrected, rest-frame 0.5–7 keV luminosity [$\log(L_X) < 41.5$, $41.5 \leqslant \log(L_X) < 42.5$, $42.5 \leqslant \log(L_X) < 43.5$, $43.5 \leqslant \log(L_X) < 44.0$, and $\log(L_X) \geqslant 44.0$] for the new and old 2 Ms CDF-N main-catalog sources. The meanings of the symbols are indicated by the legend. In each bin, the median redshift or X-ray luminosity is used for plotting; the number of stacked sources is annotated.

2.4.2. Properties of Supplementary-catalog Sources

Figure 17(b) displays the spatial distribution of the 72 supplementary-catalog sources, with the 38 new sources denoted as filled symbols; and Figure 17(d) presents the histograms of off-axis angles for different source types for the supplementary-catalog sources. Figures 22(b) and (d) present the Suprime-Cam R-band magnitude and the SEDS IRAC 3.6 μm magnitude versus the full-band flux for the supplementary-catalog sources, respectively. Among the 72 supplementary-catalog sources, 34 (47.2%) are likely AGNs; 38 (52.8%) are likely galaxies, which by selection are all located in the region expected for normal galaxies, starburst galaxies, and low-luminosity AGNs; and there are no likely stars. A total of 69 (95.8%) of these 72 sources have either $z_{\rm spec}$'s or $z_{\rm phot}$'s, ranging from 0.083 to 3.583 with a median redshift of 0.857.

2.5. Completeness and Reliability Analysis

We have carried out simulations to make an assessment of the completeness and reliability of our main catalog.

2.5.1. Generation of Simulated Data

First, we construct a mock catalog covering the entire CDF-N field and extending well below its detection limits (see Section 2.6.2). In this mock catalog, we follow Miyaji et al. (2007) to include realistic source clustering when assigning source coordinates. We randomly assign simulated AGN and galaxy fluxes following the soft-band log N–log S relations in the Gilli et al. (2007) AGN population-synthesis model and the Ranalli et al. (2005) galaxy "peak-M" model, respectively. We convert soft-band fluxes of simulated AGNs and galaxies into full-band fluxes assuming $\Gamma = 1.4$ and $\Gamma = 2.0$ power-law spectra, respectively. Second, we utilize the MARX simulator to construct source event lists from 20 simulated ACIS-I observations of the mock catalog, each under the same observational configuration (e.g., aim point, roll angle, exposure time, aspect solution file) as one of the CDF-N observations. Third, we extract corresponding background event files from the real CDF-N event files by masking all events relevant to the main-catalog and supplementary-catalog sources and then filling the masked regions with events that obey the local background distribution. We randomly remove $\approx$0.7%[23] of the events in each background event file in order to avoid counting twice the contribution of undetectable faint sources that is present in both the source and background event files. We then combine the above corresponding source and background event files to produce a set of 20 simulated ACIS-I observations that closely mimic the real CDF-N observations. Finally, following Section 2.2, we obtain a simulated merged 2 Ms CDF-N event file, construct images for the three standard bands, run WAVDETECT (sigthresh = 10^{-5}) to generate a candidate-list catalog, and make use of AE to extract photometry (including P values) for the candidate-list sources.

2.5.2. Completeness and Reliability

We define completeness as the ratio between the number of detected sources that satisfy a specific detection criterion of

catalog utilizing a matching radius of 1.″2. The choices of $0.004 \leqslant P < 0.1$, the K_s-band catalog and cutoff magnitude, and the matching radius are made to maximize the number of included sources while keeping the expected number of false sources reasonably low. A total of 72 near-infrared bright X-ray sources are identified this way, with $\approx$6.0 false matches expected (i.e., a false-match rate of 8.3%). Our supplementary catalog includes 7 A03 main-catalog sources that are not recovered in our main catalog and 27 A03 supplementary optically bright (i.e., $R \lesssim 23.0$ mag) sources, thus resulting in a total of $72-7-27 = 38$ new supplementary-catalog sources that are not present in either of the A03 catalogs. A point worth noting is that the vast majority (72 out of 79; 91.1%) of the A03 supplementary optically bright sources are included either in our main catalog (45 sources) or supplementary near-infrared bright catalog (the aforementioned 27 sources).

Our 72-source supplementary catalog is presented in Table 6, in the same format as Table 3 (see Section 2.3.4 for the details of each column). A source-detection criterion of $P < 0.1$ is adopted for photometry-related calculations for the supplementary-catalog sources; and the multiwavelength identification-related columns (i.e., Columns 18–22) are set to the WIRCam K_s-band matching results.

---

[23] This $\approx$0.7% is a typical ratio between the summed full-band counts of undetectable faint sources and the 2 Ms CDF-N total full-band background counts (see Table 8 in Section 2.6.1), assuming a range of reasonable effective photon indexes for the flux-count-rate conversions.
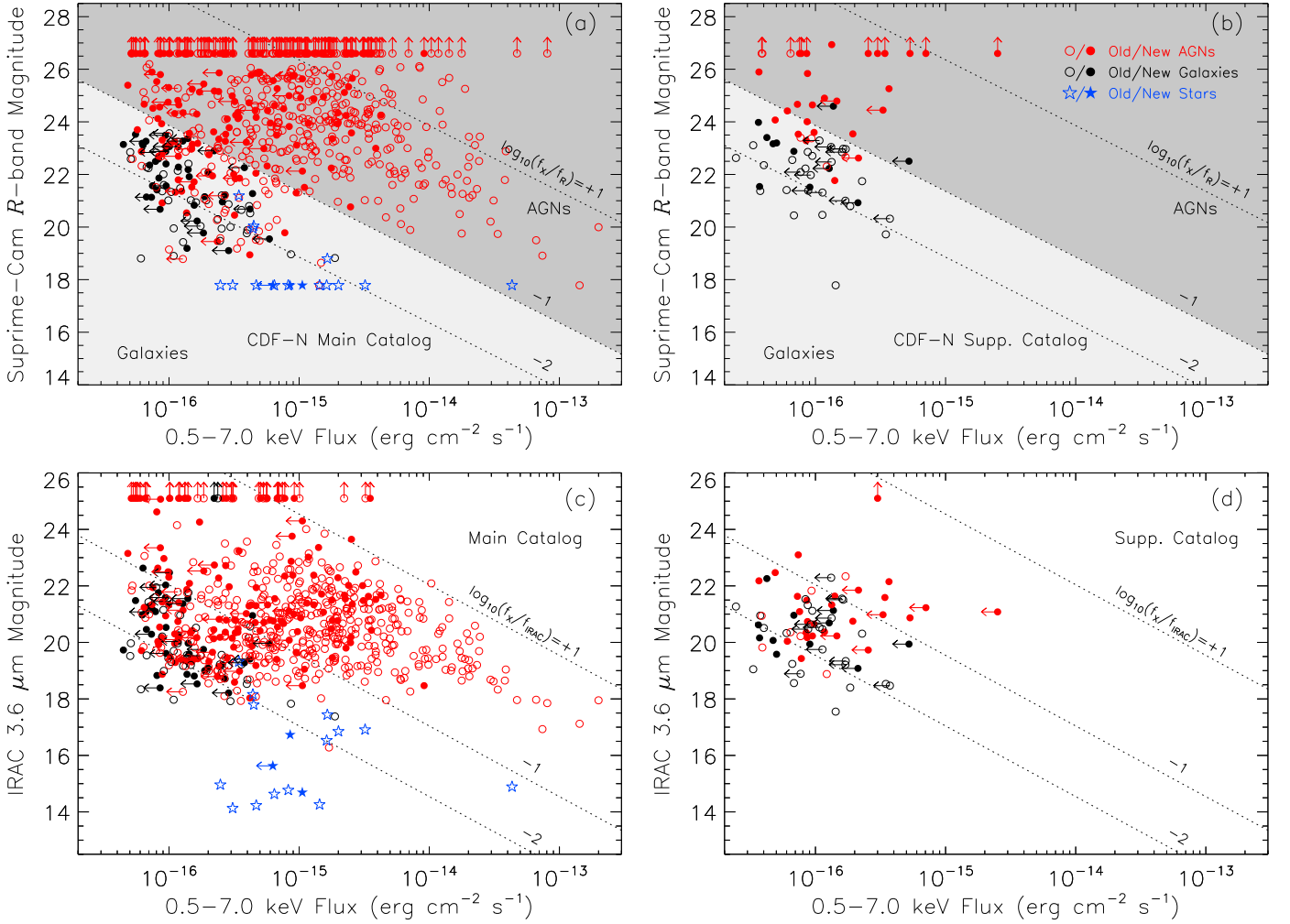
Figure 22. (Top) Suprime-Cam *R*-band magnitude vs. full-band flux for (a) the 2 Ms CDF-N main-catalog sources and (b) the supplementary-catalog sources. (Bottom) IRAC 3.6 μm magnitude vs. full-band flux for (c) the 2 Ms CDF-N main-catalog sources and (d) the supplementary-catalog sources. The meanings of the symbols of different types and colors are indicated by the legend. Arrows denote limits. In panels (a) and (b), diagonal dotted lines indicate constant full-band-to-*R* flux ratios, and shaded areas represent approximate flux ratios for AGNs (dark gray) and galaxies (light gray). In panels (c) and (d), diagonal dotted lines indicate constant full-band-to-IRAC-3.6 μm flux ratios. Note that the stars lined up at *R* = 17.8 mag have their *R*-band magnitudes set to this value for plotting purposes as they are assigned negative magnitudes in the *R*-band catalog due to saturation (*R* = 17.8 is one magnitude brighter than the brightest non-saturated stars in the *R*-band catalog).

$P < P_0$ and the number of input simulated sources, above a given source-count limit that applies to both detected sources and input simulated sources. We define reliability as 1 minus the ratio between the number of spurious sources that arise from noise fluctuations and the number of input simulated sources, above the same given source-count limit. Figure 24 displays the completeness and reliability as a function of the AE-computed binomial no-source probability within the central $\theta \leqslant 6'$ region and the entire CDF-N field, for the simulations in the full, soft, and hard bands, for sources with at least 15 and 8 counts, respectively. The case of 8 counts is roughly our on-axis (i.e., $\theta \lesssim 3'$) source-detection limit in the full and hard bands.

It seems clear from Figure 24 that (1) in all panels, as expected, each completeness curve goes up and each reliability curve goes down toward large P threshold values, and the completeness level for the case of 15 counts is higher than that for the case of 8 counts; and (2) the completeness level for the case of either 15 counts or 8 counts within the central $\theta \leqslant 6'$ region is higher than the corresponding completeness level in the entire CDF-N field. At our adopted main-catalog P

threshold of 0.004, the completeness levels within the central $\theta \leqslant 6'$ region are 100.0% and 82.5% (full band), 100.0% and 95.4% (soft band), and 87.1% and 68.7% (hard band) for sources with $\geqslant 15$ and $\geqslant 8$ counts, respectively. The completeness levels for the entire CDF-N field are 89.1% and 65.6% (full band), 95.8% and 77.2% (soft band), and 74.4% and 57.3% (hard band) for sources with $\geqslant 15$ and $\geqslant 8$ counts, respectively. At our adopted main-catalog P threshold of 0.004, the reliability level ranges from 98.7% to 99.6% for all panels; we estimate that, in the main catalog (i.e., the entire CDF-N field), there are about 5, 3, and 2 false detections with $\geqslant 15$ counts in the full, soft, and hard bands, and about 5, 4, and 3 false detections with $\geqslant 8$ counts in the full, soft, and hard bands, respectively.

Figure 25 presents the completeness as a function of flux given the main-catalog $P < 0.004$ criterion for the full, soft, and hard band simulations. The three curves of completeness versus flux that are derived from the simulations (dashed lines) approximately track the normalized sky coverage curves that are derived from the real CDF-N observations (solid curves). Table 7 presents the flux limits corresponding to four specific
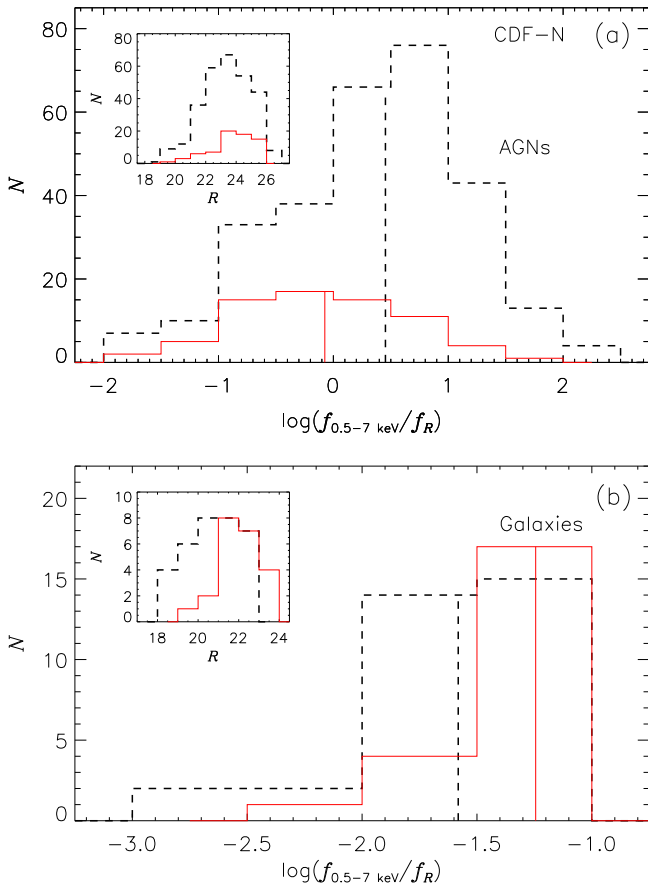
Figure 23. Histograms of X-ray-to-optical (*R* band) flux ratios for (a) the new 2 Ms CDF-N main-catalog AGNs (solid histogram) and old AGNs (dashed histogram) and (b) new galaxies (solid histogram) and old galaxies (dashed histogram), with median flux ratios denoted by vertical lines. The insets display the histograms of *R*-band magnitude for new sources (solid histograms) and old sources (dashed histograms). Only sources with both full-band and *R*-band detections are plotted.

completeness levels in the full, soft, and hard bands, which are denoted as horizontal dotted lines in Figure 25.

2.6. Background and Sensitivity Analysis

2.6.1. Background Map Creation

To create background maps for the three standard band images, we first mask the 683 main-catalog sources and the 72 supplementary-catalog sources, utilizing circular apertures that have radii of 1.5 (2.0) times the ≈99% PSF EEF radii for sources with full-band counts below (above) 10,000 (note that there are 4 main-catalog sources with >10,000 full-band counts). We subsequently fill in the masked areas of the sources with background counts, which obey the local probability distribution of counts lying within an annulus that has an inner radius that is the aforementioned masking radius and has an outer radius of 2.5 (3.0) times the ≈99% PSF EEF radius for sources with full-band counts below (above) 10,000. Table 8 summarizes the background properties including the mean background, total background, and count ratio between background counts and detected source counts for the three standard bands. 91.7%, 97.1%, and 94.2% of the pixels have zero background counts in the background maps for the full, soft, and hard bands, respectively. The values in Table 8 are systematically slightly lower than those reported in Table 8

of A03, mainly due to the facts that we adopt a smaller upper energy bound of 7 keV than the value of 8 keV adopted in A03 and that we adopt a more stringent approach for data filtering (see Section 2.1). Figure 26 displays the full-band background map.

Figure 27 presents the mean *Chandra* background spectra that are calculated for the 683 main-catalog sources in various bins of off-axis angle, using the individual background spectra extracted in Section 2.2.2. We find that (1) the shapes of the mean *Chandra* background spectra remain largely the same across the entire CDF-N field given the uncertainties, especially as far as the $\gtrsim 1$ keV parts of the spectra are concerned (with $\lesssim 10\%$ variations between the shapes); and (2) for the $\lesssim 1$ keV parts of the mean background spectra, shape variations seem apparent (up to ≈20%), with some hint of the spectra for sources with $\theta < 6'$ lying slightly above the spectra for sources with $\theta \geqslant 6'$.

Our background maps and background spectra have contributions of various origins that include the unresolved cosmic X-ray background, particle background, and instrumental background (e.g., Markevitch et al. 2003). In this work, we are only interested in the total background, thereby not distinguishing between these different background components. We refer readers to other works (e.g., Hickox & Markevitch 2006) that carefully characterize, distinguish, and measure these individual *Chandra* background components that are key to their specific scientific goals.

2.6.2. Sensitivity Map Creation

Given the above background maps and the main-catalog source-detection criterion of $P < 0.004$, we can measure B_{src} and B_{ext} to obtain the minimum number of counts (S) required for a detection according to the binomial no-source probability equation (i.e., Equation (1) in Section 2.3.1), and then create sensitivity maps in the three standard bands for the main catalog to assess the sensitivity as a function of position across the entire field. We first determine B_{src} in the background maps utilizing circular apertures of ≈90% PSF EEF radii. We then derive B_{ext} as follows to mimic the AE behavior of extracting background counts for the main-catalog sources: for a given pixel in the background map, we calculate its off-axis angle (θ_p) and set the B_{ext} value to the maximum B_{ext} value (corresponding to the highest sensitivity) of the main-catalog sources that lie within an annulus with an inner/outer radius of $\theta_p - 0\farcm25/\theta_p + 0\farcm25$. Subsequently, we numerically solve Equation (1) to obtain the minimum counts S in the source-extraction region that lead to a value of $P < 0.004$. Finally, we create sensitivity maps for the main catalog utilizing the exposure maps, under the assumption of a $\Gamma = 1.4$ power-law model with Galactic absorption. We find that there are 12, 15, and 9 main-catalog sources in the three standard bands that lie typically $\lesssim 10\%$ below the corresponding derived sensitivity limits, respectively, which is likely due to background fluctuations and/or their real Γ values differing significantly from the assumed $\Gamma = 1.4$.

Figure 28 displays the full-band sensitivity map for the main catalog, and Figure 29 presents plots of survey solid angle versus flux limit in the three standard bands given $P < 0.004$. It is clear that higher sensitivities are reached at smaller off-axis angles and thus within smaller survey solid angles. We find the mean sensitivity limits achieved in the central ≈1 arcmin² area at the average aim point to be ≈3.5 × 10^{-17}, 1.2 × 10^{-17}, and

Table 6
2 Ms CDF-N Supplementary Near-infrared Bright *Chandra* Source Catalog

| No. (1)	α_{2000} (2)	δ_{2000} (3)	$\log P$ (4)	WAVDETECT (5)	Pos Err (6)	Off-axis (7)	Full Band (8)	Full Band Upp Err (9)	Full Band Low Err (10)	Soft Band (11)	Soft Band Upp Err (12)	Soft Band Low Err (13)
1	12 35 25.28	+62 11 53.8	−1.1	−5	2.2	9.60	18.2	−1.0	−1.0	3.9	4.3	2.9
2	12 35 39.87	+62 15 05.7	−2.4	−5	0.8	7.75	24.5	11.7	10.2	11.5	7.3	5.9
3	12 35 39.87	+62 13 35.9	−2.4	−5	0.7	7.68	36.2	15.7	14.5	14.1	9.2	8.0
4	12 35 51.76	+62 21 34.5	−2.2	−5	0.9	9.86	28.2	13.2	12.0	11.3	7.9	6.7
5	12 35 54.31	+62 15 33.1	−2.2	−5	0.6	6.19	26.0	12.4	11.2	11.4	7.8	6.5

Note. The full table contains 72 columns of information for the 72 X-ray sources.

(This table is available in its entirety in machine-readable form.)
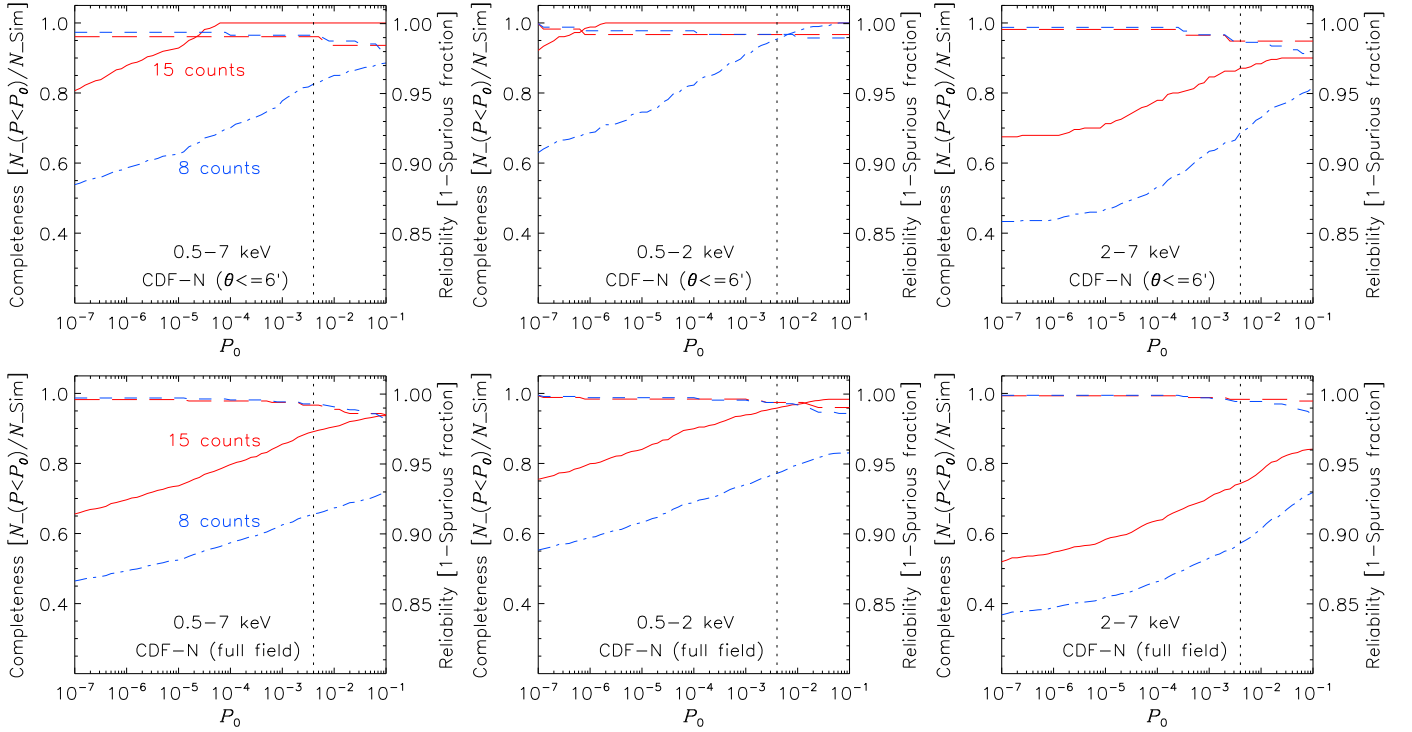
Figure 24. (Top) the $\theta \leqslant 6'$ case in the 2 Ms CDF-N: completeness (solid and dashed–dotted curves; left y-axis) and reliability (long dashed and short dashed curves; right y-axis) as a function of P_0 ($P < P_0$ as the source-detection criterion) for the simulations in the full, soft, and hard bands, for sources with $\geqslant 15$ counts (red solid and long dashed curves) and $\geqslant 8$ counts (blue dash–dotted and short dashed curves), respectively. The vertical dotted lines denote our adopted main-catalog source-detection threshold of $P_0 = 0.004$. (Bottom) same as top panels, but for the case of the full CDF-N field.
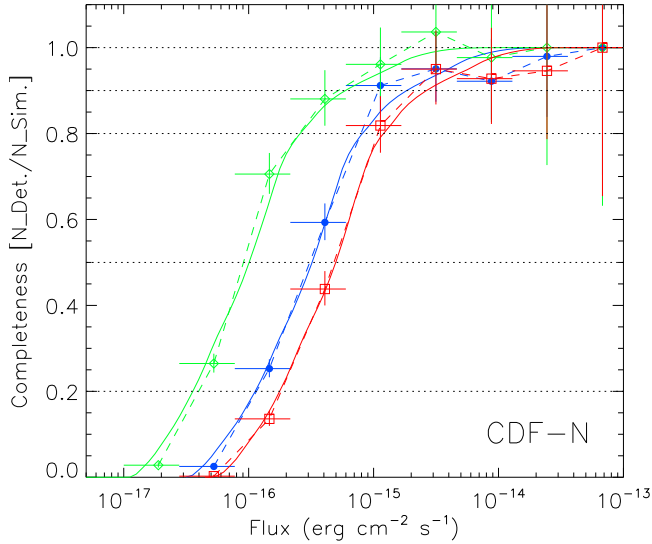
Figure 25. Completeness as a function of flux given the 2 Ms CDF-N main-catalog $P < 0.004$ criterion for the simulations in the full (blue filled circles), soft (green open diamonds), and hard (red open squares) bands, overlaid with the corresponding sky coverage curves (solid curves) that are normalized to the maximum sky coverage (see Figure 29). The dashed lines make connections between the corresponding adjacent cross points. The horizontal dotted lines denote five completeness levels.

Table 7
2 Ms CDF-N Flux Limit and Completeness

Completeness (%)	$f_{0.5-7\,keV}$ (erg cm^{-2} s^{-1})	$f_{0.5-2\,keV}$ (erg cm^{-2} s^{-1})	$f_{2-7\,keV}$ (erg cm^{-2} s^{-1})
90	1.9×10^{-15}	6.0×10^{-16}	2.7×10^{-15}
80	8.1×10^{-16}	2.6×10^{-16}	1.2×10^{-15}
50	3.2×10^{-16}	1.0×10^{-16}	5.0×10^{-16}
20	1.1×10^{-16}	3.6×10^{-17}	1.8×10^{-16}

3. PRODUCTION OF THE IMPROVED 250 KS E-CDF-S POINT-SOURCE CATALOGS

The overall production procedure is similar to that used for the 2 Ms CDF-N cataloging (see Figure 1) detailed in Section 2 and to that described in X11. To avoid unnecessary repetition, here we provide the salient details when appropriate and refer readers to Section 2 for essential details and X11 for full details. In addition, we make our 250 ks E-CDF-S data products publicly available (see footnote 13).

3.1. Observations and Data Reduction

E-CDF-S is composed of four distinct and contiguous $\approx$250 ks *Chandra* pointings (hereafter Fields 1, 2, 3, and 4) that flank CDF-S proper, consisting of a total of nine separate observations taken between 2004 February 29 and November 20 (see Table 1 of L05 for the journal of these 9 E-CDF-S observations). The 9 E-CDF-S observations made use of ACIS, with the four ACIS-I CCDs being in operation throughout the 9 E-CDF-S observations and the ACIS-S CCD S2 being operated for observations 5019–5022 and 6164. We do not use the data taken with the ACIS-S CCD S2 due to its large off-axis angle

5.9×10^{-17} erg cm^{-2} s^{-1} for the full, soft, and hard bands, respectively, which represent a factor of $\approx$2 improvement over those of A03, due to the facts that we adopt a sensitive two-stage source-detection procedure and that A03 adopted a different methodology for sensitivity calculations.

Table 8
2 Ms CDF-N: Background Parameters

Band (keV)	Mean Background (count pixel^{-1})[a]	Mean Background (count Ms^{-1} pixel^{-1})[b]	Total Background[c] (10^5 counts)	Count Ratio[d] (Background/Source)
Full (0.5–7.0)	0.171	0.167	11.4	5.3
Soft (0.5–2.0)	0.057	0.055	3.8	2.7
Hard (2–7)	0.115	0.108	7.6	10.2

Notes.
[a] The mean numbers of background counts per pixel.
[b] The mean numbers of background counts per pixel divided by the mean effective exposures.
[c] The total numbers of background counts in the background maps.
[d] Ratio between the total number of background counts and the total number of detected source counts in the main catalog.
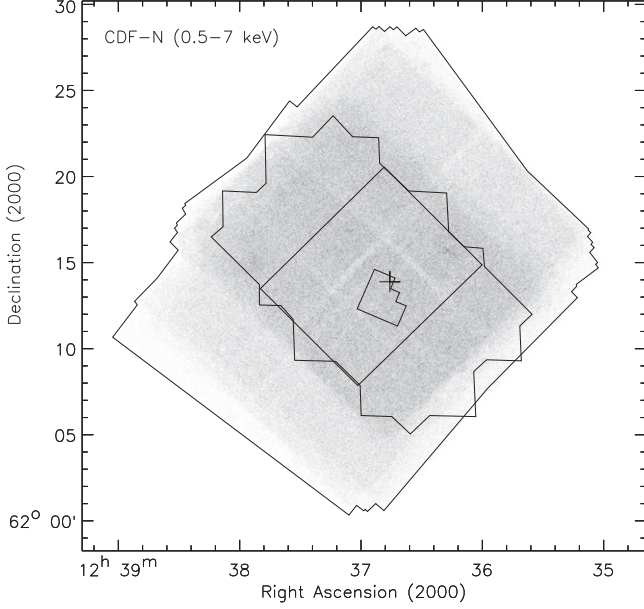
Figure 26. Full-band (0.5–7.0 keV) background map of the 2 Ms CDF-N rendered using linear grayscales. The higher background around the GOODS-N area is due to the larger effective exposure. The regions and the plus sign have the same meanings as those in Figure 2.
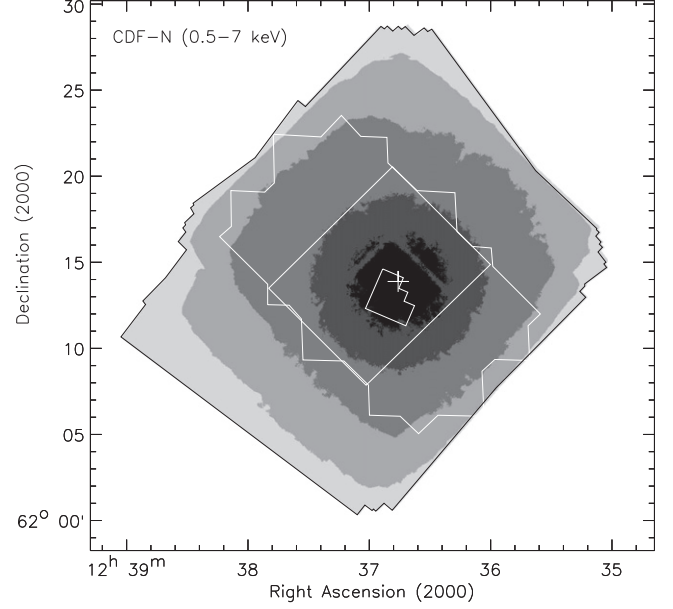
Figure 28. Full-band (0.5–7.0 keV) sensitivity map for the 2 Ms CDF-N main catalog. The grayscale levels, ranging from black to light gray, denote areas with flux limits of $<5.0 \times 10^{-17}$, 5.0×10^{-17} to 10^{-16}, 10^{-16} to 3.3×10^{-16}, 3.3×10^{-16} to 10^{-15}, and $>10^{-15}$ erg cm^{-2} s^{-1}, respectively. The regions and the plus sign have the same meanings as those in Figure 2.
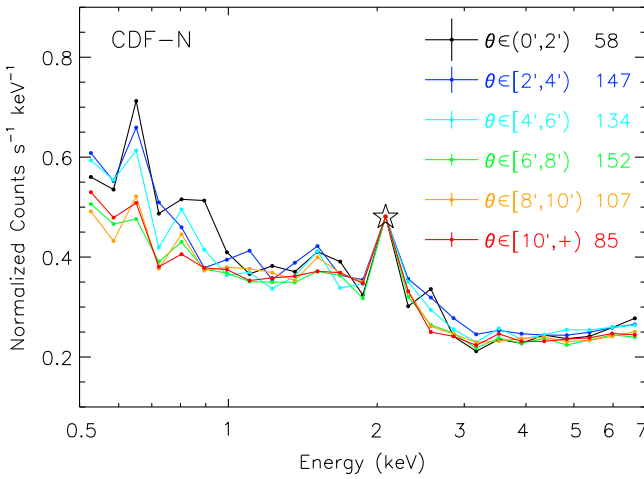
Figure 27. Mean background spectra for the 2 Ms CDF-N main-catalog sources calculated in various bins of off-axis angle. The spectra are normalized to have the same value at an energy slightly above 2 keV, which is indicated by a large five-pointed star. For clarity, errors on individual spectral data points are not plotted; the typical spectral error value and number of sources in each bin of off-axis angle are annotated in the top-right corner.
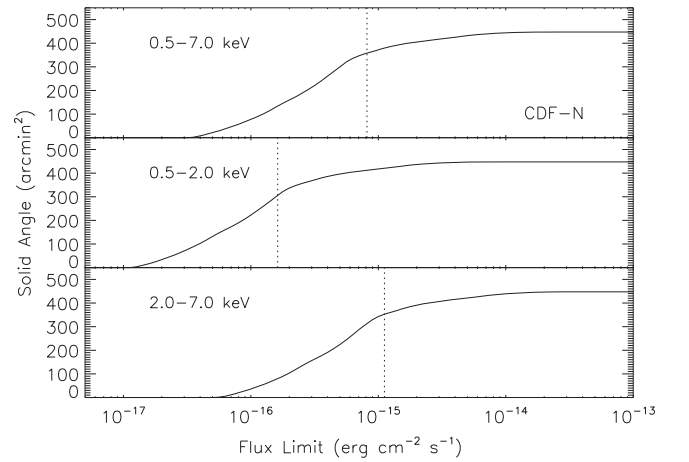
Figure 29. Survey solid angle as a function of flux limit in the full, soft, and hard bands for the 2 Ms CDF-N main catalog. The vertical dotted lines indicate the median fluxes of the main-catalog sources detected in the three bands.

and consequently its low sensitivity. For all 9 E-CDF-S observations, the focal-plane temperature was $-120°C$ and Very Faint mode was adopted.

The background light curves for all the 9 E-CDF-S observations were examined utilizing ChIPS. During observation 5015, there are two significant flares in the background, with each lasting ≈ 1.0 ks and being $\gtrsim 1.5$ times higher than nominal. The background increased to $\gtrsim 1.5$ times the nominal rate and remained above this level toward the end of observation 5017, affecting an exposure of ≈ 10.0 ks. All the other observations are free from strong flaring and are stable within $\approx 20\%$ of typical quiescent *Chandra* values, except for a number of short moderate "spikes" (up to ≈ 1.5 times higher than nominal). To remove these significant flares and moderate spikes, we utilize LC_SIGMA_CLIP with 3.5σ clippings adopted for all the 9 E-CDF-S observations. We then follow Section 2.1.2 for subsequent data reduction.

The entire 250 ks E-CDF-S covers a total region of 1128.6 arcmin^2, slightly smaller than four times the ACIS-I field of view due to the overlapping of observation field edges. The aim points are $(\alpha_{J2000.0} = 03^h33^m05^s.6, \delta_{J2000.0} = -27°41'08''.8)$, $(\alpha_{J2000.0} = 03^h31^m51^s.4, \delta_{J2000.0} = -27°41'38''.8)$, $(\alpha_{J2000.0} = 03^h31^m49^s.9, \delta_{J2000.0} = -27°57'14''.6)$, and $(\alpha_{J2000.0} = 03^h33^m02^s.9, \delta_{J2000.0} = -27°57'16''.1)$ for Fields 1–4, respectively.

3.2. Images, Exposure Maps, and Candidate-list Catalog

We follow Section 2.2.1 to construct the raw images and effective-exposure maps for the three standard bands as well as the exposure-weighted smoothed images in the 0.5–2, 2–4, and 4–7 keV bands that are subsequently combined into a false-color composite. When registering the individual observations to a common astrometric frame, we match X-ray centroid positions to the $K_s \leqslant 21.0$ mag sources in the TENIS WIRCam K_s-band catalog (Hsieh et al. 2012) rather than the VLA 1.4 GHz E-CDF-S radio sources (Miller et al. 2013) that were adopted in X11, because we find the astrometric frame of the K_s-band catalog to be in better agreement with that of other multiwavelength catalogs that are used for our X-ray source identifications in Section 3.3.3.

Figures 30 and 31 present the full-band raw image and effective-exposure map, respectively. Figure 32 displays the survey solid angle as a function of the minimum full-band effective exposure, and Figure 33 presents a false-color composite of the 250 ks E-CDF-S.

Following the blind-source search in Section 2.2.2, we use WAVDETECT (with the key parameters set to sigthresh $= 10^{-5}$, energy $= 1.497$ keV, ECF $= 0.393$, and minimum PSF map size, respectively) to detect sources in the combined raw images in the three standard bands, utilize the AE-computed centroid and matched-filter positions to improve the WAVDETECT source positions, and make use of AE to perform reliable X-ray photometry extractions. Our candidate-list catalog consists of 1434 E-CDF-S source candidates, with each being detected in at least one of the three standard bands.

3.3. Main Chandra Source Catalog

#### 3.3.1. Selection of Main-catalog Sources

To discard spurious candidate-list catalog sources, we include a candidate source into the main catalog only if it has $P < 0.002$ in at least one of the three standard bands. The
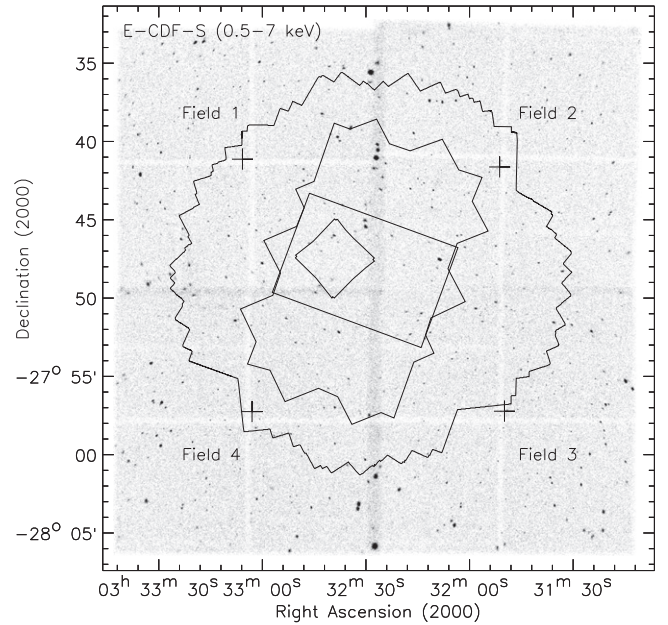

Figure 30. Full-band (0.5–7.0 keV) raw image of the 250 ks E-CDF-S rendered using linear grayscales. The E-CDF-S consists of four *Chandra* observational fields (Fields 1–4) that flank the CDF-S proper (1 Ms CDF-S, Giacconi et al. 2002; 2 Ms CDF-S, Luo et al. 2008; 4 Ms CDF-S, X11) indicated by the outermost segmented boundary; note the increase in background where these fields overlap. The aim points of the four fields are indicated as plus signs within the fields. The large polygon, the rectangle, and the small polygon indicate the regions for the GOODS-S (Giavalisco et al. 2004), the CANDELS GOODS-S deep (Grogin et al. 2011; Koekemoer 2011), and the HUDF (Beckwith et al. 2006), respectively. The light grooves running through the image are caused by the ACIS-I CCD gaps, thereby having lower effective exposures than the nearby non-gap areas (clearly revealed in Figure 31).
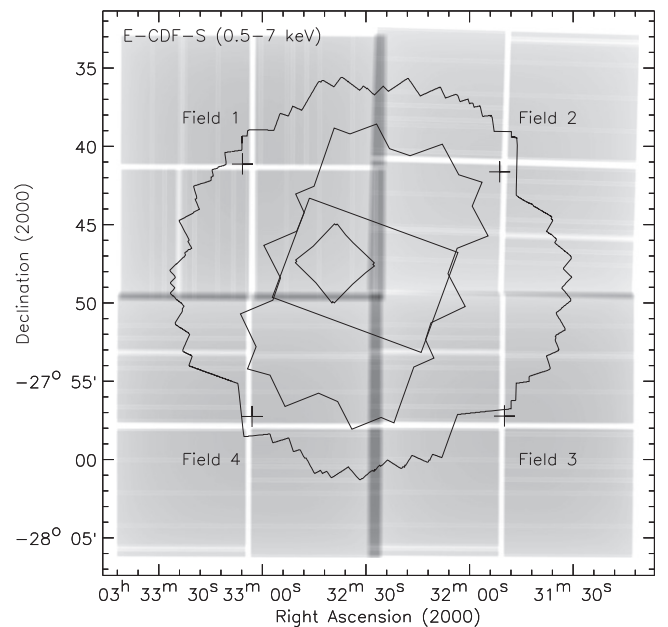
Figure 31. Full-band (0.5–7.0 keV) effective-exposure map of the 250 ks E-CDF-S rendered using linear grayscales. The darkest areas indicate the highest effective exposure times; the high effective exposures between fields are due to the overlap of observations. The ACIS-I CCD gaps can be clearly identified as the white grooves. The regions and the plus signs have the same meanings as those in Figure 30.
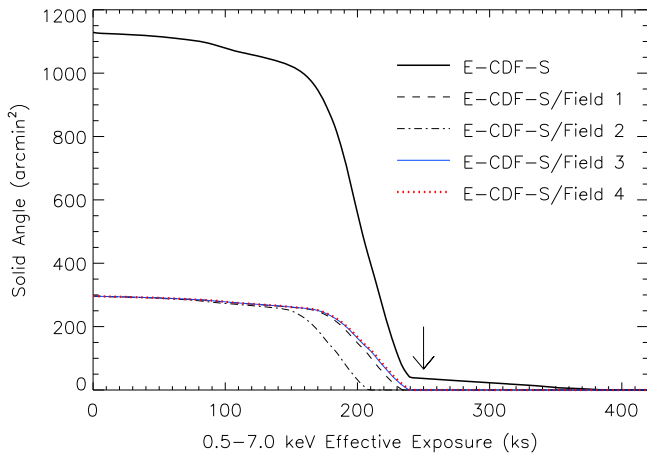
Figure 32. Survey solid angle as a function of minimum full-band (0.5–7.0 keV) effective exposure for the entire 250 ks E-CDF-S (thick solid curve) and the four observational fields (dashed, dash–dotted, solid, and dotted curves). Note that the dash–dotted curve for Field 2 appears different from the curves for the other fields, due to the fact that the nominal summed exposure of Field 2 is ≈13–19 ks shorter than that of the other fields. The entire E-CDF-S covers a total area of 1128.6 arcmin^2, roughly four times the ACIS-I field of view (16′.9 × 16′.9). The "tail" with exposures >250 ks (i.e., the portion of the thick solid curve on the right of the downward arrow signifying the 250 ks exposure) corresponds to regions where observational fields overlap (see Figure 31).
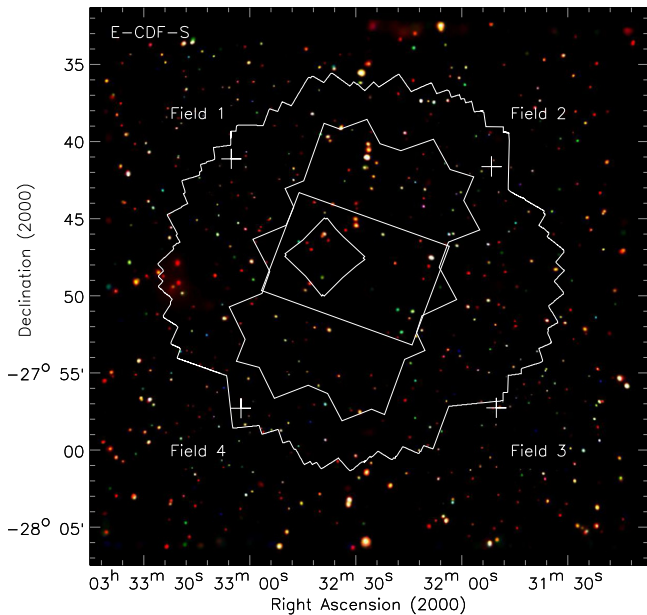
Figure 33. False-color image of the 250 ks E-CDF-S that is a color composite of the exposure-weighted and adaptively smoothed images in the 0.5–2.0 keV (red), 2–4 keV (green), and 4–7 keV (blue) bands. Near the aim points of the four observational fields, the seemingly smaller sizes and lower brightnesses of sources are due to the smaller PSF size on-axis. The regions and the plus signs have the same meanings as those in Figure 30.

choice of the $P < 0.002$ criterion results from a balance between keeping the fraction of spurious sources small and recovering the maximum possible number of real sources, primarily based on joint maximization of the total number of sources and minimization of the fraction of sources without significant multiwavelength counterparts (see Section 3.3.3). Our main catalog consists of a total of 1003 sources given this $P < 0.002$ criterion. Figure 34 presents the fraction of candidate-list sources that satisfy the $P < 0.002$ main-catalog

source-selection criterion and the $1 - P$ distribution of candidate-list sources as a function of the minimum WAVDETECT probability (see footnote 20).

3.3.2. X-Ray Source Positional Uncertainty

We find 257 matches between the 1003 main-catalog sources and the $K_s \leqslant 20.0$ mag sources in the TENIS WIRCam K_s-band catalog using a matching radius of 1″.5. We estimate on average ≈6.5 (2.3%) false matches and a median offset of 1″.07 for these false matches. Figure 35(a) presents the positional offset between these 257 X-ray-K_s-band matches (the median offset is 0″.38) as a function of off-axis angle. The source indicated as a red filled circle at the top-left corner is a mismatch (its real counterpart is a nearby fainter source that is resolved in the *HST* image but not resolved in the K_s-band image) and is therefore not included in the following analysis of X-ray positional uncertainty. Figure 35(b) presents the positional residuals between the X-ray and K_s-band positions for the remaining 256 sources, which appear roughly symmetric. We find that the empirical formula of the 68% confidence-level X-ray positional uncertainty with off-axis angle and source-count dependencies that is derived for the 2 Ms CDF-N main-catalog sources (i.e., Equation (2) in Section 2.3.2) is fully applicable to the 256 250 ks E-CDF-S main-catalog sources. Figure 36 shows the distributions of X-ray-K_s-band positional offsets in four bins of X-ray positional uncertainty. For the analysis here, as in Section 2.3.2, we allow for positional uncertainties arising from the K_s-band sources that are typically $\lesssim 0″.1$.

3.3.3. Multiwavelength Identifications

We implement the likelihood-ratio matching procedure to identify the primary ONIR counterparts for the main-catalog X-ray sources. We adopt, in order of priority, nine ONIR catalogs for identification purposes.

1. The VLA 1.4 GHz E-CDF-S radio catalog (denoted as "VLA"; Miller et al. 2013), with a 5σ limiting flux density of ≈20 μJy.
2. The GOODS-S *HST* version 2.0 z-band catalog (denoted as "GOODS-S"; Giavalisco et al. 2004), with a 5σ limiting magnitude of 28.2.
3. The GEMS *HST* z-band catalog (denoted as "GEMS"; Caldwell et al. 2008), with a 5σ limiting magnitude of 27.3.
4. The CANDELS GOODS-S WFC3 *H*-band catalog (denoted as "CANDELS"; Grogin et al. 2011; Koekemoer 2011), with a 5σ limiting magnitude of 28.0.
5. The GOODS-S MUSIC catalog (denoted as "MUSIC"; Grazian et al. 2006; we adopt the *K*-selected sources in the V2 catalog presented in Santini et al. 2009) based on the Retzlaff et al. (2010) VLT/ISAAC data, with a limiting *K*-band magnitude of 23.8 at 90% completeness.
6. The TENIS WIRCam K_s-band catalog (denoted as "TENIS"; Hsieh et al. 2012), with a 5σ limiting magnitude of 25.0 in the inner 400 arcmin^2 region.
7. The ESO 2.2 m WFI *R*-band catalog (denoted as "WFI"; Giavalisco et al. 2004), with a 5σ limiting magnitude of 27.3.
8. The MUSYC *K*-band catalog (denoted as "MUSYC"; Taylor et al. 2009), with a 5σ limiting magnitude of 22.4.
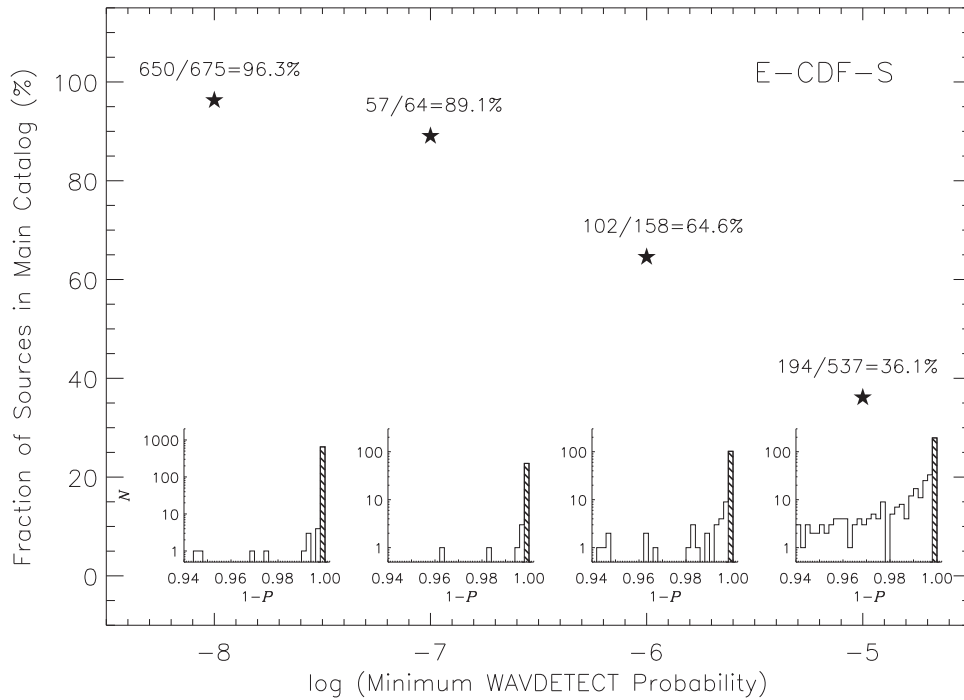
Figure 34. Fraction of the candidate-list catalog sources having an AE binomial no-source probability $P < 0.002$ that are included in the 250 ks E-CDF-S main catalog, as a function of minimum WAVDETECT probability (see footnote 20; denoted as five-pointed stars). The number of sources having $P < 0.002$ vs. the number of candidate-list catalog sources detected at each minimum WAVDETECT probability is displayed (note that there are $650 + 57 + 102 + 194 = 1003$ main-catalog sources and $675 + 64 + 158 + 537 = 1434$ candidate-list catalog sources). The fraction of candidate-list catalog sources included in the main catalog falls from 96.3% to 36.1% between minimum WAVDETECT probabilities of 10^{-8} and 10^{-5}. The insets present the $1 - P$ distributions for the candidate-list catalog sources at each minimum WAVDETECT probability, and the shaded areas highlight those included in the main catalog (i.e., satisfying $1 - P > 0.998$).

9. The SIMPLE IRAC 3.6 μm catalog (denoted as "SIM-PLE"; Damen et al. 2011),with a 5σ limiting magnitude of 23.8.

We shift the above ONIR source positions appropriately to be consistent with the TENIS WIRCam K_s-band astrometry (see Section 3.2). We identify primary ONIR counterparts for 958 (95.5%) of the 1003 main-catalog sources. Utilizing the Monte Carlo approach mentioned in Section 2.3.3, we estimate the false-match rates for the above nine catalogs in the listed order to be 0.2%, 4.4%, 4.6%, 3.4%, 2.9%, 2.4%, 5.6%, 2.1%, and 2.6%, respectively, with a weighted mean false match rate of 3.3%.

We visually examine the X-ray images of the 45 main-catalog sources without highly significant multiwavelength counterparts, and find that the majority of them have apparent or even strong X-ray signatures. Of these 45 sources, three are located near a very bright star (their counterparts might thus be hidden by the light of the bright stars), with one having 40.7 full-band counts and having no associations with any back-ground flares or cosmic-ray afterglows; one has a large off-axis angle of 8.′4 and 12.5 full-band counts; two have full-band counts of 14.7 and 16.6, respectively; and all the other 39 sources have <10 full-band counts (some of them are thus likely false detections). Only 4 out of these 45 sources are also present in the L05 main catalog.

3.3.4. Main-catalog Details

Our main catalog consists of a total of 97 columns, the vast majority of which are similar to the columns presented in the 2 Ms CDF-N main catalog (see Table 2 in Section 2.3.4), with some additional distinct columns including z_{spec} quality flag,

corresponding L05 and X11 source information, and observation field. We present the main catalog itself in Table 9. Below we give the details of these 97 columns.
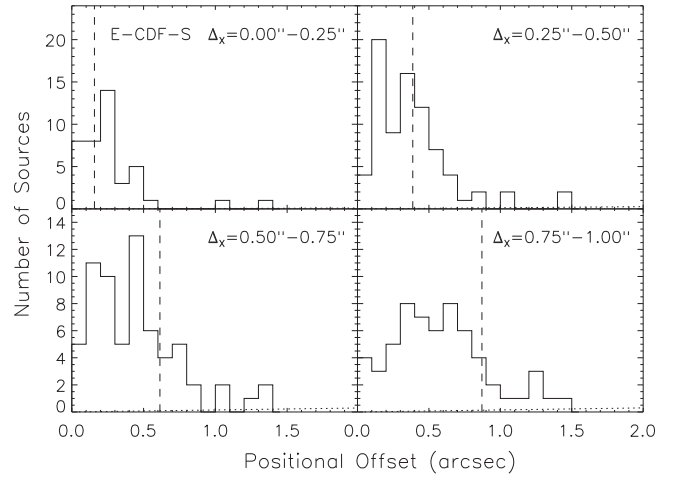
1. Column 1 gives the source sequence number (i.e., XID) in this work. Sources are sorted in order of increasing R.A.
2. Columns 2 and 3 give the J2000.0 R.A. and decl. of the X-ray source, respectively.
3. Columns 4 and 5 give the minimum value of $\log P$ among the three standard bands, and the logarithm of the minimum WAVDETECT false-positive probability detection threshold, respectively. For sources with $P = 0$, we set $\log P = -99.0$. We find a median value of $\log P = -10.4$ for the main-catalog sources, which is much smaller than the main-catalog selection threshold value of $\log P < -2.7$ (i.e., $P < 0.002$; see Section 3.3.1). We find that 650, 57, 102, and 194 sources have minimum WAVDETECT probabilities (see footnote 20) of 10^{-8}, 10^{-7}, 10^{-6}, and 10^{-5}, respectively (see Figure 34).
4. Column 6 gives the X-ray positional uncertainty in units of arcseconds at the $\approx 68\%$ confidence level, which is computed utilizing Equation (2). For the main-catalog sources, the positional uncertainty ranges from 0.″10 to 1.″30, with a median value of 0.″63.
5. Column 7 gives the off-axis angle of each X-ray source, in units of arcminutes, that is the angular separation between the X-ray source and the aim point of the corresponding field (given in Section 3.1). For the main-
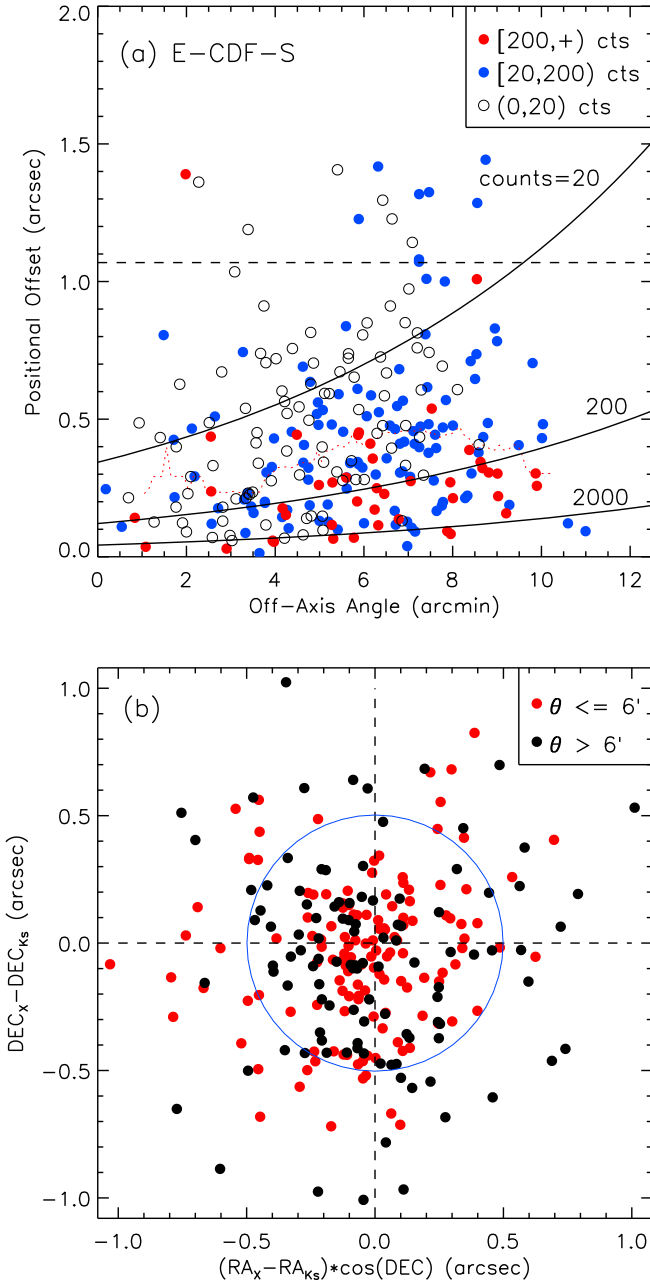
Figure 35. (a) Positional offset vs. off-axis angle for the 257 250 ks E-CDF-S main-catalog sources that have $K_s \leqslant 20.0$ mag counterparts in the TENIS WIRCam K_s-band catalog (Hsieh et al. 2012) utilizing a matching radius of 1″5 (see Section 3.3.2 for the description of an apparent outlier, i.e., the red filled circle located at the top left corner, that deviates significantly from the relation defined as Equation (2)). Red filled, blue filled, and black open circles indicate X-ray sources with $\geqslant 200$, $\geqslant 20$, and < 20 counts in the energy band that is used to determine the source position, respectively. The red dotted curve denotes the running median of positional offset in bins of 2′. The horizontal dashed line represents the median offset (1″07) of the false matches expected. The three solid curves correspond to the ≈68% confidence-level X-ray positional uncertainties (derived according to Equation (2)) for sources with 20, 200, and 2000 counts. (b) Positional residuals between the X-ray and K_s-band positions for the remaining 256 X-ray-K_s-band matches. Red and black filled circles represent sources with an off-axis angle of ⩽6′ and >6′, respectively. A blue circle with a 0″5 radius is drawn at the center as a visual guide.

Figure 36. Histograms of X-ray-K_s-band positional offsets for the 256 250 ks E-CDF-S main-catalog sources that are matched to the TENIS WIRCam $K_s \leqslant 20.0$ mag sources (Hsieh et al. 2012) utilizing a matching radius of 1″5 (note that one source is excluded; see Figure 35(a) and Section 3.3.2). Based on their X-ray positional uncertainties estimated with Equation (2), these matched sources are divided into four bins of 0″–0″25, 0″25–0″50, 0″50–0″75, and 0″75–1″. In each panel (bin), the vertical dashed line denotes the median X-ray positional uncertainty; the dotted line (almost indistinguishable from the bottom x-axis) displays the expected numbers of false matches assuming a uniform spatial distribution of K_s-band sources as a function of X-ray-K_s-band positional offset.

1σ upper and lower statistical errors for the three standard bands, respectively. We treat a source as being "detected" for photometry purposes in a given band only if it satisfies $P < 0.002$ in that band. We calculate upper limits for sources not detected in a given band, and set the associated errors to -1.00.

7. Column 17 gives a flag indicating whether a source shows a radial profile consistent with that of the local PSF. Of the 1003 main-catalog sources, we find that all but 60 have radial profiles consistent with that of their corresponding PSFs above a 95% confidence level, and set the value of this column to 1; the 60 sources have the value of this column set to 0. These 60 sources are located across the entire E-CDF-S field and show no pattern of spatial clustering. Moreover, we visually inspect these 60 sources and do not find any significant signature of extension.

8. Columns 18 and 19 give the R.A. and decl. of the primary ONIR counterpart (shifted accordingly to be consistent with the TENIS WIRCam K_s-band astrometric frame; see Section 3.3.3). Sources without ONIR counterparts have these two columns set to "00 00 00.00" and "−00 00 00.0."

9. Column 20 gives the offset between the X-ray source and the primary ONIR counterpart in units of arcseconds. Sources without ONIR counterparts have this column set to -1.00.

10. Column 21 gives the AB magnitude (see footnote 21) of the primary ONIR counterpart in the counterpart-detection band. Sources without ONIR counterparts have this column set to -1.00.

11. Column 22 gives the name of the ONIR catalog (i.e., VLA, GOODS-S, GEMS, CANDELS, MUSIC, TENIS, WFI, MUSYC, or SIMPLE; see Section 3.3.3) where the

catalog sources, the off-axis angle ranges from 0′18 to 12′22, with a median value of 5′47.

6. Columns 8–16 give the aperture-corrected net (i.e., background-subtracted) source counts and the associated

Table 9
250 ks E-CDF-S Main *Chandra* Source Catalog

No. (1)	α_{2000} (2)	δ_{2000} (3)	$\log P$ (4)	WAVDETECT (5)	Pos Err (6)	Off-axis (7)	Full Band (8)	Full Band Upp Err (9)	Full Band Low Err (10)	Soft Band (11)	Soft Band Upp Err (12)	Soft Band Low Err (13)
1	03 31 11.32	−27 33 36.9	−10.1	−8	1.0	11.97	46.8	10.5	9.3	32.2	8.1	6.9
2	03 31 12.63	−27 57 18.3	−4.0	−5	1.0	8.24	15.7	6.9	5.6	9.9	−1.0	−1.0
3	03 31 12.99	−27 55 48.8	−99.0	−8	0.3	8.28	333.4	21.2	20.0	157.1	14.6	13.4
4	03 31 13.06	−27 32 51.9	−11.6	−5	0.9	12.22	58.0	12.0	10.8	36.4	8.6	7.3
5	03 31 13.64	−27 49 49.0	−3.5	−5	1.0	10.93	29.6	11.0	9.8	17.6	−1.0	−1.0

Note. The full table contains 97 columns of information for the 1003 X-ray sources.

(This table is available in its entirety in machine-readable form.)

primary counterpart is found. Sources without ONIR counterparts have a value set to "....".

12. Columns 23–49 give the counterpart R.A., decl., and AB magnitude (see footnote 21) from the above nine ONIR catalogs that are used for identifications (the coordinates have been shifted accordingly to be consistent with the TENIS WIRCam K_s-band astrometric frame; see Section 3.3.3). We match the position of the primary ONIR counterpart with the nine ONIR catalogs using a matching radius of 0.″5. We set values of R.A. and decl. to "00 00 00.00" and "−00 00 00.0" and set AB magnitudes to −1.00 for sources without matches. We find 16.9%, 13.3%, 57.3%, 9.0%, 9.3%, 79.5%, 72.3%, 59.4%, and 75.1% of the main-catalog sources have VLA, GOODS-S, GEMS, CANDELS, MUSIC, TENIS, WFI, MUSYC, and SIMPLE counterparts, respectively.

13. Columns 50–52 give the z_{spec}, z_{spec} quality flag, and z_{spec} reference. z_{spec}'s are collected from (1) Szokoly et al. (2004), (2) Zheng et al. (2004), (3) Ravikumar et al. (2007), (4) Treister et al. (2009), (5) Balestra et al. (2010), (6) Silverman et al. (2010), (7) Bonzini et al. (2012), (8) Cooper et al. (2012), (9) Coppin et al. (2012), (10) Georgantopoulos et al. (2013), (11) Le Fèvre et al. (2013), (12) Taylor et al. (2009), (13) Kriek et al. (2008), (14) Hsu et al. (2014), (15) Skelton et al. (2014), (16) Luo et al. (2010), and (17) Cardamone et al. (2010). We match the positions of primary ONIR counterparts with the above z_{spec} catalogs utilizing a 0.″5 matching radius. For the 958 main-catalog sources with ONIR counterparts, we find that 476 (49.7%) have z_{spec} measurements (384/476 = 80.7% have $R \leqslant 24$ mag and 92/476 = 19.3% have $R > 24$ mag). 394 (82.8%) of these 476 z_{spec}'s are secure, being flagged as "Secure" in Column 51; 82 (17.2%) of these 476 z_{spec}'s are insecure, being flagged as "Insecure" in Column 51. Sources without z_{spec} have these three columns set to −1.000, "None," and −1, respectively. The z_{spec} histogram is shown in Figure 37(a).

14. Columns 53–75 give the z_{phot} information compiled from the literature. Columns 53–56 give the z_{phot}, the associated 1σ lower and upper bounds, and the alternative z_{phot} (set to −1.000 if not available) from the CANDELS/GOODS-S, CDF-S, and E-CDF-S z_{phot} catalog of Hsu et al. (2014). Columns 57–61 give the z_{phot}, the associated 1σ lower and upper bounds, Q_z, and the likely photometric classification ("Galaxy" or "Star") from the CANDELS/3D-HST z_{phot} catalog of Skelton et al. (2014). Columns 62–65 give the z_{phot}, the associated 1σ lower and upper bounds, and the alternative z_{phot} (set to −1.000 if not available) from Luo et al. (2010). Columns 66–71 give the z_{phot}, the associated 1σ lower and upper bounds, Q_z, the stellarity index (ranging from 0 to 1; a value of −1.00 indicating information not available), and the flag of whether the source prefers the photometric fitting result using the stellar templates (the values of 1, 0, and −1 indicating preferring the stellar templates, not preferring the stellar templates, and information not available, respectively) from Cardamone et al. (2010). Columns 72–75 give the z_{phot}, the associated 1σ lower and upper bounds, and the likely photometric classification ("Hybrid," "Galaxy," or "Star," with the former indicating preferring a mixture of AGN and galaxy

templates) from Rafferty et al. (2011). We match the positions of primary ONIR counterparts with the above z_{phot} catalogs utilizing a 0.″5 matching radius. Of the 958 main-catalog sources with ONIR counterparts, 748 (78.1%), 136 (14.2%), 221 (23.1%), 624 (65.1%), and 692 (72.2%) have z_{phot} estimates from Hsu et al. (2014), Skelton et al. (2014), Luo et al. (2010), Cardamone et al. (2010), and Rafferty et al. (2011), respectively. Sources without z_{phot}'s have all these columns set to −1.000 or "..." correspondingly. Figures 37((b)–(g)) present the histograms of $(z_{phot} - z_{spec})/(1 + z_{spec})$ and z_{phot} for these five z_{phot} catalogs; we caution that the quoted z_{phot} qualities, as indicated by values of σ_{NMAD} annotated in Figures 37((b)–(f)), do not necessarily represent realistic estimates because those z_{phot} qualities are not derived using blind tests and in some cases "training biases" are involved in z_{phot} derivation.

15. Column 76 gives the z_{final} adopted in this work. We choose z_{final} for a source in the following order of preference: (1) secure z_{spec}'s; (2) insecure z_{spec}'s that are in agreement with any z_{phot} estimate available [i.e., $|(z_{spec} - z_{phot})/(1 + z_{spec})| \leqslant 0.15$]; (3) z_{phot}'s from Hsu et al. (2014); (4) z_{phot}'s from Skelton et al. (2014); (5) z_{phot}'s from Luo et al. (2010); (6) z_{phot}'s from Cardamone et al. (2010); (7) z_{phot}'s from Rafferty et al. (2011); and (8) insecure z_{spec}'s that are the only redshift information available (thus being unable to compare with any z_{phot}). Of the 958 main-catalog sources with ONIR counterparts, 810 (84.6%) have z_{spec}'s or z_{phot}'s.

16. Column 77 gives the corresponding source ID number in the L05 E-CDF-S catalogs. We match our X-ray source positions to the L05 source positions (shifted accordingly to be consistent with the TENIS WIRCam K_s-band astrometric frame) using a 2.″5 matching radius for sources having $\theta < 6'$ and a 4.″0 matching radius for sources having $\theta \geqslant 6'$. Among the 1003 main-catalog sources, we find that (1) 728 have matches in the 762-source L05 main catalog (the value of this column is that from Column 1 of Table 2 in L05), i.e., there are 275 (i.e., 1003−728 = 275) new main-catalog sources (see Section 3.3.7 for more details of these 275 new sources), compared to the L05 main catalog; (2) 21 have matches in the 33-source L05 supplementary catalog (the value of this column is that from Column 1 of Table 6 in L05 added with a prefix of "SP_"); and (3) 254 have no match in either the L05 main or supplementary catalog, which are detected now thanks to our two-stage source-detection approach (the value of this column is set to −1). We refer readers to Section 3.3.5 for information on the 34 L05 main-catalog sources that are not included in our main catalog.

17. Columns 78 and 79 give the R.A. and decl. of the corresponding L05 source (shifted accordingly to be consistent with the TENIS WIRCam K_s-band astrometric frame). Sources without an L05 match have these two columns set to "00 00 00.00" and "−00 00 00.0."

18. Column 80 gives the corresponding source ID number in the X11 4 Ms CDF-S catalogs. For the 1003 main-catalog sources, we find that (1) 273 have matches in the 740-source X11 main catalog (the value of this column is that from Column 1 of Table 3 in X11), (2) 12 have matches in the 36-source X11 supplementary catalog (the value of
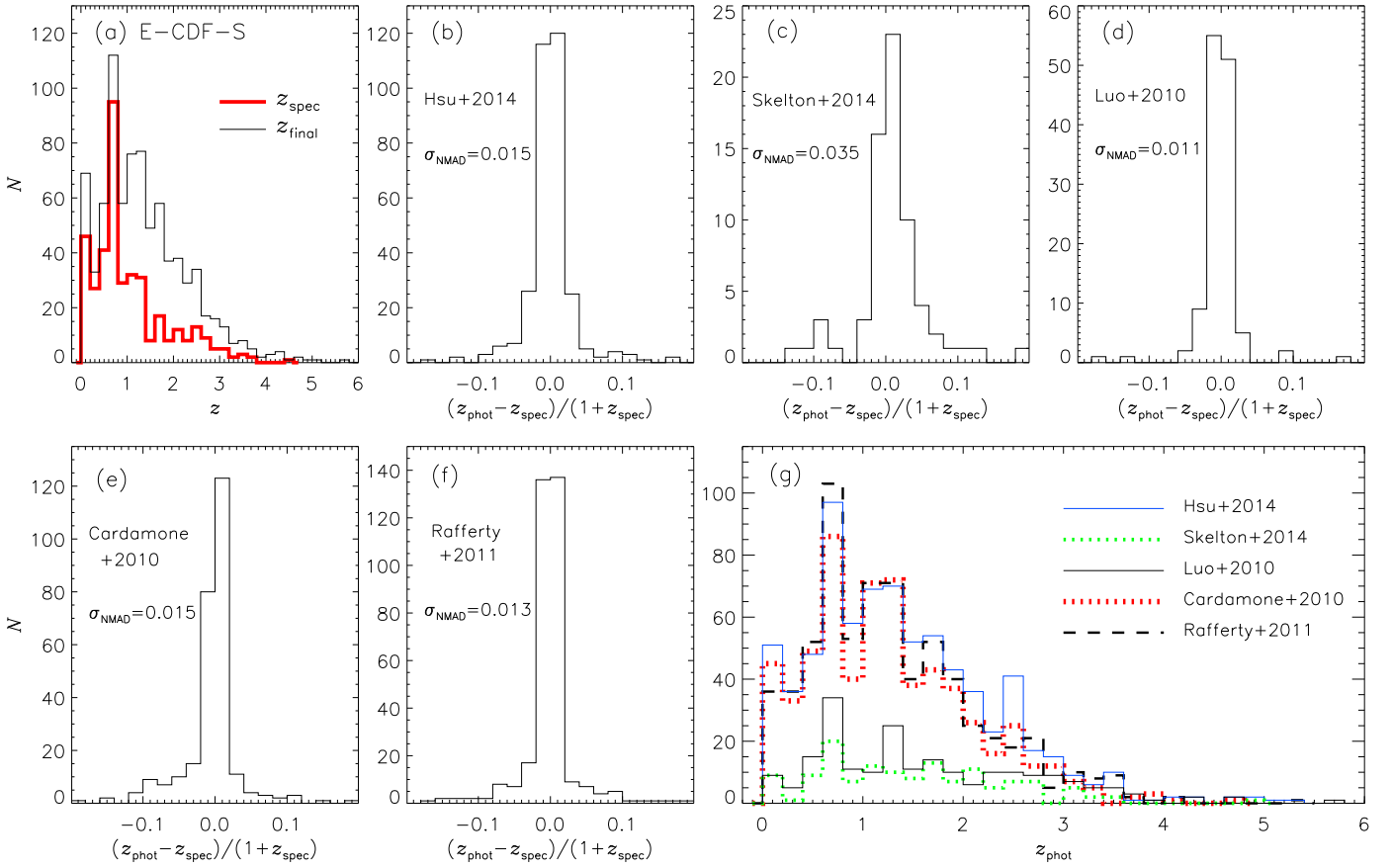
Figure 37. Redshift information for the 250 ks E-CDF-S main-catalog sources. (a) Histograms of $z_{\rm spec}$ (476 sources; $476/1003 = 47.5\%$) and $z_{\rm final}$ (810 sources; $810/1003 = 80.8\%$). (b) Histogram of $(z_{\rm phot} - z_{\rm spec})/(1 + z_{\rm spec})$ from Hsu et al. (2014; 424 sources) with $\sigma_{\rm NMAD}$ annotated. (c) Histogram of $(z_{\rm phot} - z_{\rm spec})/(1 + z_{\rm spec})$ from Skelton et al. (2014; 99 sources) with $\sigma_{\rm NMAD}$ annotated. (d) Histogram of $(z_{\rm phot} - z_{\rm spec})/(1 + z_{\rm spec})$ from Luo et al. (2010; 161 sources) with $\sigma_{\rm NMAD}$ annotated. (e) Histogram of $(z_{\rm phot} - z_{\rm spec})/(1 + z_{\rm spec})$ from Cardamone et al. (2010; 387 sources) with $\sigma_{\rm NMAD}$ annotated. (f) Histogram of $(z_{\rm phot} - z_{\rm spec})/(1 + z_{\rm spec})$ from Rafferty et al. (2011; 431 sources) with $\sigma_{\rm NMAD}$ annotated. (g) Histograms of $z_{\rm phot}$ from Hsu et al. (2014; 748 sources), Skelton et al. (2014; 136 sources), Luo et al. (2010; 221 sources), Cardamone et al. (2010; 624 sources), and Rafferty et al. (2011; 692 sources).

this column is that from Column 1 of Table 6 in X11 added with a prefix of "SP_"); and (3) 718 have no match in either the X11 main or supplementary catalog, mainly due to their spatial locations being covered by the 4 Ms CDF-S (the value of this column is set to −1).

19. Columns 81 and 82 give the R.A. and decl. of the corresponding X11 source (shifted accordingly to be consistent with the TENIS WIRCam K_s-band astrometric frame). Sources without an X11 match have these two columns set to "00 00 00.00" and "−00 00 00.0."

20. Columns 83–85 give the effective exposure times in units of seconds derived from the exposure maps for the three standard bands.

21. Columns 86–88 give the band ratio and the associated upper and lower errors, respectively. Upper limits are computed for sources detected in the soft band but not the hard band, while lower limits are computed for sources detected in the hard band but not the soft band; for these sources, the upper and lower errors are set to the calculated band ratio. Band ratios and associated errors are set to −1.00 for sources with full-band detections only.

22. Columns 89–91 give the effective photon index Γ and the associated upper and lower errors, respectively, assuming a power-law model with the Galactic column density that is given in Section 1. Upper limits are

computed for sources detected in the hard band but not the soft band, while lower limits are computed for sources detected in the soft band but not the hard band; for these sources, the upper and lower errors are set to the calculated Γ. A value of $\Gamma = 1.4$ is assumed for low-count sources (as defined in Section 2.3.4), and the associated upper and lower errors are set to 0.00.

23. Columns 92–94 give observed-frame fluxes in units of erg cm^{-2} s^{-1} for the three standard bands. Negative flux values denote upper limits.

24. Column 95 gives a basic estimate of the absorption-corrected, rest-frame 0.5–7 keV luminosity ($L_{0.5-7\,{\rm keV}}$ or L_X) in units of erg s^{-1}. Note that $L_{0.5-8\,{\rm keV}} = 1.066 \times L_{0.5-7\,{\rm keV}}$ and $L_{2-10\,{\rm keV}} = 0.721 \times L_{0.5-7\,{\rm keV}}$, given the assumed $\Gamma_{\rm int} = 1.8$ (see the description of Column 70 of the 2 Ms CDF-N main catalog in Section 2.3.4 for details). Sources without $z_{\rm final}$ have this column set to −1.000.

25. Column 96 gives a basic estimate of likely source type: "AGN," "Galaxy," or "Star." We use the same classification scheme detailed in Section 4.4 of X11 (see the description of Column 78 of the X11 main catalog), which makes use of additional spectroscopic and photometric data available in the CDF-S/E-CDF-S. There are 909 (90.6%), 67 (6.7%), and 27 (2.7%) of

Table 10
250 ks E-CDF-S Main Catalog: Summary of Source Detections

Band (keV)	Number of Sources	Maximum Counts	Minimum Counts	Median Counts	Mean Counts
Full (0.5–7.0)	929	4010.6	3.3	27.1	87.3
Soft (0.5–2.0)	769	2802.6	2.2	18.9	64.5
Hard (2–7)	655	1210.8	3.4	20.4	46.0

Table 11
250 ks E-CDF-S Main Catalog: Sources Detected in One Band but Not Another

Detection Band (keV)	Nondetection Full Band	Nondetection Soft Band	Nondetection Hard Band
Full (0.5–7.0)	…	210	298
Soft (0.5–2.0)	50	…	291
Hard (2–7)	24	177	…

the 1003 main-catalog sources identified as AGNs, galaxies, and stars, respectively.

26. Column 97 gives brief notes on the sources. Sources in close doubles or triples are annotated with "C" (a total of 29 such sources) and sources lying at the field edge are annotated with "E" (only one such source); otherwise, sources are annotated with "...".

3.3.5. Comparison with the L05 Main-catalog Sources

Table 10 summarizes the source detections in the three standard bands for the main catalog. Of the 1003 main-catalog sources, 929, 769, and 655 are detected in the full, soft, and hard bands, respectively; as a comparison, of the 762 L05 main-catalog sources, 689, 598, and 453 are detected in the full, soft, and hard bands, respectively (note that L05 adopt an upper energy bound of 8 keV). As stated in Section 3.3.4 (see the description of Column 77), 728 of the main-catalog sources have matches in the L05 main catalog. For these 728 common sources, we find that the X-ray photometry derived in this work is in general agreement with that in L05, e.g., the median ratio between our soft band count rates and those in L05 for the soft-band detected common sources is 1.04, with an interquartile range of 0.96–1.12. The significant increase in the number of main-catalog sources, i.e., an increase of $1003 - 728 = 275$ for new main-catalog sources, is mainly due to the improvements of our cataloging methodology that are summarized in Table 1, particularly our two-stage source-detection approach. Indeed, we are able to detect fainter sources than L05 that are yet reliable, with median detected counts (see Table 10) in the three standard bands being $\approx 70\%$ of those of L05 (see their Table 4).

Thirty-four (i.e., $762 - 728 = 34$) of the L05 main-catalog sources are not recovered in our main catalog, among which six are recovered in our supplementary catalog (see Section 3.4). Among the 28 L05 main-catalog sources that are not recovered in our main or supplementary catalogs, (1) 2 sources were the fainter sources in pairs in L05 but now fail our source-detection criterion of $P < 0.002$; (2) 1 source was in a triplet in L05 but is now removed based on visual inspection of the X-ray images compared to the local PSF size, thus degrading the previous triplet into a doublet; (3) four sources barely fail our source-detection criterion, with $0.002 < P < 0.004$; (4) 12 sources not only have faint X-ray signatures, but also have multiwavelength counterparts, thus being likely real X-ray sources, although they do not satisfy our $P < 0.002$ source-selection criterion; and (5) the remaining nine sources have marginal X-ray signatures and have no multiwavelength counterparts, thus they are likely false detections.

Table 11 summarizes the number of sources detected in one band but not another in the main catalog (cf. Table 5 of L05). There are 57, 50, and 24 sources detected only in the full, soft,
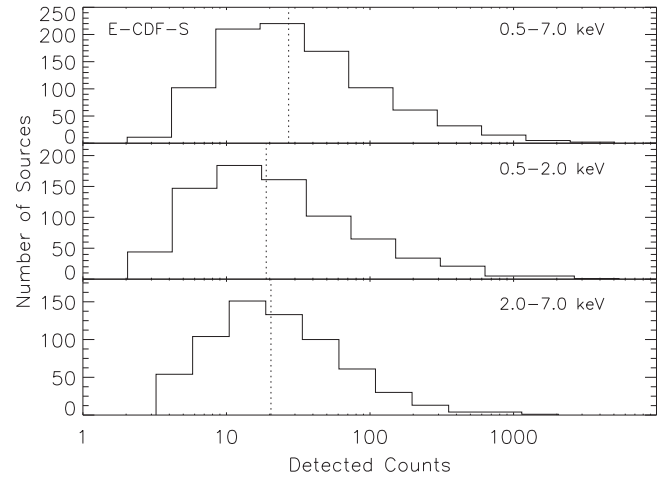
Figure 38. Distributions of detected source counts for the 250 ks E-CDF-S main-catalog sources in the full, soft, and hard bands. Sources with upper limits are not plotted. The vertical dotted lines indicate the median detected counts of 27.1, 18.9, and 20.4, for the full, soft, and hard bands, respectively (detailed in Table 10).

and hard bands, in contrast to 68, 58, and 15 sources in the L05 main catalog, respectively.

3.3.6. Properties of Main-catalog Sources

Figure 38 presents the histograms of detected source counts in the three standard bands for the sources in the main catalog. The median detected counts are 27.1, 18.9, and 20.4 for the full, soft, and hard bands, respectively; and there are 165, 77, 29, and 9 sources having >100, >200, >500, and >1000 full-band counts, respectively.

Figure 39 presents the histograms of effective exposure times in the three standard bands for all the 1003 main-catalog sources. The median effective exposures are 207.1, 206.0, and 210.6 ks for the full, soft, and hard bands, respectively.

Figure 40 presents the histograms of observed-frame X-ray fluxes in the three standard bands for the sources in the main catalog. The X-ray fluxes distribute over three orders of magnitude, with median values of 1.6×10^{-15}, 5.3×10^{-16}, and 2.0×10^{-15} erg cm^{-2} s^{-1} for the full, soft, and hard bands, respectively.

Figure 41 presents the histogram of the AE-computed binomial no-source probability P for the sources in the main catalog, with a total of 45 sources having no multiwavelength counterparts highlighted by shaded areas. The majority of the main-catalog sources have low P values that indicate significant detections, with a median P of 3.68×10^{-11} and an interquartile range of 1.28×10^{-32} to 2.04×10^{-5}. We find that 1.0% of the $\log P \leqslant -5$ sources have no ONIR counterparts, in contrast to 14.2% of $\log P > -5$ sources lacking ONIR counterparts. Given the small false-match rate estimated
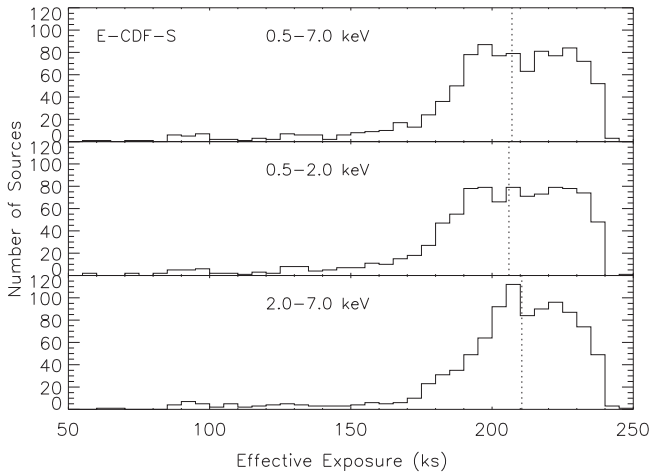
Figure 39. Distributions of effective exposure times for all the 1003 E-CDF-S main-catalog sources in the full, soft, and hard bands. The vertical dotted lines indicate the median effective exposures of 207.1, 206.0, and 210.6 ks, for the full, soft, and hard bands, respectively.
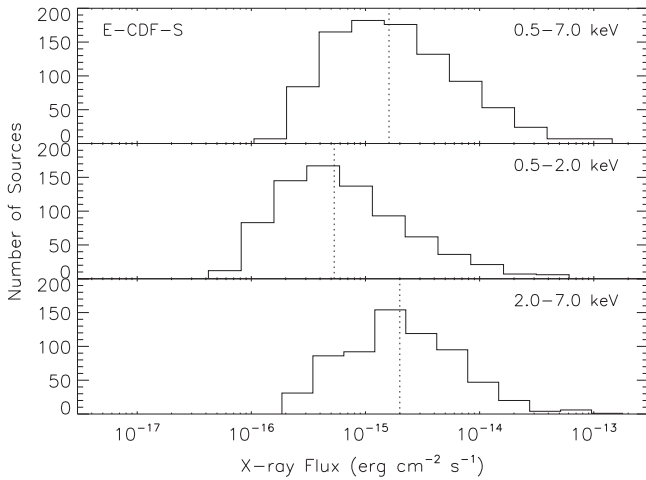

Figure 40. Distributions of X-ray fluxes for the 250 ks E-CDF-S main-catalog sources in the full, soft, and hard bands. Sources with upper limits are not plotted. The vertical dotted lines denote the median fluxes of 1.6×10^{-15}, 5.3×10^{-16} and 2.0×10^{-15} erg cm^{-2} s^{-1} for the full, soft, and hard bands, respectively.

in Section 3.3.3, a main-catalog source with a secure ONIR counterpart is almost certain to be real (note that sources without ONIR counterparts are more likely but not necessarily false detections).

Figures 42–44 display $25'' \times 25''$ postage-stamp images from the WFI R band (Giavalisco et al. 2004), the TENIS WIRCam K_s band (Hsieh et al. 2012), and the SIMPLE IRAC 3.6 μm band (Damen et al. 2011), overlaid with adaptively smoothed full-band X-ray contours for the main-catalog sources, respectively.

3.3.7. Properties of the 275 New Main-catalog Sources

Figure 45(a) displays the spatial distributions of the 275 new main-catalog sources (i.e., 238 new AGNs, 31 new galaxies, and 6 new stars that are all indicated as filled symbols) and the 728 old main-catalog sources (indicated as open symbols), whose colors are coded based on source types (red for AGNs, black for galaxies, and blue for stars) and whose symbol sizes represent different P values (larger sizes denote lower P values
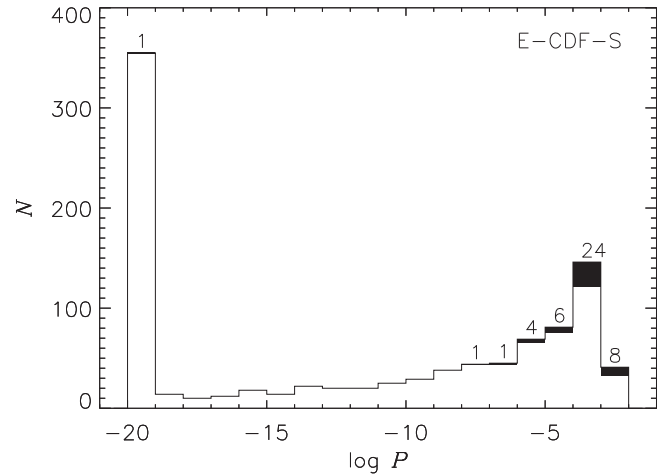

Figure 41. Distribution of the AE-computed binomial no-source probability, P, for the 250 ks E-CDF-S main-catalog sources. The values of $\log P < -20$ are set to $\log P = -20$ for easy illustration. The shaded areas denote sources without multiwavelength counterparts, with their corresponding numbers annotated.

and thus higher source-detection significances). Figure 45(c) shows the histograms of off-axis angles for different source types for the main-catalog sources.

Figures 45(e) and (f) show the observed source density as a function of off-axis angle for all the main-catalog sources and the new main-catalog sources, respectively. These two plots reveal, for either all or new sources, that (1) the source densities decline toward large off-axis angles due to the decreasing sensitivities (see Section 3.6.2); and (2) overall, observed AGN densities are larger than observed galaxy densities. In the central $\theta \leqslant 3'$ areas of the four E-CDF-S observation fields, the averaged observed source densities for all sources, all AGNs, and all galaxies reach 5800^{+1000}_{-900} deg^{-2}, 5200^{+1000}_{-800} deg^{-2}, and 500^{+400}_{-200} deg^{-2}, respectively; and the averaged observed source densities for all new sources, new AGNs, and new galaxies reach 1900^{+600}_{-500} deg^{-2}, 1600^{+600}_{-500} deg^{-2}, and 200^{+300}_{-200} deg^{-2}, respectively.

Figure 46 displays (a) observed-frame full-band flux versus adopted redshift, (b) absorption-corrected, rest-frame 0.5–7 keV luminosity versus adopted redshift, and (c) band ratio versus absorption-corrected, rest-frame 0.5–7 keV luminosity, for the new sources (indicated as filled circles) and old sources (indicated as open circles), respectively. We find that (1) the new sources typically have smaller X-ray fluxes and luminosities than the old sources (also see Figure 47); and (2) the median value of 1.71 of band ratios or upper limits on band ratios of the 83 new sources is larger than the corresponding median value of 0.84 of the 548 old sources (also see Figure 49). We further utilize survival-analysis 2-sample tests to quantify the difference in band ratios between the above 83 new sources and 548 old sources that involve censored data, which give $p = 0.0$ results indicating that there is a significant difference in band ratios between the above new and old sources. Together, the above observations indicate that our improved cataloging methodology allows us to probe more fainter obscured sources than L05.

Figure 47 presents histograms of observed-frame full-band flux and absorption-corrected, rest-frame 0.5–7 keV luminosity for the new AGNs and galaxies (main panels) as well as the old AGNs and galaxies (insets). It is apparent that AGNs and
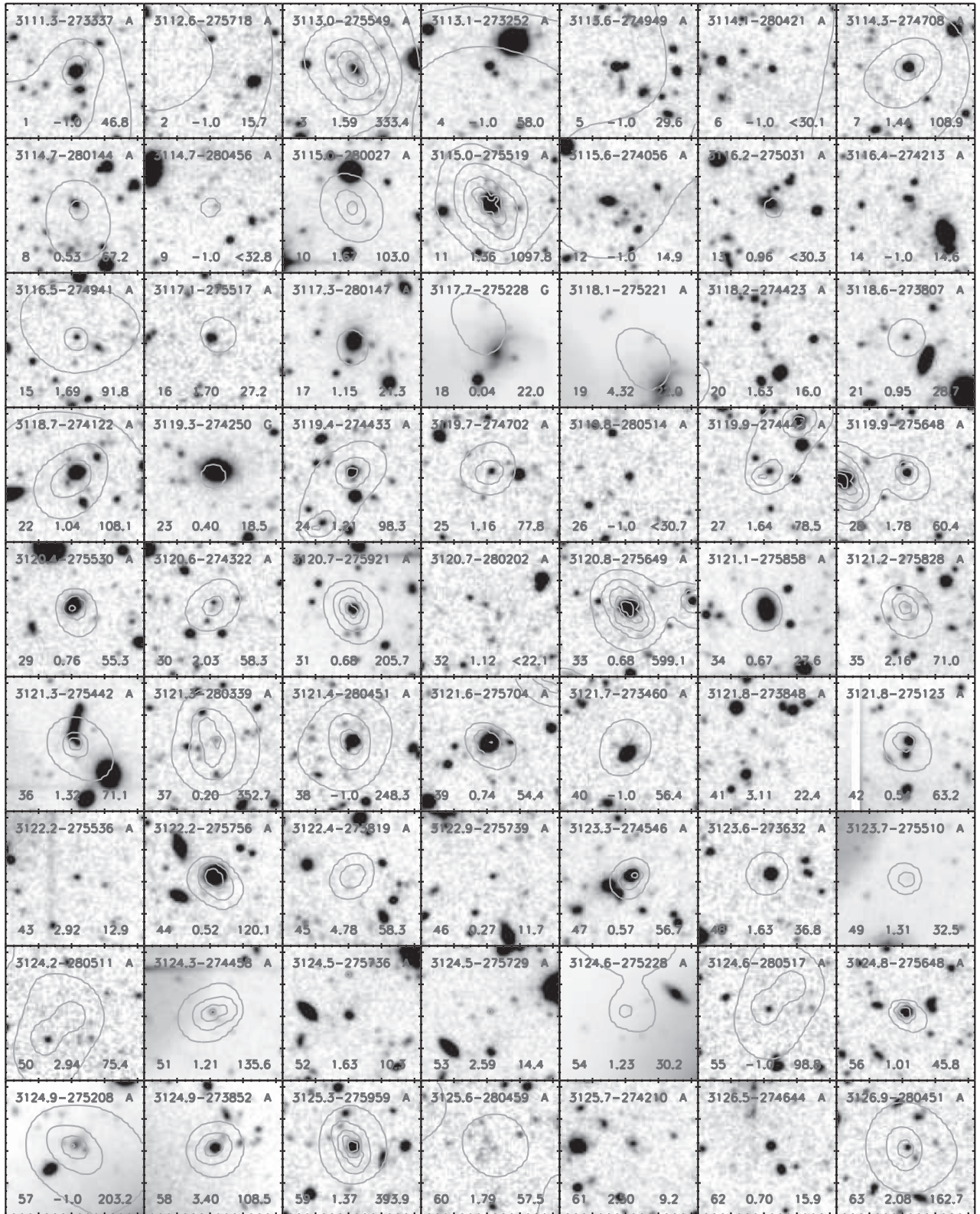
Figure 42. $25'' \times 25''$ postage-stamp images from the WFI *R* band (Giavalisco et al. 2004) for the 250 ks E-CDF-S main-catalog sources that are centered on the X-ray positions, overlaid with full-band adaptively smoothed X-ray contours that have a logarithmic scale and range from ≈0.003%–30% of the maximum pixel value. In each image, the labels at the top are the source name (the hours "03" of R.A. are omitted for succinctness) and source type (A = AGN, G = Galaxy, and S = Star); the bottom numbers indicate the source X-ray ID number, adopted redshift, and full-band counts or upper limit (with a "<" sign). In some cases there are no X-ray contours present, either due to these sources not being detected in the full band or having low full-band counts leading to their observable emission in the adaptively smoothed image being suppressed by CSMOOTH. (An extended version of this figure is available.)
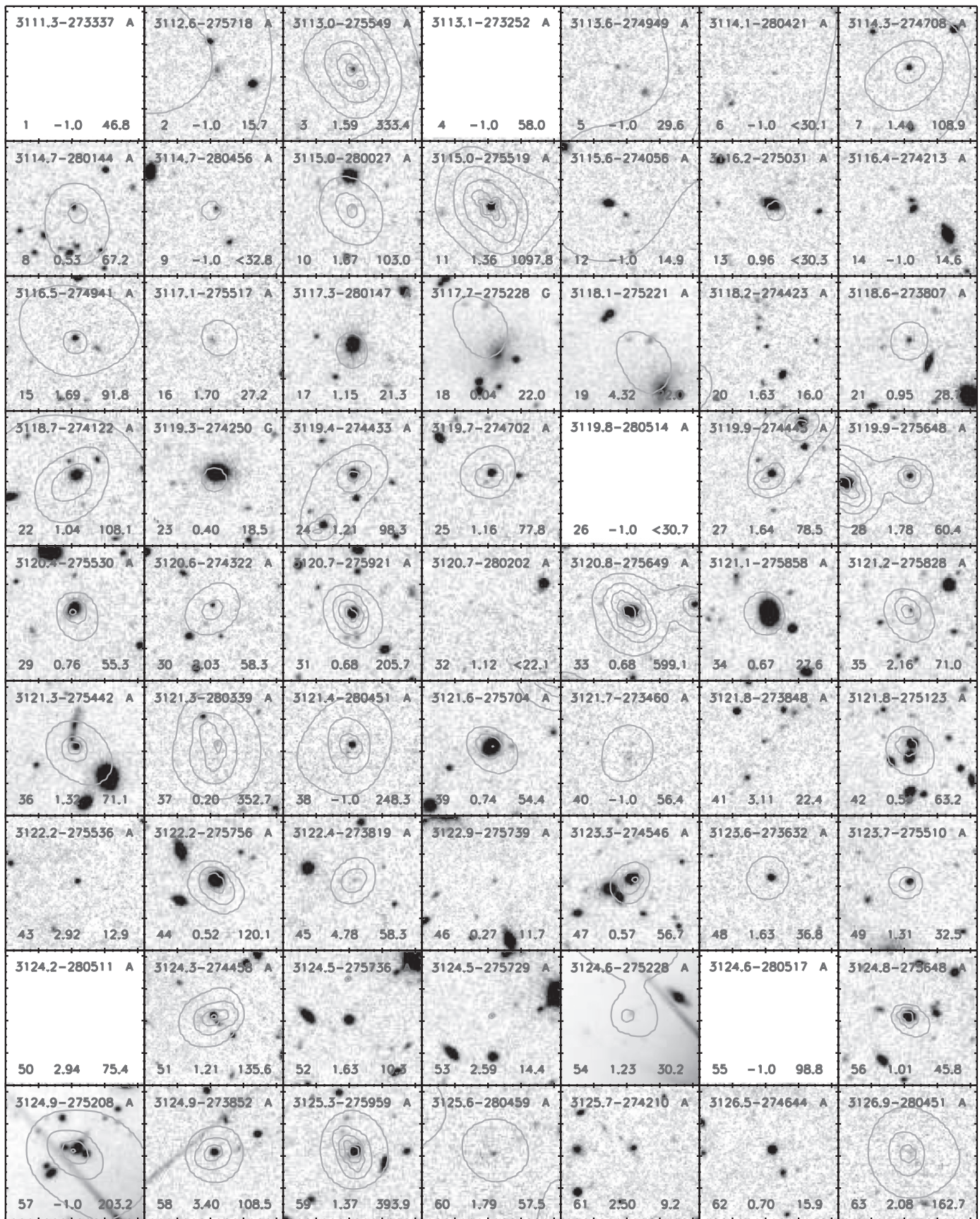
Figure 43. Same as Figure 42, but for the TENIS WIRCam K_s band (Hsieh et al. 2012). In some cases there is no K_s-band coverage (e.g., XIDs = 1, 4, 26, 50, 55).
(An extended version of this figure is available.)
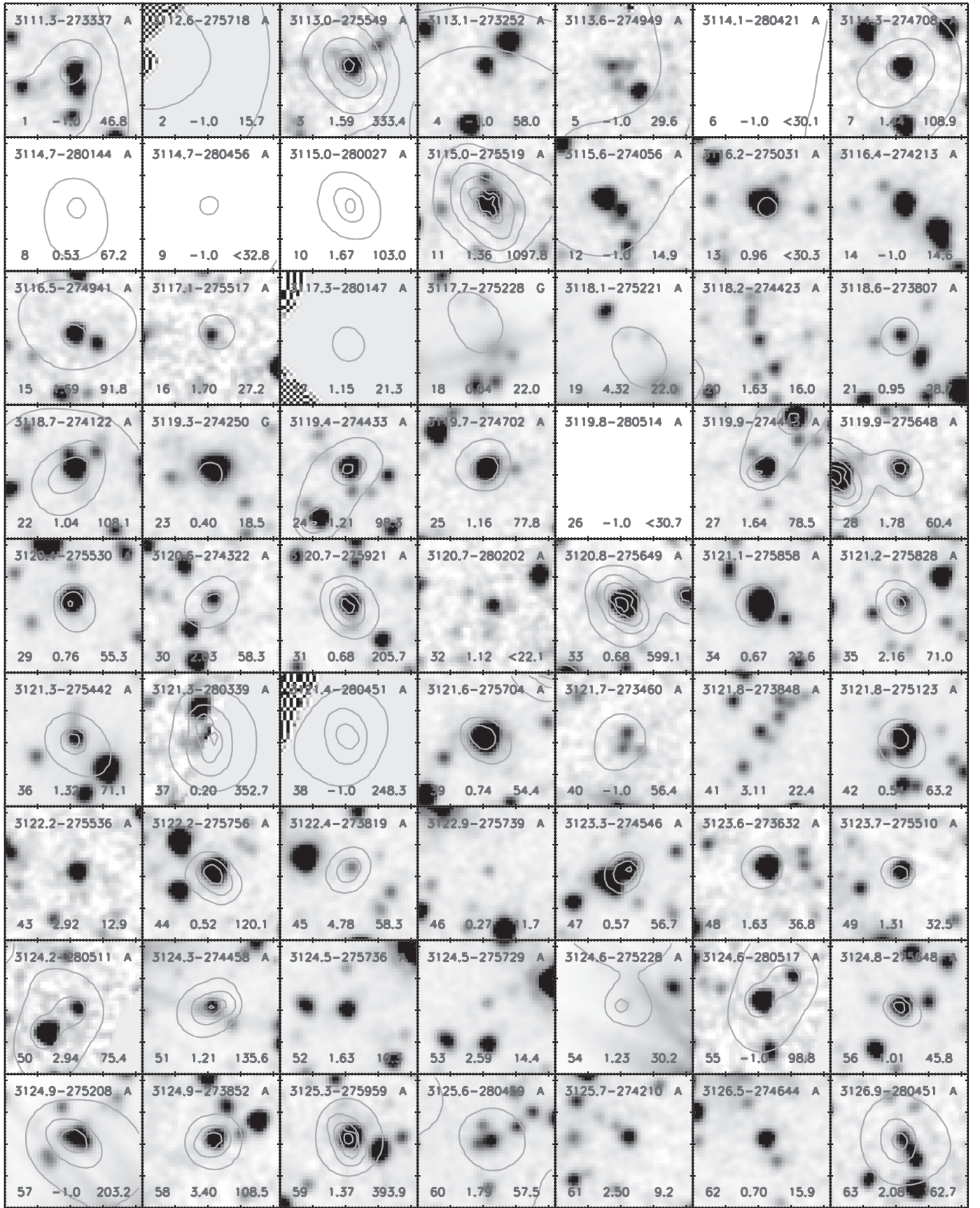
Figure 44. Same as Figure 42, but for the SIMPLE IRAC 3.6 μm band (Damen et al. 2011). In some cases there is partial (e.g., XIDs = 2, 17, 38) or no IRAC 3.6 μm band coverage (e.g., XIDs = 6, 8, 9, 10, 26). (An extended version of this figure is available.)
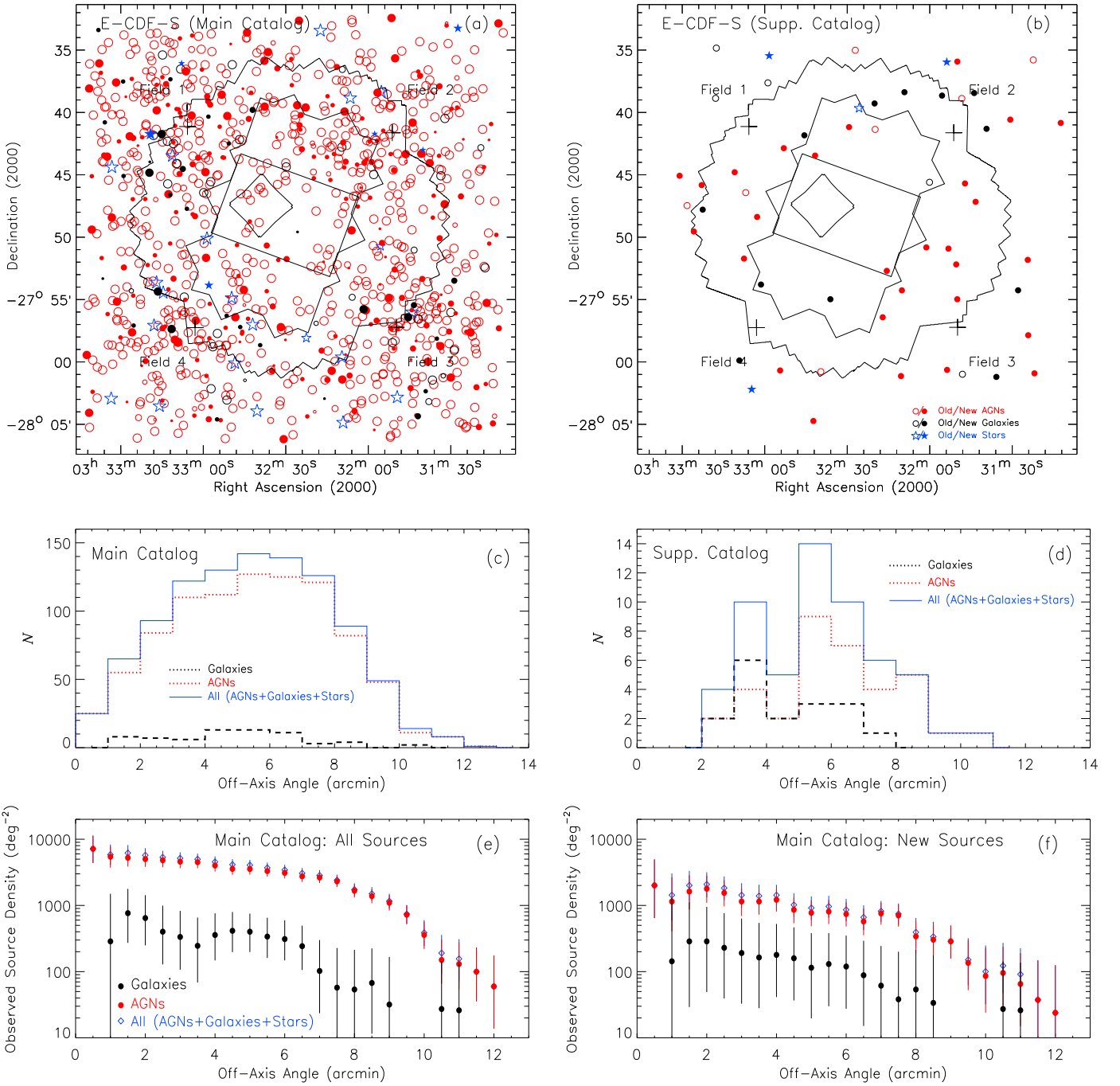
Figure 45. (Top) spatial distributions for (a) the 250 ks E-CDF-S main-catalog sources and (b) the supplementary-catalog sources. Sources classified as AGNs, galaxies, and stars are plotted as red, black, and blue symbols, respectively. Open symbols indicate old sources that were previously detected in (a) the L05 main catalog or (b) the L05 main or supplementary catalog, while filled symbols indicate new sources that were not previously detected in the L05 main and/or supplementary catalog. The regions and the plus signs have the same meanings as those in Figure 30. In panel (a), larger symbol sizes indicate lower AE binomial no-source probabilities, ranging from $\log P > -3$, $-4 < \log P \leqslant -3$, $-5 < \log P \leqslant -4$, to $\log P \leqslant -5$; while in panel (b), all sources have $\log P > -3$ and are plotted as symbols of the same size. (Middle) distributions of off-axis angles for different source types for (c) the main-catalog sources and (d) the supplementary-catalog sources. (Bottom) observed source densities broken down into different source types as a function of off-axis angle (θ) for (e) all the 250 ks E-CDF-S main-catalog sources and (f) the *new* main-catalog sources, which are calculated in bins of $\Delta\theta = 1'$ and whose 1σ errors are computed utilizing Poisson statistics.

galaxies have disparate distributions of flux and luminosity, no matter whether the new or old sources are considered (except in the main panel of Figure 47(a) where the flux distributions for the new AGNs and galaxies are somewhat similar to each other).

Figure 48(a) displays the band ratio as a function of full-band count rate for the new sources (indicated as filled

symbols) and the old sources (indicated as open symbols), with the large crosses, triangles, and diamonds representing the average (i.e., stacked) band ratios for all AGNs, all galaxies, and all sources (counting both AGNs and galaxies), respectively. The overall average band ratio is, as expected, dominated by AGNs, which has a rising and then leveling-off shape toward low full-band count rates (down to
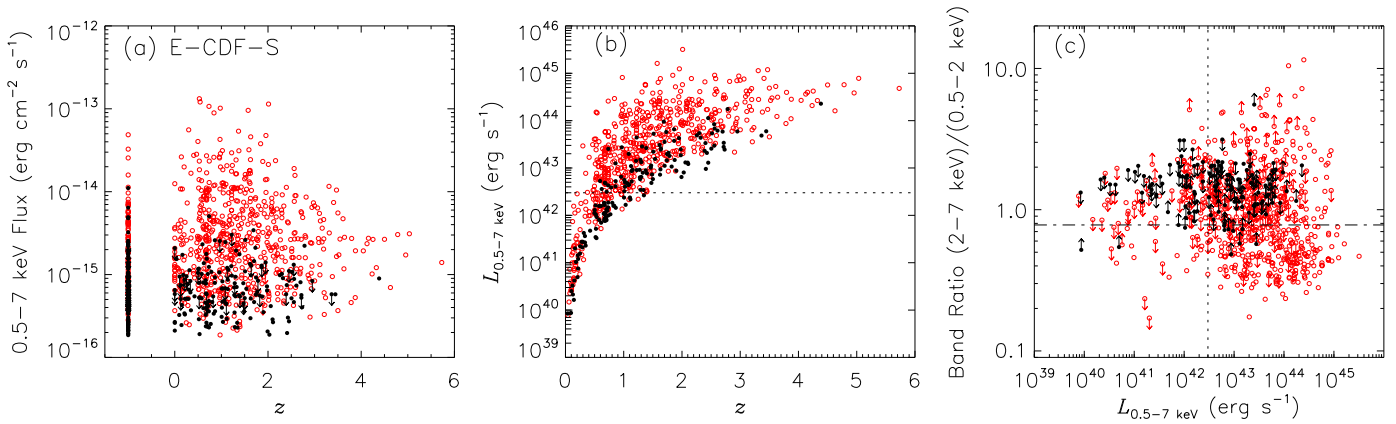
Figure 46. (a) Observed-frame full-band flux vs. adopted redshift, (b) absorption-corrected, rest-frame 0.5–7 keV luminosity vs. adopted redshift, and (c) band ratio vs. absorption-corrected, rest-frame 0.5–7 keV luminosity for the 250 ks E-CDF-S main-catalog sources. Red open circles indicate old sources while black filled circles indicate new sources. Arrows denote limits. In panel (b), sources with no redshift estimates are not plotted; in panel (c), sources with no redshift estimates or sources having only full-band detections are not plotted. The dotted lines in panels (b) and (c) and the dash–dotted line in panel (c) correspond to the threshold values of two AGN-identification criteria, $L_{0.5-7\,\mathrm{keV}} \geqslant 3 \times 10^{42}$ erg s^{-1} and $\Gamma \leqslant 1.0$.
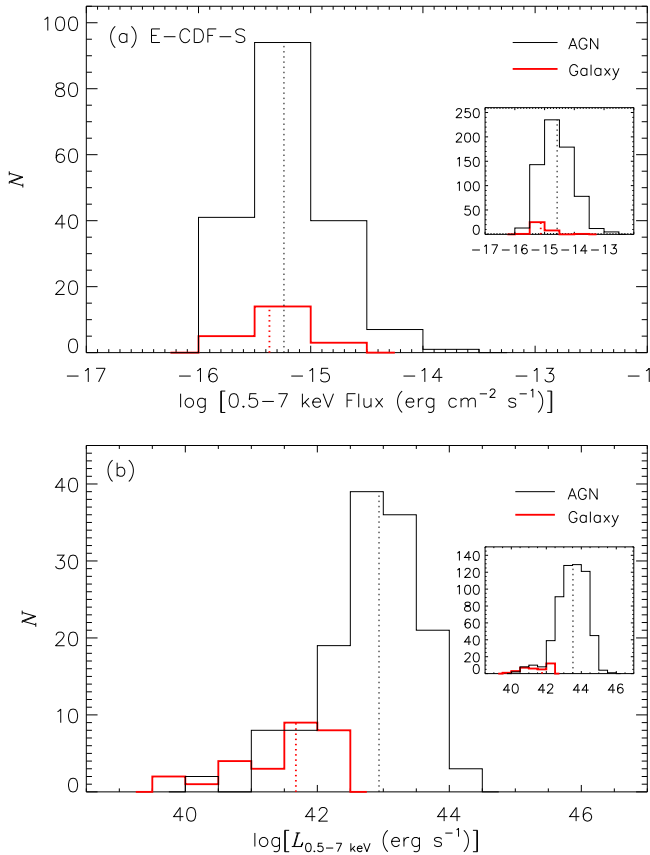
Figure 47. Histograms of (a) observed-frame full-band flux and (b) absorption-corrected, rest-frame 0.5–7 keV luminosity for the new 250 ks E-CDF-S main-catalog sources. The insets display results for the old main-catalog sources. The vertical dotted lines indicate the median values. In panel (a), sources without full-band detections are not included; in panel (b), sources without redshift estimates are not included.

2×10^{-5}–3×10^{-5} count s^{-1}) that is in general agreement with that seen in Figure 20(a) for the 2 Ms CDF-N. Figure 48(b) presents the fraction of new sources as a function of full-band count rate for the sources in the main catalog. From full-band count rates of 2.3×10^{-3} count s^{-1} to 2.3×10^{-5} count s^{-1}, the fraction of new sources rises monotonically from 0% to $\approx$60%.

Figure 49 presents the average band ratio in bins of adopted redshift and X-ray luminosity for the new AGNs, old AGNs, new galaxies, and old galaxies, respectively. A couple of observations can be made, e.g.,: (1) the new AGNs have larger band ratios than the old AGNs no matter which bin of redshift or X-ray luminosity is considered, with the only exception of the second lowest luminosity bin, reflecting the rise of obscured AGNs toward faint fluxes (e.g., Bauer et al. 2004; Lehmer et al. 2012); and (2) the new galaxies have larger band ratios than the old galaxies no matter which bin of redshift or X-ray luminosity is considered (but note the relatively limited source statistics here).

Figure 50(a) presents the WFI R-band magnitude versus the full-band flux for the new sources (indicated as filled symbols) and old sources (indicated as open symbols), as well as the approximate flux ratios for AGNs and galaxies, where the sources are color-coded with red for AGNs, black for galaxies, and blue for stars, respectively. As a comparison, Figure 50(c) presents the IRAC 3.6 μm magnitude versus the full-band flux for the new sources and old sources. Overall, a total of 909 (90.6%) of the sources in the main catalog are likely AGNs, the vast majority of which lie in the region expected for relatively luminous AGNs that have $\log(f_X/f_R) > -1$ (i.e., dark gray areas in Figure 50(a)); among these 909 AGNs, 238 (26.2%) are new. A total of 67 (6.7%) of the sources in the main catalog are likely galaxies, and by selection all of them (excluding several with upper limits on full-band fluxes) lie in the region expected for normal galaxies, starburst galaxies, and low-luminosity AGNs that have $\log(f_X/f_R) \leqslant -1$ (i.e., light gray areas in Figure 50(a)); among these 67 sources, 31 (46.3%) are new. Only 27 (2.7%) of the sources in the main catalog are likely stars, with all but one having low X-ray-to-optical flux ratios; among these 27 stars, 6 are new. Among the new sources, normal and starburst galaxies total a fraction of 11.3%, as opposed to 4.9% if the old sources are considered, which is expected due to galaxies having a steeper number-count slope than AGNs (e.g., Bauer et al. 2004; Lehmer et al. 2012).

Figure 51 presents the histograms of X-ray-to-optical flux ratios for the new AGNs, old AGNs, new galaxies, and old galaxies, respectively. It is apparent that (1) there is no significant difference between the X-ray-to-optical flux ratio distributions for the new and old AGNs; and (2) there is some slight difference between the X-ray-to-optical flux ratio
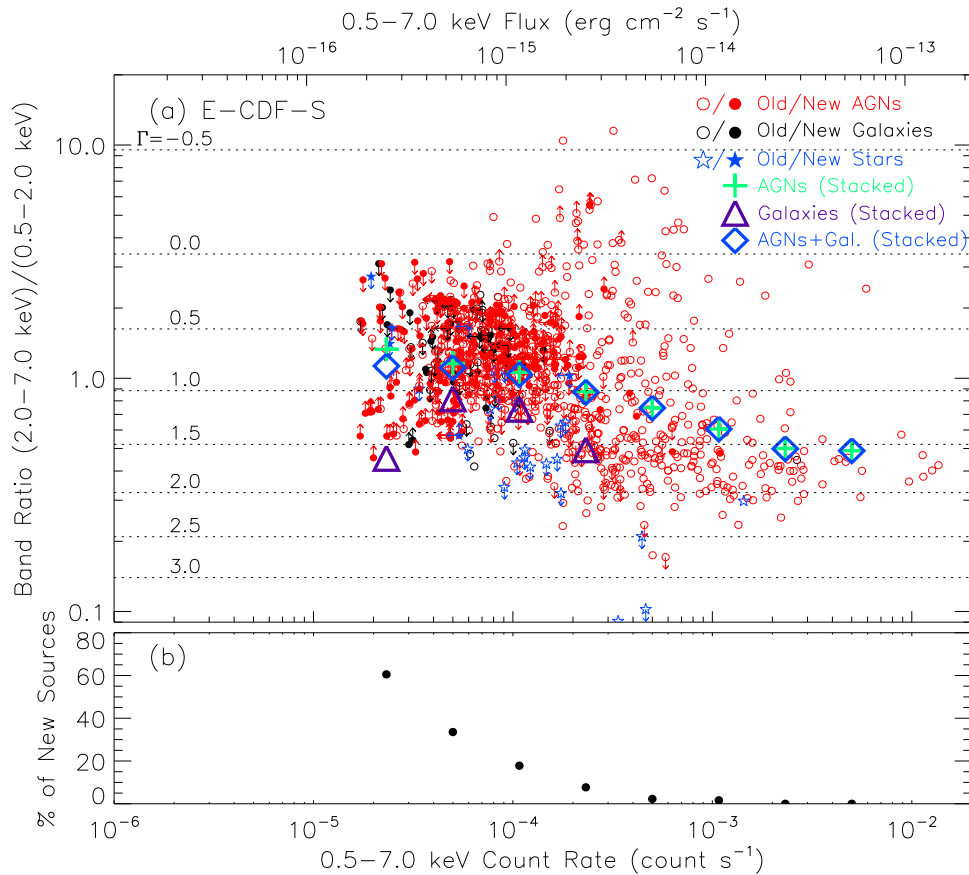
Figure 48. (a) Band ratio vs. full-band count rate for the 250 ks E-CDF-S main-catalog sources. For reference, the top x-axis displays representative full-band fluxes that are derived using full-band count rates given an assumed $\Gamma = 1.4$ power law. The meanings of symbols of different types and colors are indicated by the legend. Arrows indicate limits. Sources with only full-band detections are not plotted; there are only 57 (57/1003 = 5.7%) such sources, the exclusion of which would not affect our results significantly. Large crosses, triangles, and diamonds denote average/stacked band ratios as a function of full-band count rate that are derived in bins of Δlog(Count Rate) = 0.6, for AGNs, galaxies, and both AGNs and galaxies, respectively. Horizontal dotted lines indicate the band ratios that correspond to given effective photon indexes. (b) Fraction of new sources as a function of full-band count rate for the 250 ks E-CDF-S main-catalog sources, computed in bins of Δlog (Count Rate) = 0.6.

distributions for the new and old galaxies, with the former having slightly larger X-ray-to-optical flux ratios.

3.4. Supplementary Near-infrared Bright Chandra Source Catalog

#### 3.4.1. Supplementary Catalog Production

Among the 431 (i.e., 1434−1003 = 431) candidate-list X-ray sources that do not satisfy the main-catalog source-selection criterion of $P < 0.002$, 271 are of moderate significance, with $0.002 \leqslant P < 0.1$. In order to retrieve genuine X-ray sources from this sample of 271 sources, we create a supplementary catalog that consists of the subset of these sources having bright near-infrared counterparts, again using the prior-based source-searching method. We match these 271 Chandra sources with the $K_s \leqslant 22.3$ mag sources in the TENIS WIRCam K_s-band catalog using a matching radius of 1″.2. A total of 56 near-infrared bright X-ray sources are identified this way, with ≈5.9 false matches expected (i.e., a false-match rate of 10.5%). Our supplementary catalog includes six L05 main-catalog sources that are not recovered in our main catalog and seven L05 supplementary optically bright sources, thus resulting in a total of 56−6−7 = 43 new supplementary-catalog sources that are not present in either of the L05 catalogs. A point worth noting is that the vast majority (28 out of 33;

84.8%) of the L05 supplementary optically bright ($R < 23$ mag) sources are included either in our main catalog (21 sources) or supplementary catalog (the aforementioned 7 sources).

Our 56-source supplementary catalog is presented in Table 12, in the same format as Table 9 (see Section 3.3.4 for the details of each column). A source-detection criterion of $P < 0.1$ is adopted for photometry-related calculations for the supplementary-catalog sources; and the multiwavelength identification-related columns (i.e., Columns 18–22) are set to the TENIS WIRCam K_s-band matching results.

3.4.2. Properties of Supplementary-catalog Sources

Figure 45(b) displays the spatial distribution of the 56 supplementary-catalog sources, with the 43 new sources denoted as filled symbols; and Figure 45(d) presents the histograms of off-axis angles for different source types for the supplementary-catalog sources. Figures 50(b) and (d) present the WFI R-band magnitude and the SIMPLE IRAC 3.6 μm magnitude versus the full-band flux for the supplementary-catalog sources, respectively. Among the 56 supplementary-catalog sources, 35 (62.5%), 17 (30.4%), and 4 (7.1%) are likely AGNs, galaxies, and stars, respectively. A total of 47
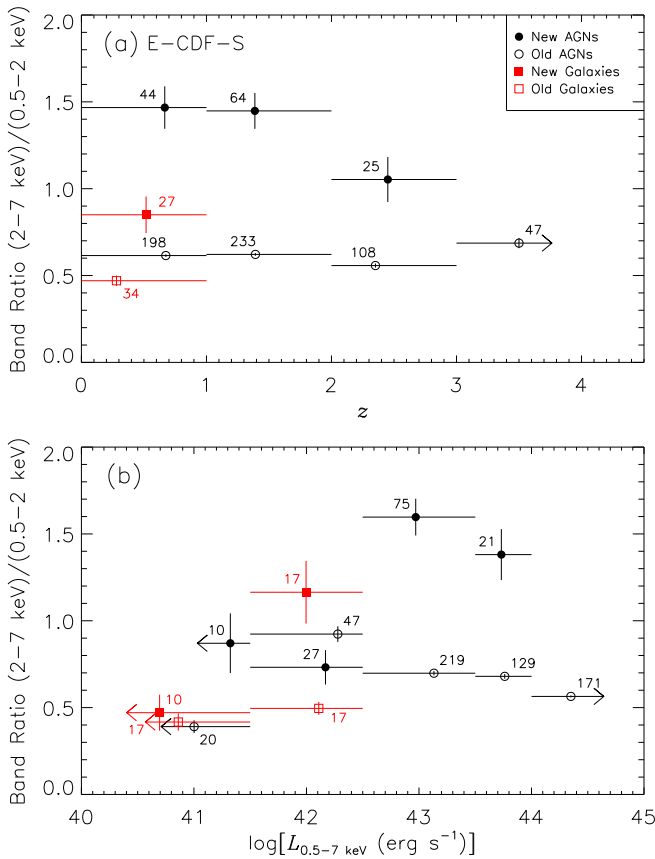
Figure 49. Average/stacked band ratios in bins of (a) redshift ($0 < z < 1$, $1 \leqslant z < 2$, $2 \leqslant z < 3$, and $z \geqslant 3$) and (b) absorption-corrected, rest-frame 0.5–7 keV luminosity [$\log(L_X) < 41.5$, $41.5 \leqslant \log(L_X) < 42.5$, $42.5 \leqslant \log(L_X) < 43.5$, $43.5 \leqslant \log(L_X) < 44.0$, and $\log(L_X) \geqslant 44.0$] for the new and old 250 ks E-CDF-S main-catalog sources. The meanings of symbols are indicated by the legend. In each bin, the median redshift or X-ray luminosity is used for plotting; the number of stacked sources is annotated.

(90.4%) of the 52 non-star sources have either $z_{\rm spec}$'s or $z_{\rm phot}$'s, ranging from 0.128 to 2.437 with a median redshift of 0.838.

3.5. Completeness and Reliability Analysis

Following Section 2.5, we produce a set of nine simulated ACIS-I observations that closely mimic the real E-CDF-S observations, obtain a simulated merged 250 ks E-CDF-S event file, construct images for the three standard bands, run WAVDETECT (sigthresh $= 10^{-5}$) to produce a candidate-list catalog, and make use of AE to extract photometry (including P values) for the candidate-list sources.

Figure 52 displays the completeness and reliability as a function of the AE-computed binomial no-source probability within the $\theta \leqslant 6'$ regions and the entire E-CDF-S field, for the simulations in the full, soft, and hard bands, for sources with at least eight and four counts, respectively. The case of four counts is close to our on-axis (i.e., $\theta \lesssim 3'$) source-detection limit in the full and hard bands. It seems clear from Figure 52 that (1) in all panels, as expected, each completeness curve goes up and each reliability curve goes down toward large P threshold values, and the completeness level for the case of eight counts is higher than that for the case of four counts; and (2) the completeness levels for both the case with 8 counts and that with 4 counts are higher within the $\theta \leqslant 6'$ regions than the

corresponding completeness levels in the entire E-CDF-S field. At our adopted main-catalog P threshold of 0.002, the completeness levels within the $\theta \leqslant 6'$ regions are 96.6% and 79.9% (full band), 100.0% and 99.8% (soft band), and 96.8% and 82.4% (hard band) for sources with $\geqslant 8$ and $\geqslant 4$ counts, respectively. The completeness levels for the entire E-CDF-S field are 81.7% and 62.6% (full band), 97.1% and 79.3% (soft band), and 87.7% and 64.1% (hard band) for sources with $\geqslant 8$ and $\geqslant 4$ counts, respectively. At our adopted main-catalog P threshold of 0.002, the reliability level ranges from 98.8% to 99.8% for all panels; and we estimate that in the main catalog (i.e., the entire E-CDF-S field), there are about 8, 4, and 2 false detections with $\geqslant 8$ counts in the full, soft, and hard bands, and about 8, 6, and 3 false detections with $\geqslant 4$ counts in the full, soft, and hard bands, respectively.

Figure 53 presents the completeness as a function of flux given the main-catalog $P < 0.002$ criterion for the full-, soft-, and hard-band simulations. The three curves of completeness versus flux that are derived from the simulations (dashed lines) approximately track the normalized sky coverage curves that are derived from the real E-CDF-S observations (solid curves). Table 13 presents the flux limits corresponding to four specific completeness levels in the full, soft, and hard bands, which are denoted as horizontal dotted lines in Figure 53.

### 3.6. Background and Sensitivity Analysis

3.6.1. Background Map Creation

We follow Section 2.6.1 to create background maps for the three standard-band images. Table 14 summarizes the background properties, including the mean background, total background, and count ratio between background counts and detected source counts for the three standard bands. 97.1%, 99.1%, and 98.0% of the pixels have zero background counts in the background maps for the full, soft, and hard bands, respectively. The values in Table 14 are systematically slightly lower than those reported in Table 7 of L05, mainly due to the fact that we adopt a smaller upper energy bound of 7 keV than the value of 8 keV adopted in L05 and that we adopt a more stringent approach for data filtering (see Section 3.1). Figure 54 displays the full-band background map.

Figure 55 presents the mean *Chandra* background spectra that are calculated for the 1003 main-catalog sources in various bins of off-axis angle, using the individual background spectra extracted in Section 3.2. We find that (1) the shapes of the mean *Chandra* background spectra remain largely the same across the entire E-CDF-S field given the uncertainties, especially as far as the $\gtrsim 1$ keV parts of the spectra are concerned (with $\lesssim 10\%$ variations between the shapes); (2) for the $\lesssim 1$ keV parts of the mean background spectra, shape variations seem slightly more apparent (up to $\approx 20\%$); and (3) compared to the shapes of the mean CDF-N background spectra shown in Figure 27, the E-CDF-S background spectra have very similar shapes at $\gtrsim 1$ keV, but seem to level off slightly at $\lesssim 1$ keV, probably due to cosmic variance and/or variations of *Chandra* instrument status.

3.6.2. Sensitivity Map Creation

We follow Section 2.6.2 to create sensitivity maps in the three standard bands for the main catalog (i.e., using $P < 0.002$) to assess the sensitivity as a function of position across the entire field. We find that there are 12, 11, and 22
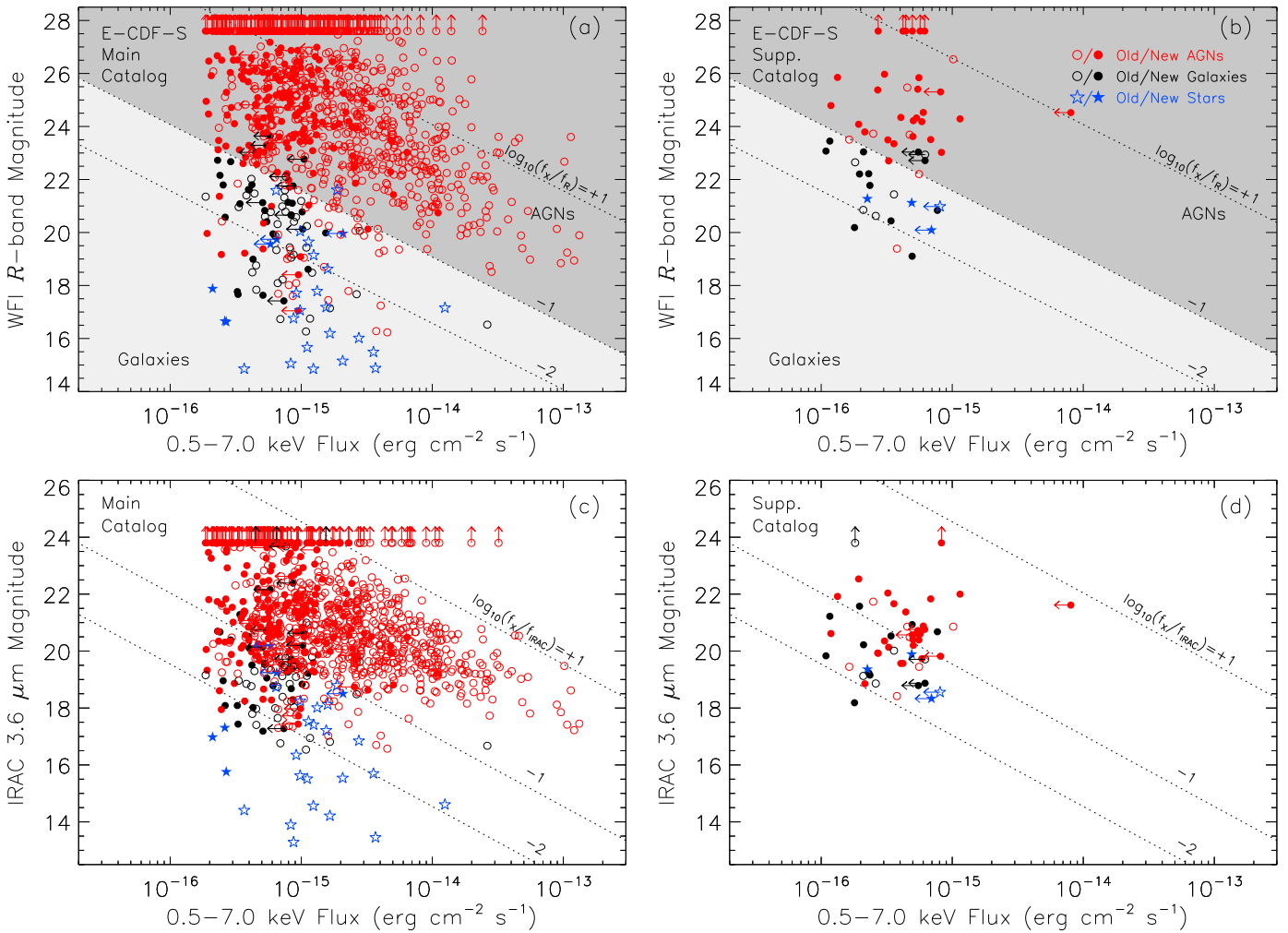
Figure 50. (Top) WFI *R*-band magnitude vs. full-band flux for (a) the 250 ks E-CDF-S main-catalog sources and (b) the supplementary-catalog sources. (Bottom) IRAC 3.6 *μ*m magnitude vs. full-band flux for (c) the 250 ks E-CDF-S main-catalog sources and (d) the supplementary-catalog sources. The meanings of the symbols of different types and colors are indicated by the legend. Arrows denote limits. In panels (a) and (b), diagonal dotted lines indicate constant full-band-to-*R* flux ratios, and shaded areas represent approximate flux ratios for AGNs (dark gray) and galaxies (light gray). In panels (c) and (d), diagonal dotted lines indicate constant full-band-to-IRAC-3.6 *μ*m flux ratios.

main-catalog sources in the three standard bands that lie typically $\lesssim 10\%$ below the corresponding derived sensitivity limits, respectively, which is likely due to background fluctuations and/or their real Γ values differing significantly from the assumed $\Gamma = 1.4$.

Figure 56 displays the full-band sensitivity map for the main catalog, and Figure 57 presents plots of survey solid angle versus flux limit in the three standard bands given $P < 0.002$. It is clear that higher sensitivities are reached at smaller off-axis angles and thus within smaller survey solid angles. The central ≈ 1 arcmin^2 areas at the four aim points have mean sensitivity limits of $\approx 2.0 \times 10^{-16}$, 7.6×10^{-17}, and 3.0×10^{-16} erg cm^{-2} s^{-1} for the full, soft, and hard bands, respectively, which represent a factor of ≈ 1.5–2.0 improvement over those of L05, due to the fact that we adopt a sensitive two-stage source-detection procedure and that L05 adopted a different methodology for sensitivity calculations.

4. SUMMARY

We present the improved *Chandra* point-source catalogs, associated data products, and basic analyses of detected

X-ray sources for the 2 Ms CDF-N and 250 ks E-CDF-S, implementing a number of improvements in the *Chandra* source cataloging methodology listed in Table 1. In particular, the combination of sophisticated and accurate X-ray photometry extraction, as well as the sensitive and reliable two-stage source-detection approach, enables the probing of fainter and more obscured sources with higher confidence in their validity than the previous A03 CDF-N and L05 E-CDF-S catalogs, without new *Chandra* observational investment. As such, the improved catalogs allow better characterization of all the ≈ 1800 CDF-N and E-CDF-S sources, including the ≈ 500 newly detected ones, thereby superseding the A03 and L05 catalogs. In addition to the point-source catalogs, we also make other associated data products publicly available, including the final event files, raw images, effective exposure maps, background maps, sensitivity maps, and solid-angle versus flux-limit curves for the 2 Ms CDF-N and 250 ks E-CDF-S (see footnote 13). Below we summarize the most significant results for CDF-N and E-CDF-S, respectively.

For 2 Ms CDF-N, the key results are as follows.
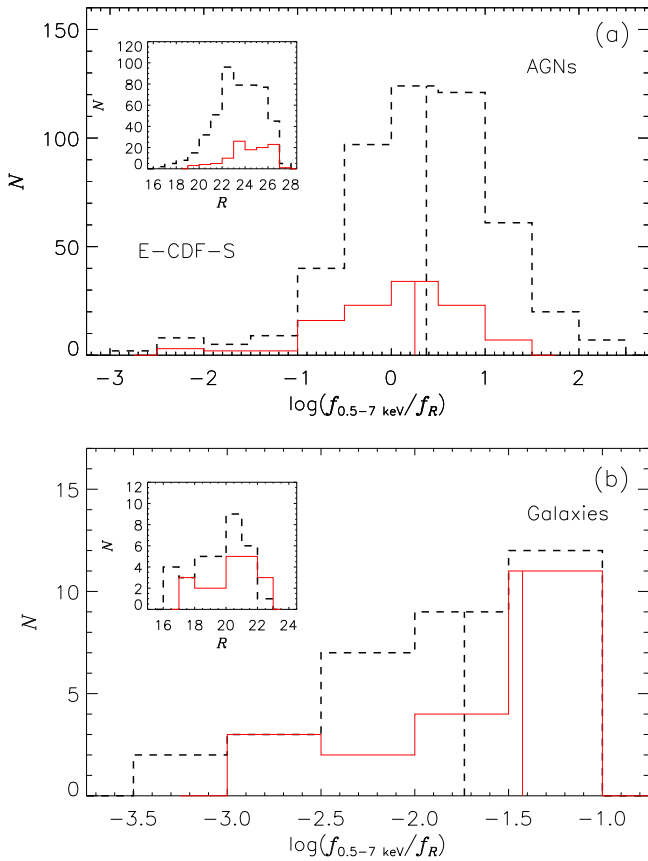
Figure 51. Histograms of X-ray-to-optical (*R* band) flux ratios for (a) the new 250 ks E-CDF-S main-catalog AGNs (solid histogram) and old AGNs (dashed histogram) and (b) new galaxies (solid histogram) and old galaxies (dashed histogram), with median flux ratios denoted by vertical lines. The insets display the histograms of *R*-band magnitude for new sources (solid histograms) and old sources (dashed histograms). Only sources with both full-band and *R*-band detections are plotted.

1. The entire CDF-N is made up of 20 individual observations, which have a total effective exposure of 1.896 Ms and cover a total solid angle of 447.5 arcmin^2.

2. The CDF-N main catalog consists of 683 sources that are detected by running WAVDETECT at a false-positive probability threshold of 10^{-5} and meet our binomial-probability source-selection criterion of $P < 0.004$; such an approach is devised to maximize the number of reliable sources detected. These 683 sources are detected in up to three standard X-ray bands, i.e., 0.5–7.0 keV (full band), 0.5–2.0 keV (soft band), and 2–7 keV (hard band). 670 (98.1%) of these 683 sources have multiwavelength counterparts, and 638 (95.2% of 670) have either spectroscopic or photometric redshifts.

3. The CDF-N supplementary catalog contains 72 sources that are detected by running WAVDETECT at a false-positive probability threshold of 10^{-5} and meet the requirements of having $0.004 < P < 0.1$ and having bright ($K_s < 22.9$) near-infrared counterparts. 69 (95.8%) of these 72 sources have either spectroscopic or photometric redshifts.

4. X-ray source positions for the CDF-N main and supplementary catalogs are determined utilizing centroid and matched-filter techniques. The absolute astrometry of X-ray source positions is locked to that of the GOODS-N WIRCam K_s-band catalog and the median positional offset of the X-ray-K_s-band matches is $0\overset{''}{.}28$. The median X-ray positional uncertainties at the $\approx 68\%$ confidence level are $0\overset{''}{.}47$ and $0\overset{''}{.}80$ for the main and supplementary catalogs, respectively.

5. Basic analyses of the X-ray and multiwavelength properties of the CDF-N sources indicate that 86.5%, 11.0%, and 2.5% of the main-catalog sources are likely AGNs, galaxies, and stars, respectively. In the central $\theta \leqslant 3'$ area of the 2 Ms CDF-N, the observed main-catalog AGN and galaxy source densities reach $12{,}400^{+1400}_{-1300}$ deg^{-2} and 4200^{+900}_{-700} deg^{-2}, respectively. 47.2%, 52.8%, and 0.0% of the supplementary-catalog sources are likely AGNs, galaxies, and stars, respectively.

6. A total of 196 CDF-N main-catalog sources are new and are generally fainter and more obscured, compared to the A03 main-catalog sources. Among the 196 new main-catalog sources, 78.6% are likely AGNs and 19.9% are likely normal and starburst galaxies (with the remaining 1.5% being likely stars), which reflects the rise of normal and starburst galaxies at these very low flux levels. Indeed, galaxies become the numerically dominant source population that emerges at luminosities less than $\approx 10^{41.5}$ erg s^{-1}, according to our source-classification results.

7. Simulations demonstrate that our CDF-N main catalog is highly reliable ($\lesssim 5$, 4, and 3 false detections are expected in the full, soft, and hard bands, respectively) and is reasonably complete (e.g., in the central $\theta \leqslant 6'$ area, the completeness levels are $\gtrsim 82\%$, 95%, and 68% for sources with $\geqslant 8$ counts in the full, soft, and hard bands, respectively).

8. The CDF-N mean background is 0.167, 0.055, and 0.108 count Ms^{-1} pixel^{-1} for the full, soft, and hard bands, respectively; 91.7%, 97.1%, and 94.2% of the pixels have zero background counts in the background maps for the full, soft, and hard bands, respectively.

9. The 2 Ms CDF-N achieves on-axis flux limits of $\approx 3.5 \times 10^{-17}$, 1.2×10^{-17}, and 5.9×10^{-17} erg cm^{-2} s^{-1} for the full, soft, and hard bands, respectively, a factor of ≈ 2 improvement over those of A03, due to the facts that we adopt a sensitive two-stage source-detection procedure and that A03 adopted a different methodology for sensitivity calculations.

For 250 ks E-CDF-S, the key results are as follows.

1. The entire E-CDF-S is made up of 9 individual observations, which have a depth of ≈ 250 ks and cover a total solid angle of 1128.6 arcmin^2.

2. The E-CDF-S main catalog consists of 1003 sources that are detected by running WAVDETECT at a false-positive probability threshold of 10^{-5} and meet our binomial-probability source-selection criterion of $P < 0.002$; such an approach is devised to maximize the number of reliable sources detected. These 1003 sources are detected in up to three standard X-ray bands, i.e., 0.5–7.0 keV (full band), 0.5–2.0 keV (soft band), and 2–7 keV (hard band). 958 (95.5%) of these 1003 sources have multiwavelength counterparts, and 810 (84.6% of 958) have either spectroscopic or photometric redshifts.

3. The E-CDF-S supplementary catalog contains 56 sources that are detected by running WAVDETECT at a false-positive probability threshold of 10^{-5} and meet the requirements

Table 12
250 ks E-CDF-S Supplementary Near-infrared Bright *Chandra* Source Catalog

No. (1)	α_{2000} (2)	δ_{2000} (3)	$\log P$ (4)	WAVDETECT (5)	Pos Err (6)	Off-axis (7)	Full Band (8)	Full Band Upp Err (9)	Full Band Low Err (10)	Soft Band (11)	Soft Band Upp Err (12)	Soft Band Low Err (13)
1	03 31 12.66	−27 40 50.6	−2.3	−7	1.2	8.62	12.0	7.0	5.7	10.9	−1.0	−1.0
2	03 31 21.98	−28 00 55.2	−2.4	−7	1.2	7.18	8.4	6.3	5.0	9.2	−1.0	−1.0
3	03 31 22.67	−27 35 48.0	−2.7	−5	1.0	8.64	16.7	7.9	6.6	8.0	5.3	4.0
4	03 31 24.28	−27 57 52.0	−1.8	−5	1.3	5.70	4.5	4.3	2.8	7.8	−1.0	−1.0
5	03 31 24.51	−27 51 49.6	−1.1	−5	1.3	7.80	8.3	7.1	5.8	13.4	−1.0	−1.0

Note. The full table contains 97 columns of information for the 56 X-ray sources.

(This table is available in its entirety in machine-readable form.)
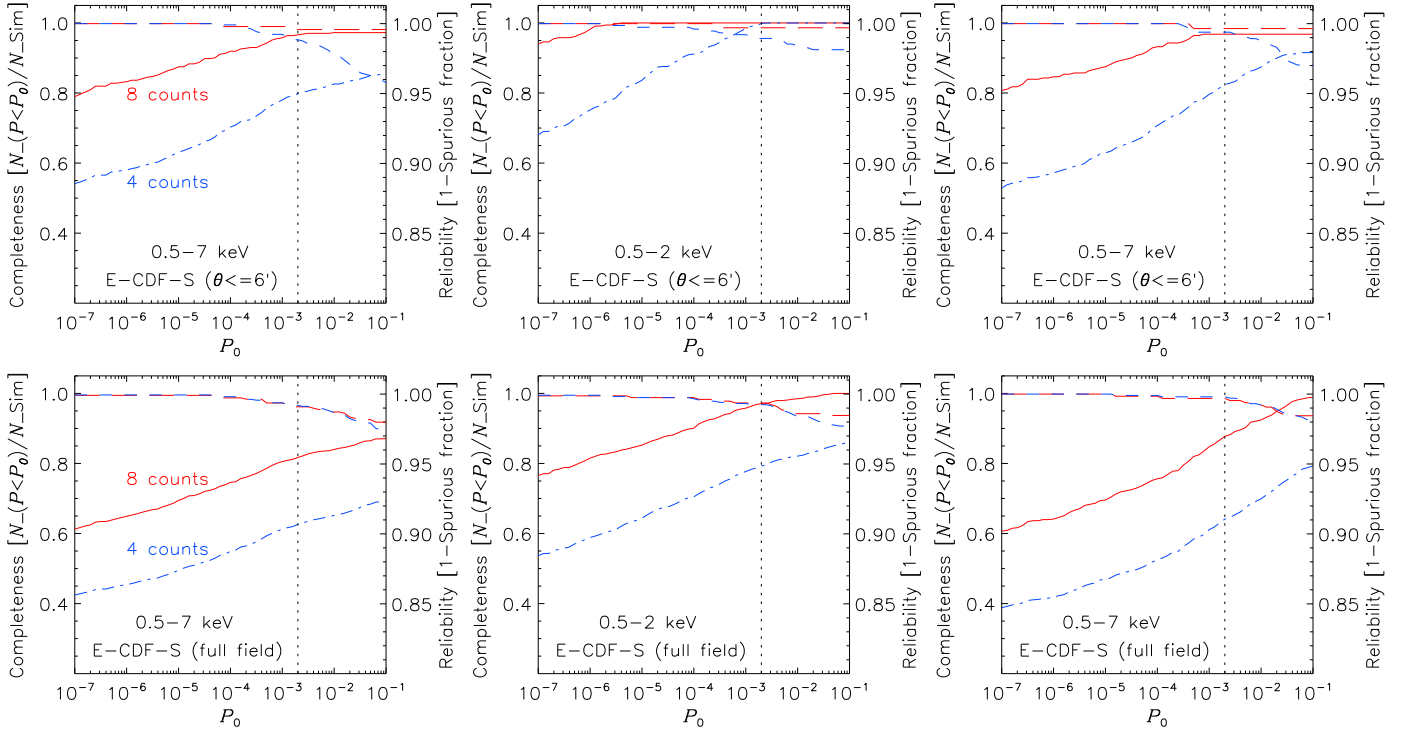
Figure 52. (Top) the $\theta \leqslant 6'$ case in the 250 ks E-CDF-S: completeness (solid and dashed–dotted curves; left y-axis) and reliability (long dashed and short dashed curves; right y-axis) as a function of P_0 ($P < P_0$ as the source-detection criterion) for the simulations in the full, soft, and hard bands, for sources with $\geqslant 8$ counts (red solid and long dashed curves) and $\geqslant 4$ counts (blue dashed–dotted and short dashed curves), respectively. The vertical dotted lines denote our adopted main-catalog source-detection threshold of $P_0 = 0.002$. (Bottom) same as top panels, but for the case of the full E-CDF-S field.
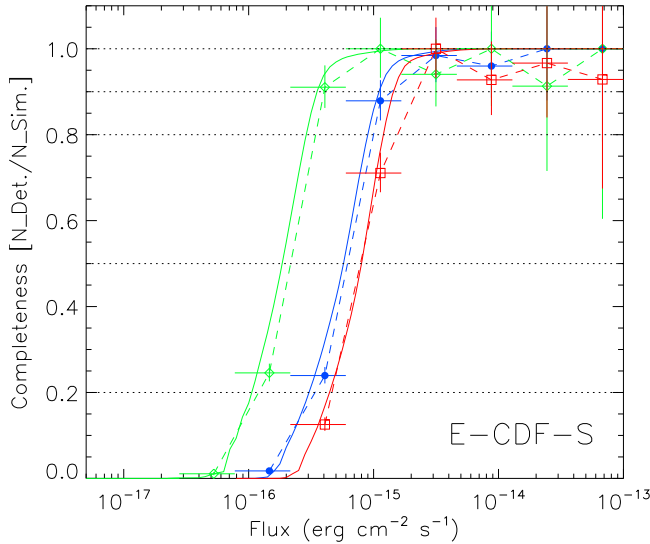
Figure 53. Completeness as a function of flux given the 250 ks E-CDF-S main-catalog $P < 0.002$ criterion for the simulations in the full (blue filled circles), soft (green open diamonds), and hard (red open squares) bands, overlaid with the corresponding sky coverage curves (solid curves) that are normalized to the maximum sky coverage (see Figure 57). The dashed lines make connections between the corresponding adjacent cross points. The horizontal dotted lines denote five completeness levels.

Table 13
250 ks E-CDF-S Flux Limit and Completeness

Completeness (%)	$f_{0.5-7\,\mathrm{keV}}$ (erg cm^{-2} s^{-1})	$f_{0.5-2\,\mathrm{keV}}$ (erg cm^{-2} s^{-1})	$f_{2-7\,\mathrm{keV}}$ (erg cm^{-2} s^{-1})
90	1.1×10^{-15}	3.5×10^{-16}	1.4×10^{-15}
80	9.0×10^{-16}	2.9×10^{-16}	1.2×10^{-15}
50	5.7×10^{-16}	1.9×10^{-16}	8.0×10^{-16}
20	3.0×10^{-16}	1.1×10^{-16}	4.4×10^{-16}

and matched-filter techniques. The absolute astrometry of X-ray source positions is locked to that of the TENIS WIRCam K_s-band catalog and the median positional offset of the X-ray-K_s-band matches is $0\rlap{.}{''}38$. The median X-ray positional uncertainties at the $\approx 68\%$ confidence level are $0\rlap{.}{''}63$ and $1\rlap{.}{''}20$ for the main and supplementary catalogs, respectively.

5. Basic analyses of the X-ray and multiwavelength properties of the E-CDF-S sources indicate that 90.6%, 6.7%, and 2.7% of the main-catalog sources are likely AGNs, galaxies, and stars, respectively. In the areas within respective off-axis angles of $3'$ of the four E-CDF-S aim points, the mean observed main-catalog AGN and galaxy source densities reach 5200^{+1000}_{-800} deg^{-2} and 500^{+400}_{-200} deg^{-2}, respectively. 62.5%, 30.4%, and 7.1% of the supplementary-catalog sources are likely AGNs, galaxies, and stars, respectively.

6. A total of 275 E-CDF-S main-catalog sources are new and are generally fainter and more obscured, compared to the L05 main-catalog sources. Among the 275 new main-catalog sources, 86.5% are likely AGNs and 11.3% are likely normal and starburst galaxies (with the remaining

of having $0.002 < P < 0.1$ and having bright ($K_s < 22.3$) near-infrared counterparts. 51 (91.1%) of these 56 sources have either spectroscopic or photometric redshifts.

4. X-ray source positions for the E-CDF-S main and supplementary catalogs are determined utilizing centroid

Table 14
250 ks E-CDF-S: Background Parameters

Band (keV)	Mean Background (count pixel^{-1})[a]	Mean Background (count Ms^{-1} pixel^{-1})[b]	Total Background[c] (10^4 counts)	Count Ratio[d] (Background/Source)
Full (0.5–7.0)	0.031	0.160	52.4	6.5
Soft (0.5–2.0)	0.009	0.048	15.7	3.2
Hard (2–7)	0.022	0.109	36.8	12.2

Notes.
[a] The mean numbers of background counts per pixel.
[b] The mean numbers of background counts per pixel divided by the mean effective exposures.
[c] The total numbers of background counts in the background maps.
[d] Ratio between the total number of background counts and the total number of detected source counts in the main catalog.
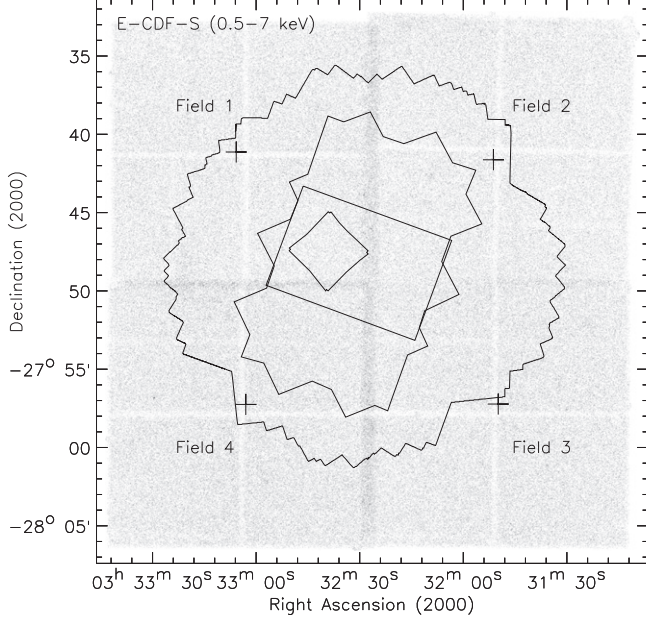
Figure 54. Full-band (0.5–7.0 keV) background map of the 250 ks E-CDF-S rendered using linear grayscales. The higher background between fields is due to the larger effective exposure caused by overlapping observations. The regions and the plus signs have the same meanings as those in Figure 30.
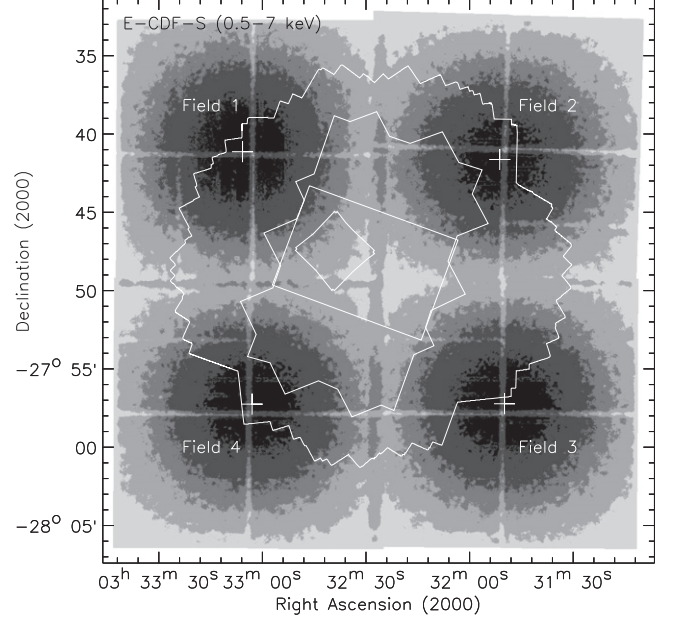
Figure 56. Full-band (0.5–7.0 keV) sensitivity map for the 250 ks E-CDF-S main catalog. The grayscale levels, ranging from black to light gray, denote areas with flux limits of $<2.0 \times 10^{-16}$, 2.0×10^{-16} to 4.0×10^{-16}, 4.0×10^{-16} to 6.0×10^{-16}, 6.0×10^{-16} to 10^{-15}, and $>10^{-15}$ erg cm^{-2} s^{-1}, respectively. The regions and the plus signs have the same meanings as those in Figure 30.
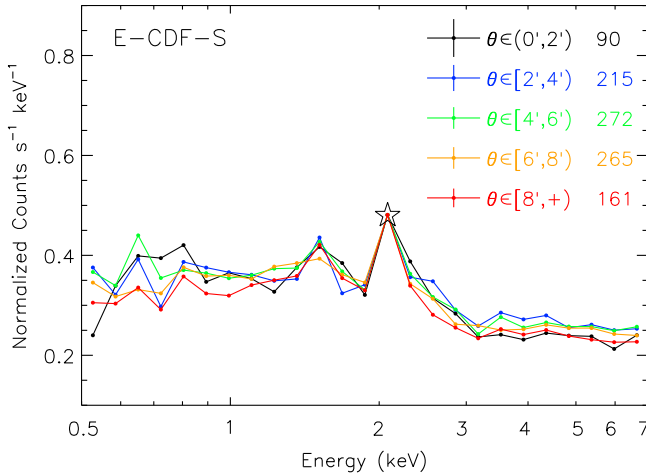
Figure 55. Mean background spectra for the 250 ks E-CDF-S main-catalog sources calculated in various bins of off-axis angle. The spectra are normalized to have the same value at an energy slightly above 2 keV, which is indicated by a large five-pointed star. For clarity, errors on individual spectral data points are not plotted; the typical spectral error value and number of sources in each bin of off-axis angle are annotated in the top right corner.
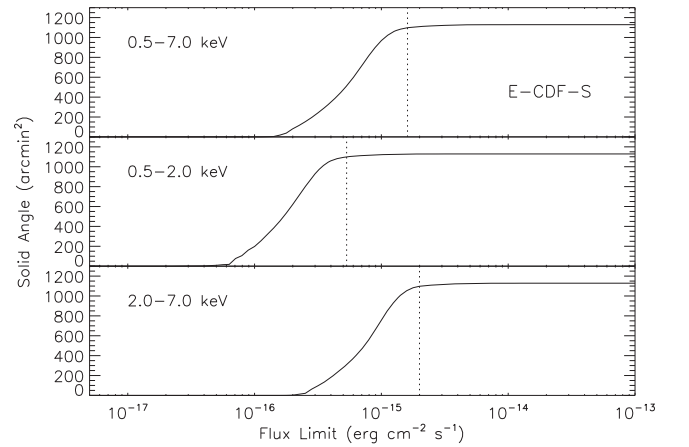
Figure 57. Survey solid angle as a function of flux limit in the full, soft, and hard bands for the 250 ks E-CDF-S main catalog. The vertical dotted lines indicate the median fluxes of the main-catalog sources detected in the three bands.

2.2% being likely stars), which reflects the rise of normal and starburst galaxies when probing fainter fluxes.

7. Simulations demonstrate that our E-CDF-S main catalog is highly reliable ($\lesssim 8$, 6, and 3 false detections are expected in the full, soft, and hard bands, respectively) and is reasonably complete (e.g., in the central $\theta \leqslant 6'$ areas, the completeness levels are $\gtrsim 79\%$, 99%, and 82% for sources with $\geqslant 4$ counts in the full, soft, and hard bands, respectively).

8. The E-CDF-S mean background is 0.160, 0.048, and 0.109 count Ms^{-1} $pixel^{-1}$ for the full, soft, and hard bands, respectively; 97.1%, 99.1%, and 98.0% of the pixels have zero background counts in the background maps for the full, soft, and hard bands, respectively.

9. The 250 ks E-CDF-S achieves on-axis (i.e., near the four aim points) flux limits of $\approx 2.0 \times 10^{-16}$, 7.6×10^{-17}, and 3.0×10^{-16} erg cm^{-2} s^{-1} for the full, soft, and hard bands, respectively, a factor of ≈ 1.5–2.0 improvement over those of L05, due to the facts that we adopt a sensitive two-stage source-detection procedure and that L05 adopted a different methodology for sensitivity calculations.

REFERENCES

Alexander, D. M., Bauer, F. E., Brandt, W. N., et al. 2003, AJ, 126, 539 (A03)
Ashby, M. L. N., Willner, S. P., Fazio, G. G., et al. 2013, ApJ, 769, 80
Baganoff, F. K., Maeda, Y., Morris, M., et al. 2003, ApJ, 591, 891
Balestra, I., Mainieri, V., Popesso, P., et al. 2010, A&A, 512, 12
Barger, A. J., Cowie, L. L., Capak, P., et al. 2003, AJ, 126, 632
Barger, A. J., Cowie, L. L., & Wang, W.-H. 2008, ApJ, 689, 687
Bauer, F. E., Alexander, D. M., Brandt, W. N., et al. 2004, AJ, 128, 2048
Beckwith, S. V. W., Stiavelli, M., Koekemoer, A. M., et al. 2006, AJ, 132, 1729
Benjamini, Y., & Hochberg, Y. 1995, J. Roy. Stat. Soc. B., 57, 289
Bonzini, M., Mainieri, V., Padovani, P., et al. 2012, ApJS, 203, 15
Brandt, W. N., & Alexander, D. M. 2015, A&ARv, 23, 1
Brandt, W. N., Alexander, D. M., Hornschemeier, A. E., et al. 2001, AJ, 122, 2810

Broos, P. S., Feigelson, E. D., Townsley, L. K., et al. 2007, ApJS, 169, 353
Broos, P. S., Townsley, L. K., Feigelson, E. D., et al. 2010, ApJ, 714, 1582
Broos, P. S., Townsley, L. K., Feigelson, E. D., et al. 2011, ApJS, 194, 2
Caldwell, J. A. R., McIntosh, D. H., Rix, H.-W., et al. 2008, ApJS, 174, 136
Capak, P., Cowie, L. L., Hu, E. M., et al. 2004, AJ, 127, 180
Cardamone, C. N., van Dokkum, P. G., Urry, C. M., et al. 2010, ApJS, 189, 270
Chapman, S. C., Blain, A. W., & Ivison, R. J. 2005, ApJ, 622, 772
Cooper, M. C., Aird, J. A., Coil, A. L., et al. 2011, ApJS, 193, 14
Cooper, M. C., Yan, R., Dickinson, M., et al. 2012, MNRAS, 425, 2116
Coppin, K. E. K., Danielson, A. L. R., Geach, J. E., et al. 2012, MNRAS, 427, 520
Cowie, L. L., Barger, A. J., Hu, E. M., Capak, P., & Songaila, A. 2004, AJ, 127, 3137
Damen, M., Labbe, I., van Dokkum, P. G., et al. 2011, ApJ, 727, 1
Eadie, W. T., Dryard, D., James, F. E., Roos, M., & Sadoulet, B. 1971, Statistical Methods in Expermental Physics (Amsterdam: North-Holland)
Ebeling, H., White, D. A., & Rangarajan, F. V. N. 2006, MNRAS, 368, 65
Ehlert, S., Allen, S. W., Brandt, W. N., et al. 2013, MNRAS, 428, 3509
Elvis, M., Civano, F., Vignali, C., et al. 2009, ApJS, 184, 158
Feigelson, E. D., & Babu, G. J. 2012, Modern Statistical Methods for Astronomy with R Applications (Cambridge: Cambridge Univ. Press)
Feigelson, E. D., Hornschemeier, A. E., Micela, G., et al. 2004, ApJ, 611, 1107
Freeman, P. E., Kashyap, V., Rosner, R., & Lamb, D. Q. 2002, ApJS, 138, 185
Garmire, G. P., Bautz, M. W., Ford, P. G., Nousek, J. A., & Ricker, G. R., Jr. 2003, Proc. SPIE, 4851, 28
Gehrels, N. 1986, ApJ, 303, 336
Gendreau, K. C., Mushotzky, R., Fabian, A. C., et al. 1995, PASJ, 47, L5
Georgantopoulos, I., Comastri, A., Vignali, C., et al. 2013, A&A, 555, 43
Getman, K. V., Flaccomio, E., Broos, P. S., et al. 2005, ApJS, 160, 319
Giacconi, R., Zirm, A., Wang, J., et al. 2002, ApJS, 139, 369
Giavalisco, M., Ferguson, H. C., Koekemoer, A. M., et al. 2004, ApJL, 600, L93
Gilli, R., Comastri, A., & Hasinger, G. 2007, A&A, 463, 79
Grazian, A., Fontana, A., de Santis, C., et al. 2006, A&A, 449, 951
Grogin, N. A., Kocevski, D. D., Faber, S. M., et al. 2011, ApJS, 197, 35
Hasinger, G., Burg, R., Giacconi, R., et al. 1998, A&A, 329, 482
Hickox, R. C., & Markevitch, M. 2006, ApJ, 645, 95
Hinshaw, G., Larson, D., Komatsu, E., et al. 2013, ApJS, 208, 19
Hornschemeier, A. E., Brandt, W. N., Garmire, G. P., et al. 2001, ApJ, 554, 742
Hsieh, B.-C., Wang, W.-H., Yan, H. J., et al. 2012, ApJ, 749, 88
Hsu, L.-T., Salvato, M., Nandra, K., et al. 2014, ApJ, 796, 60
Kim, M., Kim, D.-W., Wilkes, B. J., et al. 2007, ApJS, 169, 401
Koekemoer, A. M., Faber, S. M., Ferguson, H. C., et al. 2011, ApJS, 197, 36
Kraft, R. P., Burrows, D. N., & Nousek, J. A. 1991, ApJ, 374, 344
Kriek, M., van Dokkum, P. G., Franx, M., et al. 2008, ApJ, 677, 219
Laird, E. S., Nandra, K., Georgakakis, A., et al. 2009, ApJS, 180, 102
Le Fèvre, O., Cassata, P., Cucciati, O., et al. 2013, A&A, 559, 14
Lehmer, B. D., Alexander, D. M., Chapman, S. C., et al. 2009, MNRAS, 400, 299
Lehmer, B. D., Brandt, W. N., Alexander, D. M., et al. 2005, ApJS, 161, 21 (L05)
Lehmer, B. D., Xue, Y. Q., Brandt, W. N., et al. 2012, ApJ, 752, 46
Luo, B., Bauer, F. E., Brandt, W. N., et al. 2008, ApJS, 179, 19
Luo, B., Brandt, W. N., Xue, Y. Q., et al. 2010, ApJS, 187, 560
Lyons, L. 1991, Data Analysis for Physical Science Students (Cambridge: Cambridge Univ. Press)
Markevitch, M., Bautz, M. W., Biller, B., et al. 2003, ApJ, 583, 70
Marshall, F. E., Boldt, E. A., Holt, S. S., et al. 1980, ApJ, 235, 4
Miller, N. A., Bonzini, M., Fomalont, E. B., et al. 2013, ApJS, 205, 13
Miyaji, T., Zamorani, G., Cappelluti, N., et al. 2007, ApJS, 172, 396
Morrison, G. E., Owen, F. N., Dickinson, M., Ivison, R. J., & Ibar, E. 2010, ApJS, 188, 178
Nandra, K., Laird, E. S., Adelberger, K., et al. 2005, MNRAS, 356, 568
Nandra, K., Laird, E. S., Aird, J. A., et al. 2015, ApJS, 220, 10
Puccetti, S., Vignali, C., Cappelluti, N., et al. 2009, ApJS, 185, 586
R Core Team 2015, R: A language and environment for statistical computing, R Foundation for Statistical Computing, Vienna, Austria, (https://www.R-project.org/)
Rafferty, D. A., Brandt, W. N., Alexander, D. M., et al. 2011, ApJ, 742, 3
Ranalli, P., Comastri, A., & Setti, G. 2005, A&A, 440, 23
Ravikumar, C. D., Puech, M., Flores, H., et al. 2007, A&A, 465, 1099
Retzlaff, J., Rosati, P., Dickinson, M., et al. 2010, A&A, 511, 50
Richards, E. A. 2000, ApJ, 533, 611

Richards, E. A., Kellermann, K. I., Fomalont, E. B., Windhorst, R. A., & Partridge, R. B. 1998, AJ, 116, 1039

Santini, P., Fontana, A., Grazian, A., et al. 2009, A&A, 504, 751

Silverman, J. D., Mainieri, V., Salvato, M., et al. 2010, ApJS, 191, 124

Skelton, R. E., Whitaker, K. E., Momcheva, I. G., et al. 2014, ApJS, 214, 24

Stark, A. A., Gammie, C. F., Wilson, R. W., et al. 1992, ApJS, 79, 77

Szokoly, G. P., Bergeron, J., Hasinger, G., et al. 2004, ApJS, 155, 271

Taylor, E. N., Franx, M., van Dokkum, P. G., et al. 2009, ApJS, 183, 295

Townsley, L. K., Broos, P. S., Garmire, G. P., & Nousek, J. A. 2000, ApJL, 534, L139

Townsley, L. K., Broos, P. S., Nousek, J. A., & Garmire, G. P. 2002, NIMPA, 486, 751

Treister, E., Virani, S., Gawiser, E., et al. 2009, ApJ, 693, 1713

Vikhlinin, A. 2001, Reducing ACIS Quiescent Background Using Very Faint Mode (Cambridge: CXC) http://cxc.harvard.edu/cal/Acis/Cal_prods/vfbkgrnd/

Wang, S. X., Brandt, W. N., Luo, B., et al. 2013, ApJ, 778, 179

Wang, W.-H., Cowie, L. L., Barger, A. J., Keenan, R. C., & Ting, H.-C. 2010, ApJS, 187, 251

Williams, R. E., Blacker, B., Dickinson, M., et al. 1996, AJ, 112, 1335

Wirth, G. D., Willmer, C. N. A., Amico, P., et al. 2004, AJ, 127, 3121

Xue, Y. Q., Brandt, W. N., Luo, B., et al. 2010, ApJ, 720, 368

Xue, Y. Q., Brandt, W. N., Luo, B., et al. 2011, ApJS, 195, 10 (X11)

Yang, G., Xue, Y. Q., Luo, B., et al. 2014, ApJS, 215, 27

Zheng, W., Mikles, V. J., Mainieri, V., et al. 2004, ApJS, 155, 73